ATOMISTIC CHARACTERIZATION AND CONTINUUM MODELING OF NOVEL THERMOMECHANICAL BEHAVIORS OF ZINC OXIDE NANOSTRUCTURES

A Dissertation
Presented to
The Academic Faculty

By

Ambarish J. Kulkarni

In Partial Fulfillment
Of the Requirements for the Degree
Doctor of Philosophy in the
School of Mechanical Engineering

Georgia Institute of Technology
December 2007

ATOMISTIC CHARACTERIZATION AND CONTINUUM MODELING OF NOVEL THERMOMECHANICAL BEHAVIORS OF ZINC OXIDE NANOSTRUCTURES

Approved by:

Dr. Min Zhou, Advisor
School of Mechanical Engineering
Georgia Institute of Technology

Dr. Jianmin Qu
School of Mechanical Engineering
Georgia Institute of Technology

Dr. Samuel Graham
School of Mechanical Engineering
Georgia Institute of Technology

Dr. Naresh Thadhani
School of Materials Science and Engineering
Georgia Institute of Technology

Dr. Kenneth A. Gall
School of Materials Science and Engineering
Georgia Institute of Technology

Dr. Sukit Limpijumnong
School of Physics
Suranaree University of Technology

Date Approved: October 2, 2007

To my wife, Ruta, and my family

ACKNOWLEDGEMENTS

I sincerely thank my advisor, Dr. Min Zhou, for his consistent support, guidance, understanding, and patience during my Ph.D. study. I thoroughly enjoyed interacting with him on both technical and personal issues. He has been instrumental in my development as a graduate student and a person as a whole.

I would like to express my appreciation to our collaborators, Dr. Sukit Limpijumnong, Kanoknan Sarasamak, Prof. F. J. Ke and Jun Wang for their wonderful support of my work. I also wish to thank my committee members, Dr. Jianmin Qu, Dr. Samuel Graham, Dr. Naresh Thadhani and Dr. Ken Gall for reviewing my work and giving insightful comments.

I would also like to thank my friends and colleagues, Vikas Tomar, Wuwei Liang, Mahesh Shenoy, Narasimhan Swaminathan, Remi Dingreville, Nitin Patel, Raghvendra Vijaywargiya, Rajesh Prasannavenkatesan and many others. It is through their help, support and friendship that my research has progressed so well and I have enjoyed my life here.

I would also like to acknowledge the tremendous help and support I have received from my wife Ruta, my parents and family.

I would like to acknowledge the support through NSF grant no. CMS9984298 and NSFC grant no. 10528205. The computations are carried out at the NAVO, ARL, AHPCRC and ASC MSRCs through AFOSR MURI no. D49620-02-1-0382.

TABLE OF CONTENTS

LIST OF TABLES

Page

LIST OF FIGURES

SUMMARY

Zinc oxide (ZnO) nanowires and nanorods are a new class of one-dimensional (1D) nanomaterials with a wide range of potential applications as catalysts, chemical and biomedical sensors, resonators, transparent conductors, and electronic and photonic interconnects in nano-electro-mechanical systems (NEMS). The motivation for this work stems from the lack of understanding and characterization of their mechanical and thermal behaviors which are essential for their incorporation in nanosystems. Furthermore, it is imperative to characterize the dimensional dependence of the thermomechanical responses observed due to the high surface-to-volume ratios at the nanoscale.

The overall goal of this work is to develop a fundamental understanding of the mechanisms controlling the responses of these nanostructures. The specific focus of this research is threefold: (1) development of a molecular dynamics (MD) based computational framework for analyzing the thermomechanical behavior, (2) characterization of the thermal and mechanical behaviors and their coupling in ZnO nanowires and (3) development of models for the behavior with focus on pseudoelasticity and thermal conductivity.

The thermal response analyses use an equilibrium Green-Kubo approach to quantify the thermal conductivity of 19-41 Å sized wires in the 500-1500 K temperature range. Values of thermal conductivity obtained are one order of magnitude lower than that for bulk ZnO single crystal and decrease for smaller sizes due to enhanced surface scattering of phonons. A modified equation for phonon radiative transport (EPRT) incorporating the effect of surface scattering is used to model the thermal conductivity as a function of size and temperature.

Quasistatic tensile loading of wires in the same size range show that the elastic moduli values are 68.2-27.8% higher than the corresponding values for bulk ZnO. More

importantly, phase transformations from the initial wurtzite (WZ) structure to a previously unknown graphite-like phase (HX) and a body-centered-tetragonal phase (BCT-4) are discovered in $[01\bar{1}0]$- and [0001]-oriented nanowires, respectively, under uniaxial tensile loading. The discovery of these new polymorphs brings about a more complete understanding of the extent of polymorphism in ZnO and its dependence on load triaxiality. The reversibility of the WZ→HX transformation gives rise to a novel pseudoelastic behavior in $[01\bar{1}0]$-oriented nanowires with recoverable strains up to 16%. This previously unknown phenomenon is only observed in nanowires and does not occur in bulk ZnO. A micromechanical continuum model is developed to capture the major characteristics of the overall constitutive behavior (elastic deformations of the individual phases, transformations from WZ to HX during loading and from HX to WZ during unloading), accounting for both the size effect and temperature effect.

The effect of the phase transformations on the mechanical (elastic moduli, yield and fracture strengths) and thermal properties (conductivity) are characterized. Specifically, a computational scheme involving Green-Kubo calculations at fixed values of strain is used to study the evolution of conductivity during loading. Results obtained show that the WZ→HX phase transformation causes a novel transition in thermal response with the conductivity of HX wires being 20.5-28.5% higher than that of the initial WZ-structured wires.

The results obtained here can provide guidance and criteria for the design and fabrication of a range of new building blocks for nanometer-scale sensors, transducers, resonators and other devices that rely on thermomechanical response and thermomechanical coupling.

CHAPTER 1 : INTRODUCTION

As nanotechnology progresses and complex nanosystems are being fabricated, a rising impetus is being given to the development of multi-functional and size-driven materials. The term size-driven refers to emergence of exciting properties from materials as we explore smaller i.e. micro and nano-size scales. Furthermore, recent advances in nanofabrication technology have promoted the growth of nanocomponents such as nanowires, nanotubes, nanobelts and associated development of complex nanoarchitectures through simple bottom-up approaches (Bae et al. 2002; Dai et al. 2002). Most of these materials are made of semiconducting oxides and nitrides of Zn, Sn, In, Cd, and Ga [such as zinc oxide (ZnO), tin oxide (SnO) and gallium nitride (GaN)], with ZnO being the most versatile in both structure and properties (Wang et al. 2004). ZnO has been explored for applications in sensing, environmental monitoring, bio-medical systems and communications technology. It has emerged as an important component for integration in nanoelectromechanical systems (NEMS) because (i) it is a semiconductor and (ii) it is piezoelectric (owing to its non-centrosymmetric structure) (Wang et al. 2004). Recently, ZnO nanostructures (nanobelts and nanowires) have been grown using vapor deposition techniques (Pan et al. 2001). As functional nano-building blocks, these nanostructures have found applications in ultra-sensitive chemical and biological species sensors, nanoresonators and nanocantilevers, field effect transistors (Comini et al. 2002b; Arnold et al. 2003; Bai et al. 2003; Hughes and Wang 2003).

The integration of these nanostructures in any system entails detailed understanding of their inherent properties, functionalities and behavior. Since these nanostructures have only been synthesized recently, there is a lack of understanding and characterization of their mechanical and thermal behaviors. Response to stimuli such as applied mechanical stress, thermal gradients, size and temperature effects have to be

characterized. The mechanical and thermal behaviors of these nanocomponents are important in many of the applications since strength, stiffness, and thermal conductivity are among the key attributes involved. For example, the assembly of nanobelts between electrodes or substrates in a system requires a balance of rigidity and strength, while in applications such as nanocantilever sensors the mechanical resonance depends on the bending modulus. On the other hand, at the nanoscale, electric field density and heat flux are very high and are therefore of great concern. One example involves thermoelectric applications which require careful control of the thermal and electrical conductivities. A great challenge and perhaps also an opportunity in regulating such properties for device integration is their dependence on size at the nanoscale. The primary contributor to this size effect is the high surface-to-volume ratios in the 1D nanostructures. Unlike at the macroscale where the effect of surfaces on material response is negligible due to very low surface-to-volume ratios, surfaces play a dominant role in altering the behavior at the nanoscale. The size dependences of Young's moduli and thermal conductivity are examples (Shi et al. 2004; Kulkarni et al. 2005). Characterization of mechanical and thermal property variations with nanostructure sizes is crucial to the incorporation of these structures in nanodevices.

More importantly for ZnO nanowires, our results show that for specific conditions of nanowire orientation and loading triaxialities, mechanical loading induces previously unknown structural (or phase) transformations (Kulkarni et al. 2006). Specifically, previously unknown graphite-like phase (HX, $P6_3/mmc$ space group) and body-centered-tetragonal phase (BCT-4, $P4_2/mnm$ space group) are observed in $[01\bar{1}0]$- and [0001]-oriented nanowires, respectively under uniaxial tensile loading. The reversible phase transformation from the tetrahedrally coordinated wurtzite (WZ, $P6_3mc$ space group) phase to the newly discovered HX phase results in a novel pseudoelastic behavior in $[01\bar{1}0]$-oriented ZnO nanowires (Kulkarni et al. 2006). Since the parent and transformed

phases can have very different properties, such stress-induced phase transformations may significantly alter the response of the nanowires. Examples include the modulation of piezoelectric constant, Seebeck coefficient and thermal conductivity (Picu et al. 2003; Kulkarni and Zhou 2007). Such effects provide mechanisms for controlling or "tuning" the thermal response of a nanocomponent through the application of a mechanical input. Conversely, temperature variations can possibly induce structural changes and alter the mechanical strength and rigidity of nanocomponents. This thermomechanical coupling provides both opportunities for developing "tunable" functional nano-devices and challenges for ensuring thermomechanical reliability and functionality of nano-systems. Since these phase transformations and the novel pseudoelastic behavior have just been discovered in ZnO nanowires, a fundamental understanding of the overall constitutive behavior, the nature of the phase transformation and the characteristics of the transformed phase is needed in order to unleash the potential of these nanowires.

The research focuses on the characterization of the thermomechanical behavior of ZnO nanowires and nanorods. Molecular dynamics (MD) simulations with Buckingham-type interatomic potential with charge interactions are used to characterize the response of the nanowires. The first part of the research investigates the mechanical response of the nanowires under uniaxial loading along the wire axis. In particular, the elastic response of the parent structure (WZ), the phase transformation to HX/BCT-4 phase and the elastic stretching of the transformed phase (HX/BCT-4) are studied. Emphasis is on the crystallographic characterization of the new phase, the crystallographic and mechanistic description of the transformation and the quantification of the size and temperature effects on the overall stress-strain response. First principles calculations using the density functional theory (DFT) are carried out to establish the stability of the newly discovered phases under the applied loading conditions.

The second part of the research focuses on characterizing the novel pseudoelastic behavior in the $[01\bar{1}0]$-oriented nanowires. The critical stress for transformation

initiation, maximum recoverable strains, and hysteretic dissipation values are determined for a range of wire sizes and temperatures. A micromechanics based model is developed to describe the constitutive relationship for the pseudoelastic response. Emphasis is on the phase evolution, transformation completion and the overall stress-strain relation as a function of wire size and temperature.

The third part of the research involves extracting the thermal response of the nanowires using MD simulations coupled with a statistical mechanics based Green-Kubo approach. Specifically, the thermal conductivity of the nanowires is characterized for a range of sizes and temperatures. Size effect characterization is essential since at the nanoscale surface scattering of phonons dominates the thermal response and has the potential of reducing the thermal conductivity by as much as two orders of magnitude as compared to the bulk. A new approach developed by Majumdar (1993) is used to model the thermal response. This approach involves treating phonon dominated thermal behavior as radiative heat transfer with modifications to account for surface scattering of phonons (Lu et al. 2002; Lu et al. 2003). Using this approach, an expression for the thermal conductivity of the nanowires accounting for the variations with size, surface atom density and temperature is developed.

The final part of the research investigates the thermomechanical coupling in the nanowires' responses. In particular, the effect of lattice strains, distortions and phase transformations on thermal conductivity is characterized. The findings and insights will prove to be effective tools for the design of future nanosystems.

The organization of this thesis is as follows. Chapter 2 briefly reviews relevant topics such as the surface dependence of mechanical and thermal behavior at the nanoscale, characteristics of phase transformations and pseudoelasticity, constitutive models for describing mechanical response of nanowires and models for nanoscale heat transfer. Chapter 3 describes the MD computational framework including interatomic potentials and their calibration, generation of nanowire structures, crystallographic

analysis techniques, schemes for characterizing thermal and mechanical response and first-principles framework for determining phase stability. Chapter 4 describes and characterizes the novel phase transformations observed in this research. Chapter 5 characterizes the pseudoelastic behavior of the nanowires. Size and temperature dependence of transformation parameters is analyzed. The micromechanical continuum model developed to capture the overall pseudoelastic behavior is delineated. Chapter 6 discusses the thermal responses of the nanowires under stress-free and strained conditions. Finally, the conclusions reached in this research and future research directions are presented in chapter 7.

CHAPTER 2 : BACKGROUND

This chapter briefly reviews the relevant topics such as the fabrication and structure of the ZnO nanowires, surface dependence of mechanical and thermal properties and their evaluation. Other topics reviewed include characterization and modeling of phase transformations and the modeling of thermal responses at the nanoscale.

2.1 Material System

ZnO nanowires and nanobelts are one class of nanostructures endowed with semiconductivity, piezoelectricity and coupled thermomechanical responses (Wang et al. 2004). As functional nano-building blocks, these components have a wide variety of potential applications such as catalysts, chemical sensors, resonators, transparent conductors, biosensors, medical devices, nano-electronic components, and nano-photonic components (Comini et al. 2002b; Arnold et al. 2003; Bai et al. 2003; Hughes and Wang 2003; Kong and Wang 2003; Wang 2004b, 2004a; Gao et al. 2005; Gao and Wang 2005; Wang 2005). Recently, ZnO nanostructures with rectangular cross-sections referred to as nanobelts/nanowires and hexagonal cross-sections termed as nanorods have been grown through vapor deposition (Pan et al. 2001; Wei et al. 2006) (see Figure 2.1). The synthesis is based on thermal evaporation of ZnO powders in a tube furnace and condensation of the vapors on an alumina plate. The as-synthesized nanowires and nanorods are single-crystalline and wurtzite-structured with lattice constants a = 3.249 Å and c = 5.206 Å. The most common growth directions for the nanobelts are along the [0001] and $[01\bar{1}0]$ crystalline axes of the wurtzite structure. Growth along the $[2\bar{1}\bar{1}0]$ orientation is resisted by the energy barrier due to surface polarization, but such structures have also been reported (Kong and Wang 2003).

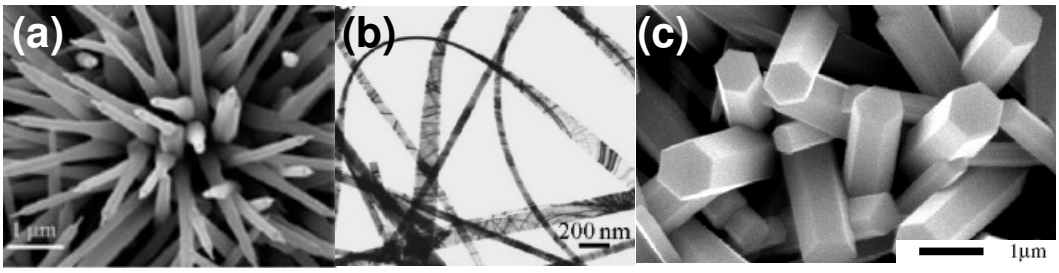

Figure 2.1 TEM images of ZnO nanostructure: (a) nanowires (Wang et al. 2004), (b) rectangular nanobelts (Wang et al. 2004) and (c) hexagonal nanorods (Wei et al. 2006).

2.2 Mechanical Behavior at the Nanoscale

2.2.1 Surface Dominated Mechanical Response

The high surface-to-volume ratios in the ZnO nanowires enhance surface effects on the mechanical response giving rise to a size effect unique to the nanoscale. Such size dependence, while creating challenges to design, if characterized appropriately can result in the development of novel tunable devices in NEMS. Characterization of mechanical response of nanostructures is therefore vital. Elastic properties of ZnO nanostructures have been evaluated experimentally through scanning electron microscopy (Desai and Haque 2007; Hoffmann et al. 2007), high resolution transmission electron microscopy (Bai et al. 2003; Chen et al. 2006a, 2006b) and atomic force microscopy (Mao et al. 2003; Song et al. 2005; Ni and Li 2006; Lucas et al. 2007a; Lucas et al. 2007b). All experimental evaluations involved either nanoindentation or bending of the nanowires. Results obtained from such experiments have failed to show general trends in the nanowires behaviors. While some of the experiments show that the moduli of the nanowires are higher than bulk values and show a distinct size dependence (Chen et al. 2006a; Desai and Haque 2007), other experiments show that the moduli are similar to or lower than bulk values (Hoffmann et al. 2007; Lucas et al. 2007a). The apparent contradictions in the experimental results put to question the validity and the applicability of current experimental setups at such a small scale. However, it is possible that further

refinement in the experimental procedures could enhance the results and possibly explain the physical mechanisms behind such contradictions.

Atomistic simulations, on the other hand, provide an alternate medium of analyzing the properties of materials in reasonably realistic conditions. Traditionally, three atomistic simulation methods have been proposed to study material behavior: First principles/quantum mechanical (QM), Molecular Dynamics (MD) and Molecular Statics (MS). QM simulations have few approximations associated in their evaluations and have been used to accurately characterize the elastic properties of nanostructures (Opitz et al. 2002; Zheng et al. 2002; Jelínek et al. 2003). However, these calculations tend to be computationally intensive for large systems (as is the case for the nanostructures considered in this research) and therefore are limited to the study of small clusters of atoms. MS calculations can handle larger systems and can predict material properties by determining the energetically favorable configurations under applied external inputs. Recently, MS calculations have been employed to study the effect of free surfaces and edges on the structure and elastic properties of FCC metal nanowires by applying a uniform uniaxial strain incrementally to the relaxed nanowire configurations followed by energy minimization (Diao 2004). Strain meshing represents another family of MS techniques used to study the mechanical response of nanostructures where the elastic constants are obtained by numerical interpolation of the energy density meshing in the strain space (Liang et al. 2005a). However, such calculations assume zero temperature conditions and therefore cannot represent thermal influences which are important where phenomena such as phase transformations or shape memory exist. MD simulations, which use Newton's second law to determine the positions and velocities of atoms at finite temperatures, are appropriate for determining material response at nano- and micro-scales. MD simulations allow for the study of comparatively large systems and have emerged as an effective tool for the characterization of the mechanical and thermal behaviors of nanostructures (Mehrez et al. 1997; Branicio and Rino 2000; Komanduri et

al. 2001, 2003; Liang and Zhou 2003; Diao et al. 2004a; Diao et al. 2004c; Gall et al. 2004; Ju et al. 2004).

Alternatively, various approaches have also been developed to extend continuum theories to nanostructured materials through the incorporation of surface attributes (Streitz et al. 1994; Miller and Shenoy 2000; Zhang et al. 2002; Sun and Zhang 2003). Specifically, several available thermodynamic models allow the size dependence of the response of nanostructures to be characterized through the inclusion of surface free energy or surface stresses (Dingreville et al. 2005a). While such approaches provide effective analytical tools they require prior knowledge of the material properties such as bulk and surface elastic constants. In summary, among the family of computational techniques, MD has the capacity to effectively predict the strain evolution of the elastic properties and more importantly predict phase transformation if it exists. Consequently, in the proposed research, MD simulations are considered to predict the thermomechanical responses of ZnO nanostructures.

2.2.2 Phase Transformations and Polymorphism

One-to-one binary compounds obeying the octet rule (i.e., I-VII, II-VI, III-V, or IV-IV materials) are generally semiconductors or insulators. Although these type AB compounds have the same chemical formula units, their crystal structures under ambient conditions show significant variations with bond ionicity (see Figure 2.2). While highly ionic compounds like CsCl (I-VII) prefer dense crystal structures with a coordination number of 8 (CN= 8), compounds like NaCl (also I-VII) with lower degrees of ionicity gravitate towards the rocksalt structure (RS, $Fm\bar{3}m$ space group) with CN= 6. As the degree of ionicity decreases (shifting toward covalent bonding states), compounds such as ZnO (II-VI), GaN (III-V) and SiC (IV-IV) stabilize in either wurtzite (WZ, $P6_3mc$) or zinc blende (ZB, $F\bar{4}3m$) structures with CN = 4. In such covalent compounds, the valence electron counting (two electrons in each bond) is satisfied through the formation

of four bonds for each atom. However, in compounds with higher degrees of ionicity such as CsCl and NaCl, the gain through cation-anion attractions leads to the formation of structures with higher C.N. Nevertheless, bond ionicity should not be considered as the only factor in determining crystalline structures in such compounds since the assumption of a particular structure also depends on intrinsic factors such as composition, band structure, valence electrons, bonding states and structural symmetries. A change in any of these factors may trigger a transformation to a different structure, giving rise to polymorphism

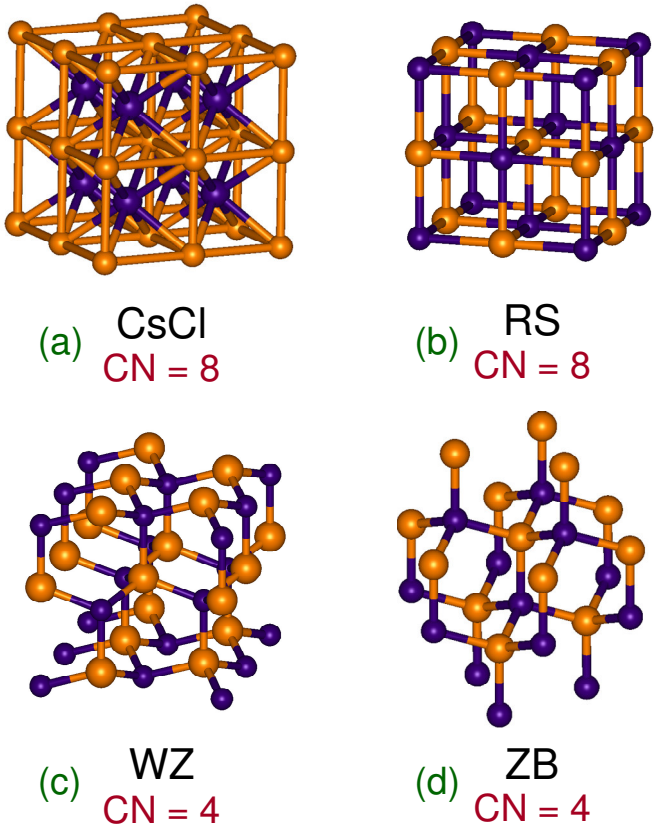

Figure 2.2 Crystal structures of type AB compounds: (a) CsCl, (b) Rocksalt (RS), (c) Wurtzite (WZ) and (d) Zinc blende (ZB).

Traditionally, external loading and temperature changes are used to effect polymorphic transitions in materials. Polymorphism through stress-induced phase transformations are widely observed in groups IV, III-V and II-VI materials including

ZnO (Mujica et al. 2003). There are three hitherto well known polymorphs of ZnO, including WZ, ZB and RS (Ozgur et al. 2005). WZ is the most stable and commonly observed phase under ambient pressure. ZB can be obtained only on cubic surfaces under specific growth conditions. RS is the result of a transformation from WZ at pressures between 8-10 GPa (Bates et al. 1962; Jaffe and Hess 1993; Karzel et al. 1996; Desgreniers 1998; Jaffe et al. 2000; Limpijumnong and Jungthawan 2004; Serrano et al. 2004). This pressure-induced reversible transformation has received significant consideration primarily because hydrostatic compression is the most likely mode of loading for bulk ZnO. Recent work on GaN, MgO and ZnO thin films has revealed a previously unknown unbuckled layered structure (LY) resulting from extensive surface reconstructions to suppress surface polarity (Capaz et al. 1995; Goniakowski et al. 2004; Claeyssens et al. 2005; Freeman et al. 2006). So far, the existence of polymorphs other than WZ, ZB, and RS at various loading triaxialities has not been extensively studied. The recent fabrication of defect-free, single-crystalline nanowires, nanobelts and nanorings necessitates the analyses of responses to loading of various triaxialities, including bending and uniaxial tension since these materials have slender quasi one-dimensional geometries and are capable of undergoing significant elongations (Diao et al. 2004b; Kulkarni et al. 2005; Liang and Zhou 2006). Furthermore, novel shape memory effects (SME) and pseudoelasticity observed in nanowires as a consequence of polymorphic transitions also need to be characterized.

2.2.3 Pseudoelasticity

Traditionally, pseudoelasticity and shape memory effect (SME) are associated with shape memory alloys and elastomers (Otsuka and Wayman 1998). The term pseudoelasticity originates from the fact that the material is elastic in the sense that it returns to the original state after one loading-unloading cycle but it is only *pseudo*-elastic as the stress-strain response runs through a hysteresis loop (Muller 1989). Pseudoelastic

behavior has been extensively studied in shape memory alloys (SMA) such as CuZnAl, CuAlNi, NiMnGa where the austenitic to martensitic transformations result in this unique behavior (Muller 1989; Otsuka and Wayman 1998; Hirsinger et al. 2004; Musolff and Sahota 2004; Muller and Bruhns 2006). This effect has also been observed in polymers (Liu et al. 2004; Yiping et al. 2006), single crystal NiTi and polymer nanocomposites (Gall et al. 2002a; Gall et al. 2002b). Recent investigations of tensile response of single crystalline metal nanowires have shown that SME and pseudoelasticity exist in the nanowires as a consequence of their nanoscale dimensionality (Liang and Zhou 2005; Liang et al. 2005b; Park et al. 2005; Liang and Zhou 2006). Furthermore, experiments have shown that pseudoelasticity can be observed at the nanoscale in carbon nanotubes with recoverable strain up to 15% (Yakobson et al. 1996) and also in gold nanowires (Landman et al. 1996). Although, the mechanisms for pseudoelasticity are well-characterized at the macroscale, research on this phenomenon is quite underdeveloped for nanoscale structures. Furthermore, with the recent discovery of pseudoelastic behavior in normally brittle compounds such as ZnO, efforts have to be directed towards understanding the origin and nature of pseudoelasticity in such materials.

2.2.4 Micromechanical Continuum Modeling

The discovery of SME and pseudoelasticity has spurred various investigations from a metallurgical perspective. Such analyses give insights into the fundamental mechanisms for austenite to martensitic transformation and twin boundary movement. From a thermodynamics perspective, constitutive modeling has received due attention. Various approaches including the development of macroscopic phenomenological, microscopic thermodynamics based and micromechanics based models have been proposed. Specifically, the macroscopic models are based on curve fitting of experimental data with inference from phase diagrams of the materials. Such simplistic models are suitable for engineering applications where only the average response based

on experimental data is required. Microscopic models consider material behavior at lower scales with emphasis on the treatment of issues such as nucleation of defects, barrier for nucleation, driving forces on interfaces and interface motion. While such models provide insights on the fundamental physical mechanisms, they are too complex to be practically applicable to modeling pseudoelastic behavior. Micromechanics based modeling offers a practical alternative to modeling SME and pseudoelasticity. In this approach, micromechanics principles coupled with thermodynamics are used to describe the transformation. While this approach is not as rigorous as the microscopic models, its inherent simplicity has resulted in its widespread application to the study of various SMA.

The micromechanics based model is based on the availability of a non-convex free energy function which implies the possibility of phase transformations (Huo and Muller 2003). Statistical mechanics methods have been previously utilized to develop of such functions (Muller and Xu 1991). Recently, first principles calculations and atomistic simulations such as MD have been used to develop energy landscapes for various materials. This framework has been applied to the study of martensitic transformations in SMA. Specifically, strain energy functions with multiple local minima are developed and the phase transformation is analyzed through the study of evolution of these minima with applied load (Abeyratne and Knowles 1993; Abeyratne and Kim 1994; Abeyratne and Bhattacharya 2001). However, kinetic laws that relate the driving force and interface motion are extremely difficult to obtain and may preclude the use of such models. Alternatively, the response can be modeled by decomposing the behavior into static equilibrium states and interface propagation. Liang et al. (2007) have successfully applied this approach to the modeling of pseudoelastic behavior in FCC metal nanowires. Since the lattice reorientation that leads to the pseudoelastic behavior in such nanowires occurs through the propagation of a single twin boundary, interfacial energy considerations are not required in their model. However, during phase transformations in

ZnO nanowires or in other SMA in general, the evolution of a homogeneous body into a heterogeneous body with multiple phases involves the formation of interfaces which vary with applied load. In such cases, interfacial energy has to be explicitly considered. There are two approaches for modeling interfacial properties (Huo and Muller 2003):

(1) The interface is considered as a singular surface attributed with certain interface energy. Here, the free energy of the body is the sum of the energies of the phases involved and the interfacial energy;

(2) The interface is considered smooth but steep such that both strain gradients and strains have to be considered as state variables. Here, the free energy is the volume integral over the free energy density.

The first approach has been extensively used to model pseudoelasticity in SMA. Muller and Xu (1991) developed a 1D model to characterize the pseudoelasticity and the hysteretic dissipation in CuZnAl alloy. In this model, the interfacial energy contribution to the free energy is expected to be proportional to the interfacial area and a functional form has been derived using statistical arguments. This model has been successfully applied to the characterization of pseudoelastic behavior in CuAlNi alloy (Musolff and Sahota 2004). 3D models using an approach similar to that of Muller and coworkers have also been developed (Raniecki and Lexcellent 1994, 1998). Furthermore, a finite strain model using the same approach has also been developed and used to predict the stress-strain response of NiTi specimens (Muller and Bruhns 2006).

In this research, a combination of approaches developed by Muller and Xu (1991) and Liang et al. (2007) is used to model the pseudoelastic behavior of the ZnO nanowires. The goal of this continuum model is to capture the overall constitutive behavior and also account for size and temperature effects observed in MD simulations.

2.3 Nanoscale Thermal Response

2.3.1 Surface dominance of thermal transport

Thermal transport in semiconducting materials is governed by crystal vibrations which travel through a solid in the form of waves. The energy of such a lattice wave is quantized and each quantum is termed a phonon (Majumdar 1993). The kinetic theory of fluids relates the thermal conductivity λ to the phonon mean free path Λ through

$$\lambda = \frac{1}{3} C_v v \Lambda , \tag{2.1}$$

where C_v is specific heat and v is the velocity of heat carriers (for ZnO, the heat carriers are phonons and hence v represents the average phonon group velocity). At the macroscale, the heat transport through lattice waves can be modeled using Fourier's law as

$$q = -\lambda \nabla T , \tag{2.2}$$

where q is the heat flux, λ is the thermal conductivity and ∇T is the temperature gradient. However, Fourier's law has been observed to break down at the nanoscale where the characteristic sizes approach mean free paths of the phonons. This has led to the development of various experimental, theoretical and computational approaches to estimate the thermal conductivity which account for the nanoscale surface effects. Theoretical approaches focus on developing solutions to the Boltzmann transport equation (BTE) for nanostructures (Walkauskas et al. 1999; Cahill et al. 2003). There is also a great interest to experimentally investigate electron and phonon transport and heat dissipation phenomena in these materials. Traditional thermal conductivity measurements can be performed by a variety of techniques including the modified angstrom's method, photo thermal beam deflection, optical pump–probe, hot-stripe approach (Asnin et al. 1999). However such measurement techniques cannot resolve thermal features below 100 nm (Cahill et al. 2003). To address these issues, new techniques such as scanning thermal

microscopy (Asnin et al. 1999), 3ω techniques (Luo et al. 1999) and thermometry (Shi et al. 2003) have been used. Computational approaches to heat-transfer problems span the range from numerical solutions of Fourier's law to calculations based on the Boltzmann transport equation to atomic-level simulations which require a fairly sophisticated understanding of the fundamental phonon processes. MD simulations, in contrast, do not require any *a priori* understanding of heat transport and are ideal for investigating the fundamental heat-transfer mechanisms. However, MD does have the significant limitation of being entirely classical, with each vibrational mode equally excited; thus it is only rigorously applicable to solids above the Debye temperature (Cahill et al. 2003). The two most commonly used approaches used in MD simulation based evaluation of the thermal conductivity are the Green–Kubo approach (Kubo et al. 1985) in which the equilibrium fluctuations in the heat current are analyzed, and the direct method (Schelling et al. 2002) which mimics experiment by imposing a temperature gradient on the system and determining the thermal conductivity from Fourier's Law [Eq. (2.2)]. The direct method is easier to implement but involves significantly high temperature gradients (10^6 K/m) due to the nanometer scale characteristic sizes. Such high temperature gradients can result in non-linear response and the application of Fourier's law would be unrealistic. The Green-Kubo approach, on the other hand, is an equilibrium approach where the system is in the linear response regime and therefore can be reliably employed to determine the thermal conductivity of the nanostructures. Recently, the Green-Kubo approach using MD simulations has been successfully implemented for studying the thermal response of silicon nanowires (Volz and Chen 1999b, 1999a). Results obtained in these works show that the effect of surfaces is appropriately considered in the thermal conductivity calculation for a range of nanoscale sizes and temperatures justifying the applicability of this method for nanostructures.

2.3.2 Model for Nanoscale Heat Transfer

Heat transport in semiconducting and insulating materials has predominantly been modeled using the Boltzmann Transport Equation (BTE) with a Bose-Einstein distribution for phonons (Ziman 1960). Recently, BTE was modified for surface effects so as to predict the thermal conductivity of nanostructured components (Walkauskas et al. 1999; Zou and Balandin 2001). The solutions obtained from BTE have been under a linearized relaxation time approximation which has proven to overestimate conductivity at low length scales (Majumdar 1993). A new approach was developed by Majumdar (1993) by treating phonon dominated thermal behavior as radiative heat transfer. Using the analogy between photons and phonons as wave packets of energy, he developed an equation for phonon radiative transport (EPRT) similar to the BTE. The EPRT was further modified to account for phonon behavior in nanowires and nanorods through the specification of appropriate boundary conditions as well as the incorporation of a boundary scattering term in the expression for the relaxation time (Lu et al. 2002; Lu et al. 2003). In the present work, this EPRT model has been extended to fit the thermal conductivity data obtained for ZnO wires through MD simulations.

2.3.3 Thermomechanical Coupling

Thermal conductivity of semiconductors is dominated by phonon scattering events. In other words, the lattice thermal conductivity contributes towards the conductivity of the material whereas the electronic contribution is minimal. Consequently, any alteration in the lattice structure will modify the thermal response of a semiconductor. It is well known that applied mechanical stress on a semiconductor can vary its energy band and lattice structure (Aflatooni and Nathan 1995). Such distortions in the lattice induce changes in the phonon frequency leading to the observed variations in its thermal transport characteristics (Fjeldly et al. 1973; Ramdane et al. 1983; Sood and Roy 1992). In particular, transitions in thermal conductivity and the coefficient of thermal

expansion have been reported for the quartz-coesite, olivine-γ-spinel, coesite-stishovite, B1-B2 and pyroxene-garnet transformations in minerals under pressure (Jeanloz and Roufosse 1982; Roufosse and Jeanloz 1983; Andersson 1985; Slack and Ross 1985). Although, the mechanisms of thermal transport are well understood at the macroscale, the effect of applied stress has not been studied extensively at the nanoscale. Recently, the effect of hydrostatic stresses on the thermal conductivity of nanostructures was also analyzed (Picu et al. 2003). However, since periodic images of the structure were considered in the simulation of the nanostructure, the effect of surfaces was neglected and hence the response is not reflective of nanoscale thermal characteristics which are significantly dominated by surface scattering irrespective of the applied loading. The characterization of the thermal response as a function of lattice strains is indispensable in nanowires since the operational conditions in devices may result in distortion of the lattice and in some cases result in phase transformations and therefore entirely change the thermal characteristics which the device design was based on. Alternatively, the thermomechanical coupling can be regarded as a mechanism for tuning the response of nanocomponents in a variety of NEMS through the application of mechanical input.

CHAPTER 3 : COMPUTATIONAL FRAMEWORK

Experimental evaluations of material response at the nanoscale are challenging or even infeasible due to the practical difficulties involved in the manipulation and testing of nanostructures. Even with the recent cutting-edge high-resolution transmission electron microscopes (HRTEM) and atomic force microscopes (AFM), it is challenging to experimentally track deformations of nanostructures in real time and predict their mechanical responses. Furthermore, experimental evaluations of thermal response of the nanostructures are practically difficult and also suffer from the inherent drawback of contact resistance. Atomistic simulations provide an alternate medium of analyzing the properties of materials in reasonably realistic conditions. In MD simulations, the motion of individual atoms can be monitored such that even complex phenomena such as phase transformations in nanostructures are easily resolved. MD simulations also allow for the study large systems as compared to other atomistic simulations such as first-principles calculations and have therefore emerged as an effective tool for the characterization of the mechanical and thermal behaviors of nanostructures (Mehrez et al. 1997; Branicio and Rino 2000; Komanduri et al. 2001, 2003; Liang and Zhou 2003; Diao et al. 2004a; Diao et al. 2004c; Gall et al. 2004; Ju et al. 2004). Consequently, in this research, MD simulations are considered to predict the thermomechanical response of ZnO nanostructures.

MD simulations are carried out using a general purpose parallel MD simulation package DL_POLY_2 developed at Daresbury Laboratory by W. Smith, T.R. Forester and I.T. Todorov. DL_POLY_2 is based on a replicated data parallelism designed for distributed memory parallel machines which offers excellent scalability from workstations to massively parallel supercomputers (Smith and Forester 1996). The

computations are carried out at the NAVO, ARL, AHPCRC and ASC major shared resource centers (MSRCs)

This chapter discusses some important aspects of the MD simulation framework including interatomic potentials, their calibration, generation of nanowire and nanorod structures and crystallographic analysis techniques. Mechanical and thermal response analysis techniques involving quasistatic loading schemes, density functional theory (DFT) calculations and the Green-Kubo framework are also discussed.

3.1 Interatomic Potential

MD simulations use Newton's second law ($\mathbf{f}_i = m_i \ddot{\mathbf{r}}_i$) to determine the positions and velocities of atoms at finite temperatures. The forces on atoms are calculated from the gradient of the potential energy ($\mathbf{f}_i = -\partial U / \partial \mathbf{r}_i$) where the potential energy is expressed as $U = \sum_{i=1}^{N} \sum_{\substack{j=1 \\ j \neq i}}^{N} u\left(r_{ij}\right)$. Here, $u\left(r_{ij}\right)$ is the pair wise interaction energy determined from the Buckingham-type interatomic potential of the form

$$u(r_{ij}) = \frac{q_i q_j}{4\pi\varepsilon_0 r_{ij}} + A\exp\left(\frac{-r_{ij}}{\rho}\right) - \frac{C}{r_{ij}^6}. \tag{3.1}$$

Here, r_{ij} is the distance between two ions, q_i is the charge on ion *i* and A, ρ and C are potential parameters (Binks and Grimes 1993; Binks 1994). The first term in Eq. (3.1) considers the long-range Coulomb interactions due to electric charges and the second and third terms model short-range interactions. The parameters *A*, ρ and C of the potential are fitted to the structure and properties of ZnO using classical and quantum mechanical methods (Binks 1994) and are listed in Table 3.1. Anion-anion interactions include both the long-range and short-range terms. Anion-cation interactions are modeled using the Born-Mayer form which neglects the last (attractive) term. Cation-cation interactions involve only the long-range charge effect. Calculations of the long-range Coulomb force

are carried out using Ewald summation technique which is computationally efficient and unconditionally convergent. The periodicity required for the Ewald sum is introduced using a supercell concept, in which the simulation box is defined considerably larger than the nanowires and nanobelts.

Table 3.1 Short range interaction parameters for ZnO (Binks 1994)

Species		$A(eV)$	$\rho(\text{Å})$	$C(eV\,\text{Å})$
O^{2-}	O^{2-}	9547.96	0.21916	32.0
Zn^{2+}	O^{2-}	529.70	0.3581	0.0
Zn^{2+}	Zn^{2+}	0.0	0.0	0.0

The Buckingham potential has been shown to accurately predict the equilibrium lattice energy, cell parameters, elastic and dielectric constants of the wurtzite structure (see Table 3.2 and Table 3.3). Figure 3.1 shows the lattice parameters a, c and $u = uc/c$ that uniquely define the WZ lattice. The corresponding values from first principles calculations and experiments are listed in Table 3.2.

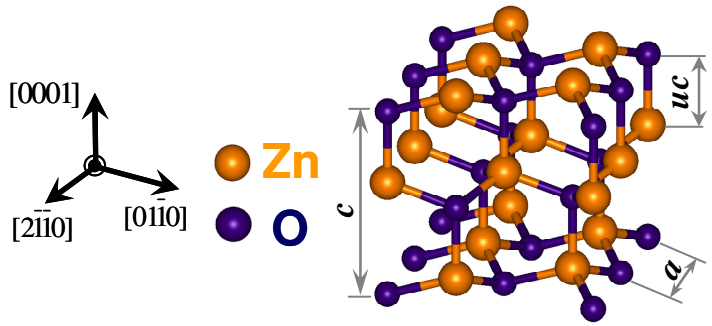

Figure 3.1 Zn and O atomic positions in wurtzite lattice structure. The lattice parameters a, c and uc are indicated.

Extensive perfect lattice, defect and monovalent ion incorporation simulations have been successfully carried out using this potential (Binks and Grimes 1993; Binks

1994; Grimes et al. 1995). The potential also effectively predict surface properties such as surface energies (Binks 1994). This is especially important in the simulations of nanowires whose high surface-to-volume ratios are known to significantly affect behavior. The interatomic potential also predicts values of lattice constants of other polymorphs of ZnO including zinc blende and rocksalt structures which are in excellent agreement with experimental observations (see Table 3.4).

Table 3.2 Calculated and experimental wurtzite lattice parameter values for ZnO (Binks 1994).

Lattice Parameter	Calculated	Experimental	% Error
a (Å)	3.271	3.253	+0.6
c (Å)	5.139	5.213	-1.4
u	0.389	0.380	+2.4
c/a	1.571	1.603	-2.0
Volume ($Å^3$)	47.618	47.773	-0.3

Table 3.3 Calculated and experimental wurtzite elastic constant values (in GPa) for ZnO (Binks 1994)

Elastic Constant	Calculated	Experimental	% Error
C_{11}	232.5	209.7	+10.9
C_{12}	95.20	121.1	-21.4
C_{13}	85.60	105.1	-18.6
C_{33}	210.4	210.9	-0.20
C_{44}	74.60	42.50	+75.5
C_{66}	68.60	44.30	+54.9

Table 3.4 Calculated and experimental zinc blende (ZB) and rocksalt (RS) lattice parameter values for ZnO (Binks 1994).

Structure	Lattice Parameter	Calculated	Experimental	% Error
RS	*a* (Å)	4.320	4.280	+0.9
	Volume ($Å^3$)	80.62	78.40	+2.7
ZB	*a* (Å)	4.570	4.620	-1.1
	Volume ($Å^3$)	95.44	98.61	-3.3

3.2 Generation of Nanostructures

The as-synthesized nanowires and nanorods are single-crystalline and wurtzite-structured with lattice constants a = 3.249 Å and c = 5.206 Å. The calculations concern the quasi-static uniaxial tension of nanowires with the $[01\bar{1}0]$ growth orientation and nanorods with the [0001] growth orientation. The nanostructures considered in this work are perfect single crystals without any defects. While thermodynamic considerations dictate that point defects such as vacancies should exist in any structure for temperatures greater than 0 K, such point defects are neglected. This is because the number of defects in the nanowires is expected to be extremely small. Furthermore, analysis of mechanical response of FCC metal nanowires have shown that the presence of such defects do not alter their behavior which is dominated by surfaces and can be neglected (Gall 2007).

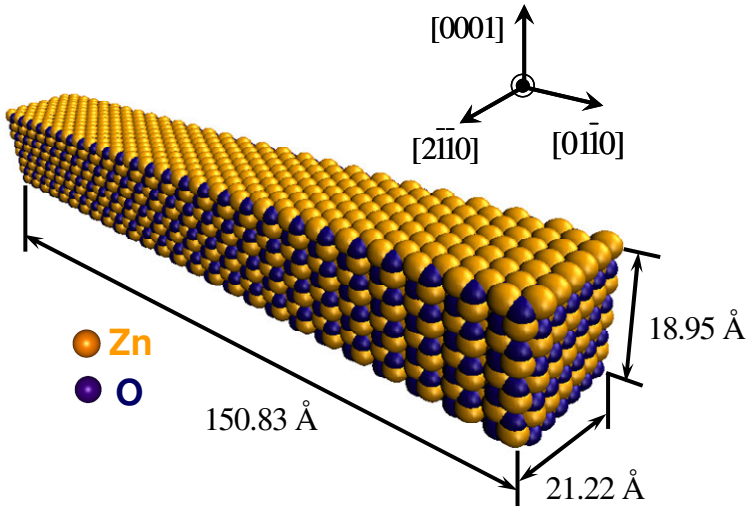

Figure 3.2 Configuration of a $[01\bar{1}0]$ nanowire with lateral dimensions of 21.22×18.95 Å after geometric construction and before initial relaxation.

The $[01\bar{1}0]$-oriented nanowires have rectangular cross-sections and $\{2\bar{1}\bar{1}0\}$ and $\{0001\}$ lateral surfaces. Their thickness is between 5-20 nm with typical width-to-thickness ratios of 1-10 (Pan et al. 2001). The wire structure can be obtained by repeating the unit wurtzite cell along the $[01\bar{1}0]$ crystallographic direction as shown in Figure 3.2.

The minimum cross-sectional size analyzed (21.22×18.95 Å) is chosen such that the short range cutoff distance is smaller than the smallest wire dimension and long-range interactions are properly considered. Periodic boundary conditions (PBCs) are specified in the axial direction to approximate the behavior of long wires. A small periodic length can significantly affect the calculated responses by introducing image effects since PBCs effectively truncate the phonon wavelength spectrum (Picu et al. 2003). Calculations show that any length above 100 Å is sufficient for avoiding such image effects. The simulation cell is therefore chosen as 150.83 Å in the axial direction and cross-sectional dimensions of 21.22×18.95, 31.02×29.42 and 40.81×39.89 Å are used to evaluate the size effect.

The [0001]-oriented nanorods have hexagonal cross-sections with a six-fold symmetry around the [0001] axis and six $\{01\bar{1}0\}$ lateral surfaces (Wei et al. 2006). The nanorod is generated by repeating a unit wurtzite cell along the [0001], $[01\bar{1}0]$ and $[2\bar{1}\bar{1}0]$ directions (see Figure 3.3). Periodic boundary conditions are used along the axial direction with a computational cell length of 145.8 Å. To study the size effect, five lateral dimensions (d = 19.5, 26.0, 32.5, 39.0 and 45.5 Å) are considered. The analyses are carried out in the 100-1500 K temperature range to quantify the effect of temperature on the behavior.

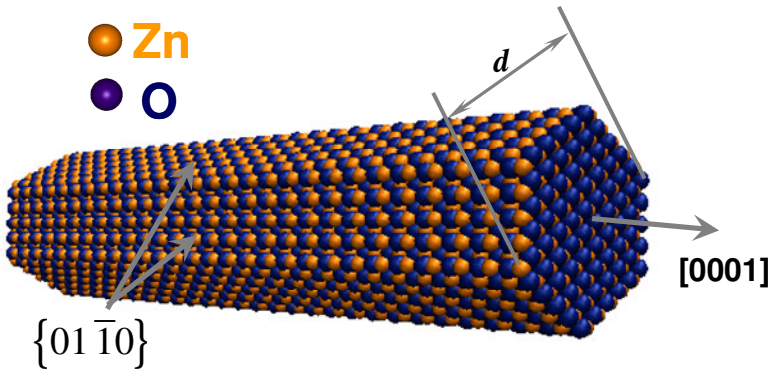

Figure 3.3 Configuration of a [0001] nanorod with d = 32.5 Å after geometric construction and before initial relaxation.

3.3 Crystallographic Characterization

Changes in lattice structures with applied strain are characterized using average lattice constants, radial distribution functions [RDF, (Leeuwen et al. 1959)] and coordination number. The average lattice constants are calculated at each strain increment during loading and unloading of the nanostructures by averaging local lattice constants over the bulk volume of the wire. Surface layers are not included in this calculation and the local lattice parameters are computed from coordinates of atoms in the wire core (see Figure 3.4).

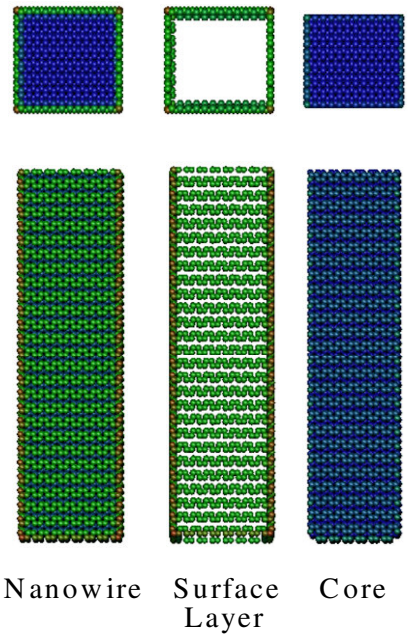

Figure 3.4 Decomposition of a nanowire into surface atoms and interior atoms using the coordination number (CN), the surface atoms have CNs below 4 and the core atoms have CNs equal to 4.

3.3.1 Radial Distribution Function

The RDF describes how atoms in a system are radially packed around each other. It measures the density of atoms in a spherical shell of radius r and thickness dr surrounding an atom in the structure, i.e.

$$g(r) = \frac{n(r, r+dr)}{V_S} \Big/ \frac{N}{V}, \tag{3.2}$$

where $g(r)$ is the RDF, $n(r, r+dr)$ is the number of atoms in the spherical shell, $V_S = 4\pi r^2 dr$ is the volume of the spherical shell, N is the total number of atoms in the system and V is the volume of the structure (Figure 3.5). The RDFs are generated at the end of the equilibration stage of a relevant strain increment when a steady state has been achieved during loading and unloading of the nanowires.

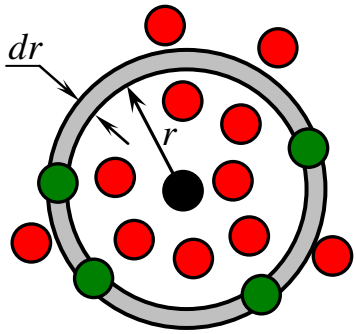

Figure 3.5 Calculation of the RDF. A ring centered on the center atom is drawn with radius r and thickness dr, and the atoms positioned within this spherical shell are counted.

3.3.2 Coordination Number

RDF is a good technique to characterize the overall average structure and also to evaluate the average lattice parameter values. However, it is not appropriate for identifying local structure changes or structural defects, which are very important to understand the mechanisms underlying the phase transformations. There are several techniques to identify defects such as techniques relying on electron density, potential energy, dislocation density tensor, atomic level stress tensor, centrosymmetry and coordination number. Here, we use the coordination number in order to identify local changes in structure such as the nucleation of a new phase in the nanowires.

Coordination number (CN) or ligancy is the number of atoms, ions, or molecules that a central atom or ion holds as its nearest neighbors in a crystal. CN is calculated through a distance based search routine, wherein all atoms lying inside a sphere with radius corresponding to the nearest neighbor distance are summed. For example, in the case of WZ-ZnO, the nearest neighbor distance is the Zn-O bond distance and the number of primary neighbors is 4 [see Figure 3.6(a)]. Consequently, WZ-ZnO is said to be tetrahedrally coordinated. On the other hand, for the HX structure in Figure 3.6(b), the number of neighbors is 5 and as a result, the CN for HX is 5. Similar to RDF calculations, the CN is also calculated at the end of the equilibration stage when a steady state has been achieved during loading and unloading. In particular, both the CN and the RDF for the parent structure after initial relaxation and for the transformed structure are studied to characterize the structural changes associated with the phase transformation.

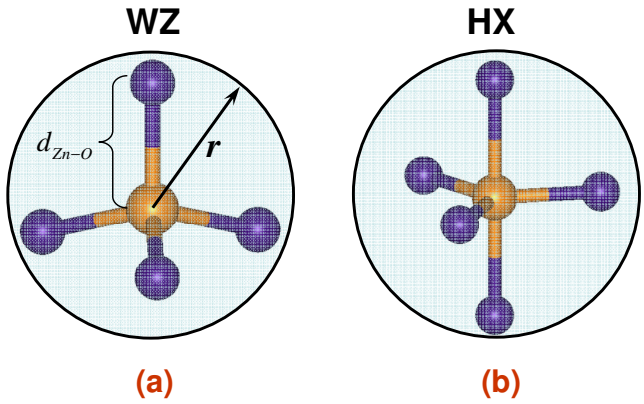

Figure 3.6 A schematic illustration of the coordination number calculation for an O atom surrounded by Zn atoms in its coordination sphere in (a) WZ and (b) HX structure.

3.4 Pre-Loading Relaxation

Since the crystallographically constructed nanowires may not be in equilibrium, pre-loading relaxations are carried out to obtain the wires' free standing configurations. The relaxations occur at desired temperatures without external loading, until

thermodynamic quantities (such as energy, stress, and temperature) indicate that statistical steady states have been reached. A relaxation time of 3 *ps* is found to be adequate for achieving equilibrium states for the ranges of wire size and temperature considered. During the relaxations, minimization of the wires' energy occurs through surface reconstruction and adjustment of the lattice spacing in the wire core. The surface reconstruction manifests in the forms of decreases in the interlayer spacing between outer surface layers and in-plane contractions of the surfaces (Kulkarni and Zhou 2006b). Such morphological changes on surfaces and in the wires' cores are also monitored. This is especially important for nanostructures since their surface-to-volume ratios are high and extensive surface, and in some cases, core reconstructions may occur. For example, [100]-oriented FCC metal nanowires are known to reconstruct into [110] orientations as a consequence of surface energy minimization (Diao et al. 2003, 2004b; Liang and Zhou 2005; Liang et al. 2005b).

3.5 Mechanical Response Analysis

3.5.1 Quasi-static Loading Scheme

In a MD framework, deformations analyzed usually involve dynamic conditions with strain rates up to 10^9 s^{-1}. Such high strain rates are often necessary to reach required strain levels with available computer resources. However, the higher strain rates cause rapid and high temperature increases and may also result in quantifications that are not physically interpretable. In the present work, MD simulations of deformation under quasi-static tensile loading are carried out. The results obtained can therefore be related to those obtained through experimental techniques.

Approximate quasi-static tensile loading in each deformation increment is achieved though successive loading and equilibration steps using a combination of algorithms for NPT and NVE ensembles (Haile 1997). Specifically in each deformation

increment, stretching at a specified rate of 0.005 */ps* is first carried out for 0.5 *ps* using a modified version of the NPT algorithm (Melchionna et al. 1993; Spearot et al. 2005). Subsequently, with the strain maintained constant, the nanowire is relaxed for 3 *ps* via an algorithm for NVE ensemble (Haile 1997) at the specified temperature. This equilibration duration is chosen such that a statistically steady state is reached and no further structural changes occur. It is possible that the magnitude of the strain increment in each step may affect the calculated stress-strain response. To minimize this error, calculations using series of strain increments between 0.35% and 0.1% were carried out. Based on the results, a strain increment of 0.25% and an equilibration period of 3 *ps* per loading step are found to minimize fluctuations in the calculated response and are used in the analysis reported. Since the loading proceeds in a series of equilibration steps, this process essentially simulates quasi-static loading of the specimen. Unloading is implemented in a similar manner with a reduction in strain for each unloading step. The virial formula is used to calculate the stress (Zhou 2003).

3.5.2 Thermodynamic Favorability

First principles calculations are carried out to evaluate the total energy of the material in its natural and deformed states. This research has been carried out in collaboration with physicists in Suranaree University of Technology, Thailand. The calculations are based on the density functional theory (DFT) as implemented in the VASP code (Kresse and Furthmüller 1996) with local density approximation (LDA) and ultrasoft pseudopotentials (Vanderbilt 1990). Zinc *3d* electrons are treated as valence electrons. Cutoff energies for the plane wave expansion is 400 eV. The k-point sampling set is based on a $7\times7\times7$ division of the reciprocal unit cell which gives approximately 100 inequivalent k-points.

The stability of each crystal structure can be determined by analyzing enthalpy as a function of lattice parameter ratios *c/a* and *b/a* (Figure 3.1). The enthalpy per unit cell (2 cation-anion pairs) under uniaxial loading is

$$H(c/a, b/a) = E(c, b, a, u, v) - \frac{1}{2} f_i q_i, \tag{3.3}$$

where E is the formation energy, f_i is the uniaxial force per unit cell along the I direction, q_i is the lattice parameter in the I direction, and $f_i q_i$ (summation not implied) is external work. For tension along the $[01\bar{1}0]$ (or b) axis, $i = b$, $f_b = \sigma_b \times (ac)$ and $q_b = b$, with σ_b being the tensile stress. For tension along the [0001] (or c) axis, $i = c$, $f_c = \sigma_c \times (ab)$, and $q_c = c$, with σ_c being the tensile stress.

For each pair of *c/a* and *b/a*, the equation of states (i.e. the energy as a function of cell volume) is determined so that, under applied tension loading, the cell volume (V) can be relaxed to minimize H. For each strained configuration (each *c/a*-*b/a* pair), the energies associated with at least four different unit cell volumes are calculated. An equation of state (energy-volume relation) is obtained by a 3rd-degree polynomial fit. Under loading, the volume that minimizes H is not the same as the volume that minimizes E. The equation of state allows the minimum enthalpy for each combination of *c/a*-*b/a* pair and loading condition to be obtained. A total of over 170 equations of states, each of which describes a specific strained configuration in the *c/a* – *b/a* space, are calculated.

For each *c/a* and *b/a* pair, the internal parameters u and v and the unit cell volume V are allowed to relax so that the configuration that yields the minimum H is obtained. For a given load condition, the minima on the enthalpy surface with *c/a* and *b/a* as the independent variables identify the corresponding stable and metastable structures. For the analyses at hand, the parameter ranges considered are [1.00, 1.63] for *c/a* and [1.00, 1.73] for *b/a*, with the increments of 0.05 for *c/a* and 0.10 for *b/a*. This meshing of the structural space results in approximately 170 strained configurations. For tensile loading

along the *b*-direction, additional configurations with *b/a* up to 2.30 are also investigated, increasing the number of total configurations to 200. Out of these 170 or 200 configurations, those around (*c/a, b/a*) ≈ (1.63, 1.73), (1.2, 1.73) and (1.00, 1.00) are more carefully analyzed since these three parameter sets define the neighborhoods of stable WZ, HX and BCT-4 structures, respectively, for the given load condition.

3.6 Thermal Response Analysis

The evaluation of the thermal conductivity uses the Green-Kubo approach which is based on the fluctuation-dissipation theorem (Kubo et al. 1985; Schelling et al. 2002). Specifically, the thermal conductivity is written as

$$\kappa_{\mu\nu} = \frac{1}{Vk_B T^2} \int_0^\infty \left\langle J_\mu(t) J_\mu(0) \right\rangle dt \,, \tag{3.4}$$

where V is system volume, T is temperature, k_B is Boltzmann constant, $J_\mu(t)$ is the μ^{th} (μ=1, 2, 3) component of the heat current $\mathbf{J}$ and $\left\langle J_\mu(t) J_\mu(0) \right\rangle$ is the auto-correlation function for $J_\mu(t)$ with $\langle\ \rangle$ denoting ensemble time average. The heat current is calculated as

$$\mathbf{J}(t) = \sum_{i=1}^{N} \left(\mathbf{v}_i E_i + \frac{1}{2} \sum_{j=1, j\neq i}^{N} \mathbf{r}_{ij} \left(\mathbf{F}_{ij} \cdot \mathbf{v}_i \right) \right). \tag{3.5}$$

Here, $\mathbf{r}_i$, $\mathbf{v}_i$ and E_i are the position vector, velocity and total energy of atom *I,* respectively; $\mathbf{r}_{ij} = \mathbf{r}_j - \mathbf{r}_i$ and $\mathbf{F}_{ij}$ is the force exerted on atom *I* by atom *j*. The first term in Eq. (3.5) represents the convection contribution to heat flow. This term is inconsequential in solids and is ignored in conductivity calculations.

The upper limit for the integral in Eq. (3.4) extends to infinity since theoretically the time required for a system to attain thermal equilibrium tends to infinity. To calculate thermal conductivity in a realistic manner, however, the integral is truncated after a certain time period which is defined as the delay time τ_m and the system is assumed to

have reached equilibrium at that time. The choice of the delay time depends on the material system analyzed since it is a measure for a system's inherent thermal response. To calculate thermal conductivity for each delay time, the autocorrelation function values are averaged over a number of time origins within the simulation window. Hence, the average measure of thermal conductivity can be expressed as a function of delay time as

$$\kappa_{\mu\nu}(\tau_m) = \frac{\Delta t}{Vk_B T^2} \sum_{m=1}^{M} \frac{1}{N-m} \sum_{n=1}^{N-m} J_\mu(m+n) J_\nu(n) , \tag{3.6}$$

where Δt is the simulation timestep, $N\Delta t$ is the total simulation time and the delay time $\tau_m = M\Delta t$.

The thermal analysis presented here is limited to temperatures near or above the Debye temperature θ_D ($= 420K$ for ZnO). Consequently, temperature can be calculated through mean kinetic energy and the theorem of equipartition of energy as

$$\frac{3}{2} N k_B T = \frac{1}{2} \sum_{i=1}^{N} m_i v_i^2 , \tag{3.7}$$

with N being the number of atoms in the system and m_i being the mass of atom i. Temperatures significantly below θ_D, for which quantum mechanical corrections may be needed, are not considered here.

3.6 Coupled Thermomechanical Response

The deformation of the nanowires is approximated as a quasi-static process with each strain increment followed by a relaxation stage until a statistically steady state is reached. Since the loading proceeds in a series of equilibration steps, an equilibrium approach such as the Green-Kubo method can be applied to determine the thermal response of the nanowires as a function of applied strain. Also, since the MD simulations carried out to determine heat flux do not require any *a priori* understanding of heat transport or the configurational characteristics, this approach is ideal for investigating the heat-transfer in materials undergoing straining or even phase transformations. Hence, the

Green-Kubo approach implemented in MD simulations is used to characterize the coupled thermomechanical response of the nanowires.

CHAPTER 4 : NOVEL PHASE TRANSFORMATIONS

The assumption of crystal structures by a material reflects a complex interplay of intrinsic factors such as composition, band structure, valence electrons, bonding states, and structural symmetry and extrinsic factors such as temperature and loading. A change in any of the intrinsic factors through external stimuli such as mechanical loading and temperature changes may result in failure through bond breaking or trigger a transformation to a different structure, giving rise to polymorphism. At the macroscopic scale, failure is dominant since atomic mobility is relatively low and defects are more prevalent. At the nanoscale, however, high surface-to-volume ratios and nearly defect-free structures lead to higher atomic motilities and more pronounced polymorphic transitions.

Recent synthesis of quasi-1D nanostructures such as ZnO nanowires, nanobelts and nanorods necessitates understanding of the response of ZnO to uniaxial tensile loading (Mao et al. 2003; Wang 2004b; Chen et al. 2006b). Since these nanostructures are single-crystalline and nearly defect-free, they are endowed with high strengths and the ability to undergo large deformations without failure. Also, their high surface-to-volume ratios enhance atomic mobility and promote phase transformations under loading along certain crystalline directions. Consequently, polymorphs previously unknown for bulk materials have been revealed. This research reports two novel phase transformations observed in ZnO nanowires: (1) Transformation from WZ to a graphitic phase (HX) within the $P6_3/mmc$ space group during uniaxial tensile loading of $[01\bar{1}0]$-oriented nanowires and (2) Transformation from WZ to a body-centered-tetragonal phase (BCT-4) within the $P4_2/mnm$ space group during the tensile loading of [0001]-oriented nanorods. The results here show that the extent of polymorphism in ZnO is much more pronounced than previously known. With the discovery of these new phases, a more complete picture

has emerged for the polymorphism of ZnO under the influence of mechanical loading with all realistic triaxialities.

This chapter focuses on characterizing the tensile response of the $[01\bar{1}0]$- and [0001]-oriented nanowires and nanorods leading to the observed phase transformations. Crystallographic analyses of the newly discovered HX and BCT-4 structures and corresponding transformation paths including atomic motions responsible for the transformations are carried out. First principle calculations involving density functional theory are carried out to determine the energetic favorability of the parent and transformed phases. Characterization of the responses of the relevant phases is crucial since the performance and functionalities of these slender quasi one-dimensional materials as components in ultra-sensitive chemical and biological sensors, nanoresonators, field effect transistors and nanogenerators (Comini et al. 2002a; Arnold et al. 2003; Bai et al. 2003; Wang and Song 2006) are either significantly affected by or utilize the phase transitions (Diao et al. 2004b; Kulkarni et al. 2005; Liang and Zhou 2006).

4.1 Wurtzite to Graphitic Phase Transformation

4.1.1 Stability of $\{0001\}$ Surfaces

The $[01\bar{1}0]$ nanowires are dynamically relaxed with traction free boundary conditions to obtain their free-standing states. During equilibration, minimization of energy occurs through surface reconstruction and adjustment of the lattice spacing in the wire core. The surface reconstruction manifests in the forms of decreases in the interlayer spacing between outer surface layers and in-plane contractions of the surfaces. As shown in Figure 4.1, the spacing between the two outermost layers of (0001) planes decreases by 73 % resulting in higher atomic densities in the surfaces compared to the wire core (Kulkarni et al. 2005).

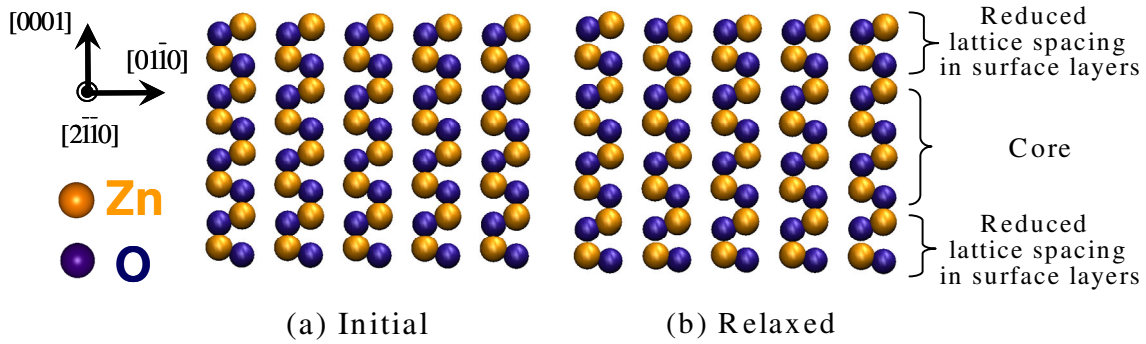

Figure 4.1 Surface reconstruction of a 21.22×18.95 Å nanowire at 100 K relative to its configuration in bulk ZnO, the images correspond to the states of the wire after (a) geometric construction (before initial relaxation) and (b) after initial relaxation.

The surface reconstruction seen here is a consequence of the reduced charge transfer and imbalance of ionic forces on the surfaces where atoms have fewer neighbors relative to those in the core. The reduced coordination of the surface atoms is also responsible for the in-plane relaxation of the surface atoms. As shown by Sander (Sander 2003), the surface energy curve has a positive slope at zero surface strain, i.e., minimum surface energy occurs at a compressive surface strain. Consequently, in-plane contraction leads to a surface configuration considerably different from that in the bulk. Both effects become significant at small sizes since the surface-to-volume ratio increases with decreases in size. Specifically, as the size decreases from 50 to 10 Å, the fraction of surface atoms increases from 10 to 45% (see Figure 4.2), indicating that an increasingly larger portion of atoms reside on the surface rather than in the interior. As a result of this, surface energy constitutes a major portion of the total energy of the nanowires and plays a significant role in determining the configuration of the nanowires. Owing to their higher fractions, the behavior of surface atoms plays an increasingly dominant role in determining phase stability in the nanowires.

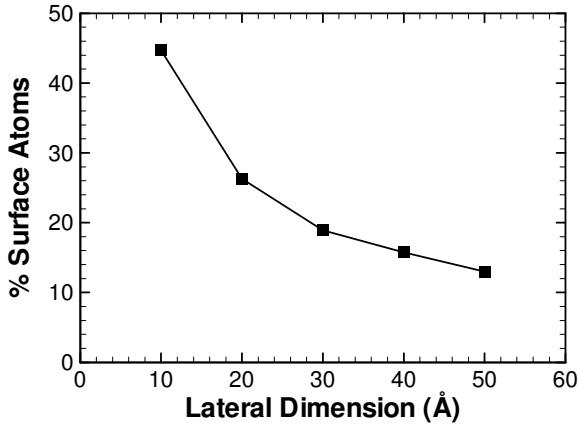

Figure 4.2 Fractions of surface atoms as a function of lateral dimensions of the nanowires.

4.1.2 Tensile Response of $[01\bar{1}0]$-oriented Nanowires

Figure 4.3(a) shows the tensile stress-strain (σ-ε) response of a nanowire with a 21.22×18.95 Å cross-section at 100 K. The region between A and B corresponds to elastic stretching of the WZ structure. Loading beyond B results in a stress drop from 10.02 to 6.98 GPa (B→C) at ε=5.14%. This softening behavior corresponds to the nucleation of the HX phase. As the deformation progresses, the transformed region sweeps through the entire wire length (C→D) and the transformation completes at ε=9.71% (σ=9.65 GPa). Figure 4.3(b) shows an intermediate stage during the transformation. Further deformation occurs through the elastic stretching of the transformed structure (HX) and ultimate fracture occurs at ε=16% (σ=15.29 GPa, not shown) through cleavage along $\{\bar{1}2\bar{1}0\}$ planes. Unloading from any strain prior to the initiation of failure, e.g. point E with ε=14.5%, is first associated with the recovery of the elastic deformation within the HX structure (E→F). A reverse transformation from HX to WZ (F→G→H) initiates at ε=5.77% (σ=4.59 GPa, point F) and completes at ε=0.6% (σ=1.15 GPa, point H). Unloading beyond H occurs through elastic deformation within the WZ structure (H→A). Strains up to 14.5% can be recovered,

highlighting a very unusual aspect of the behavior of ZnO which normally is quite brittle. Obviously, the large recoverable strains observed here are associated with a unique structural transformation process which occurs only in $[01\bar{1}0]$ nanowires under uniaxial tensile loading.

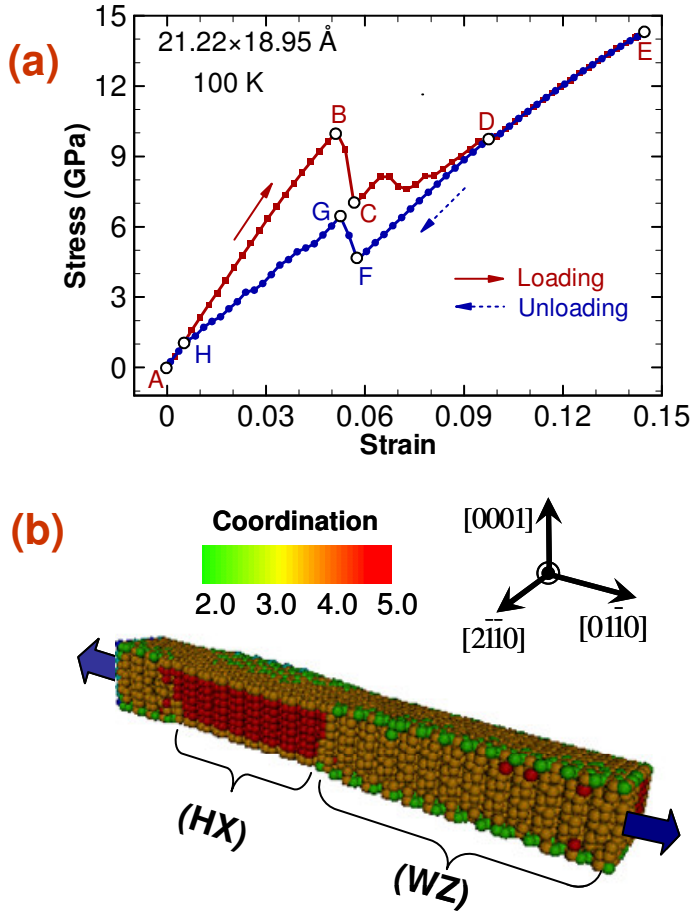

Figure 4.3 (a) Tensile stress-strain response of a 21.22×18.95 Å nanowire at 100 K during loading-unloading and (b) Nanowire with HX and WZ phases [transformation in progress under tensile loading (point C in Fig. 2 with a strain of 5.9%)].

4.1.3 Crystallographic Characterization

Figure 4.4(a) shows three parameters (a, c, and $u = uc/c$) typically used to define hexagonal structures (WZ), with uc denoting the offset between the Zn and O basal planes. Additional parameters b and v, with vb being the offset between Zn and O atoms

along the $[01\bar{1}0]$ axis, are introduced to delineate the difference between the HX and RS structures (Limpijumnong and Lambrecht 2001a; Limpijumnong and Jungthawan 2004). *a, b* and *c* are the dimensions of the hexagonal unit cell along the $[2\bar{1}\bar{1}0]$, $[01\bar{1}0]$ and [0001] directions, respectively. Additionally, two layers of atoms perpendicular to the $[01\bar{1}0]$ direction and two layers perpendicular to the $[2\bar{1}\bar{1}0]$ direction are shown in Figure 4.4(b) and Figure 4.4(c), respectively, to delineate the atomic motions associated with the transformation.

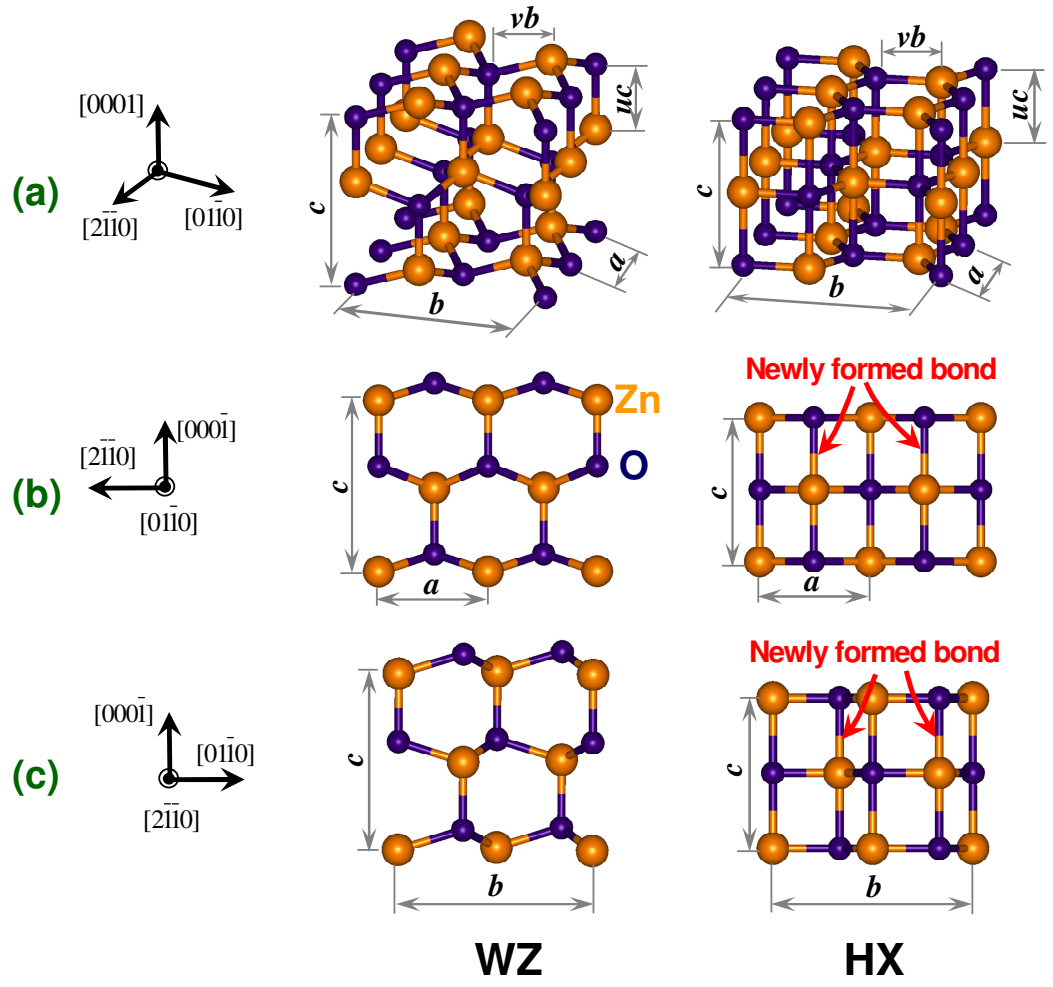

Figure 4.4 Illustrations of the WZ and HX structures involved in the phase transformation, (a) lattice structures of the WZ and HX phases, (b) atomic arrangement on $[01\bar{1}0]$ plane, and (c) atomic arrangement on $[2\bar{1}\bar{1}0]$ planes.

Table **4.1** lists the lattice constants for WZ, HX and RS structures. Note that the parameters for relaxed wires deviate slightly from the values for ideal bulk WZ due to surface effects (Kulkarni et al. 2005; Kulkarni and Zhou 2006b). For HX, $c = 4.35$ Å and $u = 0.50$ are similar to those for RS; whereas $a = 3.34$ Å and $v = 0.32$ are similar to those for WZ. Since *v* remains unchanged, HX has the same hexagonal symmetry around the *c*-axis as WZ. During the transformation, *u* changes from its initial value of 0.38 for WZ to a value of 0.5 for HX (Table 4.1), implying the flattening of the buckled wurtzite basal plane (Zn and O atoms becoming co-planar). Consequently, an additional Zn-O bond is formed along the [0001] axis [Figure 4.4(b) and Figure 4.4(c)]. As a result, Zn atoms are at equal distances from O atoms along the [0001] axis and the structure acquires the additional symmetry of a mirror plane perpendicular to the [0001] axis. This process occurs while the orientation of the basal plane remains invariant. The in-plane coordination of the HX structure is 3-fold and the full 3D coordination is 5-fold (as compared to the 4-fold in WZ).

The formation of additional bonds (therefore the increase in coordination) along the [0001] axis can also be seen in the charge density distributions on $\left(11\bar{2}0\right)$ planes in Figure 4.5. Obviously, an additional bond is formed between the O atom initially at the top left and the Zn atom initially at the bottom in the WZ structure. A similar unbuckled structure has been observed in GaN, MgO and ZnO thin films as a result of extensive surface reconstructions to suppress surface polarity (Capaz et al. 1995; Goniakowski et al. 2004; Claeyssens et al. 2005; Freeman et al. 2006). The newly discovered HX structure bears both resemblance to and distinction from the layered structure (LY) (Capaz et al. 1995; Goniakowski et al. 2004; Claeyssens et al. 2005; Freeman et al. 2006). The resemblance is in crystallography and the distinction is in coordination.

Specifically, a strong bond along the [0001] axis is seen in HX which occurs throughout solid wires. In contrast, this inter-planar bond is absent in LY which extends only a few layers from the surface beneath which the structure is predominantly WZ. Therefore, despite the similar geometric symmetries, HX has a higher coordination number (5) than LY (3). A similar HX phase has been reported as the natural state of boron nitride (*h*-BN) (Wentzcovitch et al. 1988). It has also been predicted as a metastable state of GaN during the WZ→RS transformation at high pressures (Limpijumnong and Lambrecht 2001a) and as a stable phase of MgO under hydrostatic tensile loading (Limpijumnong and Lambrecht 2001b).

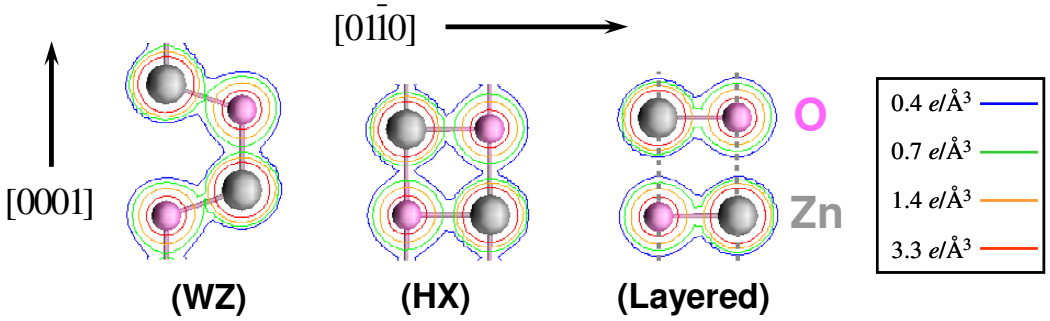

Figure 4.5 Charge density plots on the $(11\bar{2}0)$ planes of WZ, HX and the layered structure (LY).

Table 4.1 Lattice parameters for WZ, HX and RS under different loading conditions, select values are highlighted in boldface for easy comparison across different structures.

Parameters	WZ					HX			RS
	DFT $\sigma_b = 0$ GPa	AP[§] $\sigma_b = 0$ GPa	Exp[§§] $\sigma_b = 0$ GPa	DFT $\sigma_b = 10$ GPa	DFT $\sigma_c = -6$ GPa	AP[§] $\sigma_b = 10$ GPa	DFT $\sigma_b = 10$ GPa	DFT $\sigma_c = -6$ GPa	DFT $p = 8.22$ GPa
a (Å)	**3.20**	**3.22**	**3.25**	**3.12**	**3.28**	**3.34**	**3.29**	**3.49**	4.16
b (Å)	**5.54**	**5.66**	**5.63**	**5.93**	**5.68**	**6.24**	**6.42**	**6.03**	4.16
v	**0.33**	**0.32**	**0.33**	**0.33**	**0.34**	**0.32**	**0.32**	**0.33**	0.50
c (Å)	5.15	5.30	5.21	5.00	4.92	**4.35**	**4.18**	**4.18**	**4.16**
u	0.38	0.41	0.38	0.39	0.39	**0.50**	**0.50**	**0.50**	**0.50**
b/a	1.73	1.76	1.73	1.90	1.73	1.87	1.95	1.73	1.00
c/a	1.61	1.65	1.60	1.60	1.50	1.30	1.27	1.20	1.00

§ Analytical Potential, §§ Experiment (Binks 1994)

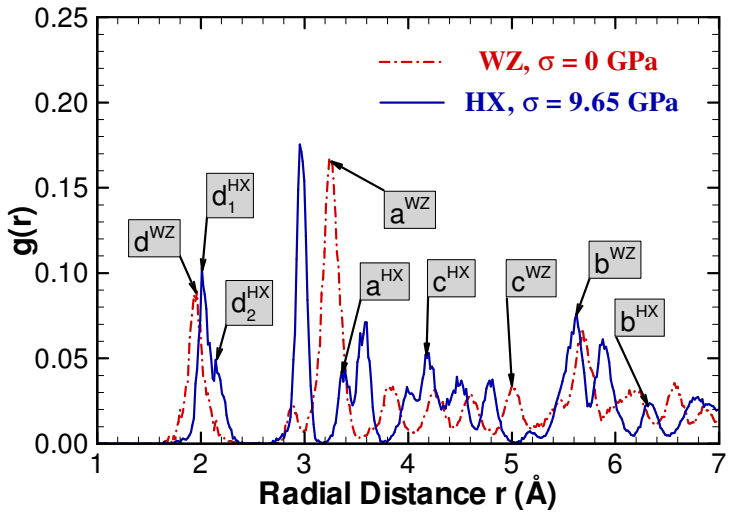

Figure 4.6 Radial distribution function profiles for a 21.22×18.95 Å nanowire before loading [point A in Figure 5.1(a)] and upon completion of phase transformation [point D in Figure 5.1(a)].

RDF profiles before loading is applied (point A, $\sigma = 0$ GPa) and upon completion of the WZ→HX transformation (point D, $\sigma = 8.58$ GPa) for the nanowire are shown in Figure 4.6. The profile for the initial wire (WZ structure) has its first peak at a radial distance of 1.93 Å, indicating a Zn-O bond distance consistent with the experimental value of 1.95 Å (Binks 1994). Upon completion of the WZ→HX transformation at point D, this peak has split into two peaks with the primary peak at 1.98 Å and the secondary peak at 2.20 Å. The primary peak corresponds to Zn-O bonds in the basal $\{0001\}$ plane of the HX structure, while the secondary peak is associated with the additional bonds formed along the [0001] axis (see Figure 4.4). Also seen in Figure 4.6 are peaks corresponding to lattice constants *a*, *b* and *c*. Initially in the WZ phase, the '*a*' peak is at 3.22 Å and the '*c*' peak is at 5.30 Å. The transformation to HX results in the shift of the '*a*' peak to 3.34 Å and the shift of the '*c*' peak to 4.35 Å. These shifts indicate that the transformation to the HX structure involves both an expansion of the basal planes (increase in '*a*') to accommodate the flattening of the buckled plane and a contraction in '*c*' which results in the formation of the Zn-O bond along the [0001] axis. The

transformation is also associated with a shift of the '*b*' peak from 5.66 Å for WZ to 6.24 Å for HX, consistent with the nature of the applied tensile loading. Further load increases are accompanied by increases in *b* with the associated RDF peak shifting toward a higher value (not shown).

4.1.4 Structural Stability

To identify stable crystalline structures under uniaxial tensile loading along the $[01\bar{1}0]$ direction, their enthalpy as a function of *c/a* and *b/a* for specific values of stress using DFT calculations is calculated. Since the transformation proceeds with the Zn and O basal planes becoming coplanar and a corresponding reduction in *c*, the stability of the HX phase under compression along the [0001] axis is also explored. Figure 4.7 shows the enthalpy surfaces (eV/unit cell) for *b*-oriented stress $\sigma_b = 7$, 10 and 13 GPa (with *c*-oriented stress $\sigma_c = 0$ GPa) and $\sigma_c = -6$ GPa (with $\sigma_b = 0$ GPa). Here, positive values of stress are considered tensile. In each case, there are two minima. For the tensile loading along $[01\bar{1}0]$ orientation, the first minimum ($^{b}H_{\min}^{WZ}$) is in the vicinity of *c/a* ≈ 1.6 and *b/a* ≈ 1.9; for the compressive loading along [0001], the first minimum ($^{c}H_{\min}^{WZ}$) is in the vicinity of *c/a* ≈ 1.5 and *b/a* = 1.732; each corresponding to a WZ structure with lattice parameters slightly different from those at zero stress (Table 4.1). The second minimum in each of these plots corresponds to the HX phase. For tensile loading, the second minimum ($^{b}H_{\min}^{HX}$) is in the vicinity of *c/a* ≈ 1.3 and *b/a* ≈ 1.9; for compressive loading, the second minimum ($^{c}H_{\min}^{HX}$) is in the vicinity of *c/a* ≈ 1.2 and *b/a* = 1.732. The structure at $^{b}H_{\min}^{HX}$ is that observed in the MD simulations discussed earlier. The difference in lattice parameters obtained from the two modes of loading stems from the fact that the ratio *b/a* is locked at 1.732 by structural symmetry under compression along the [0001] axis.

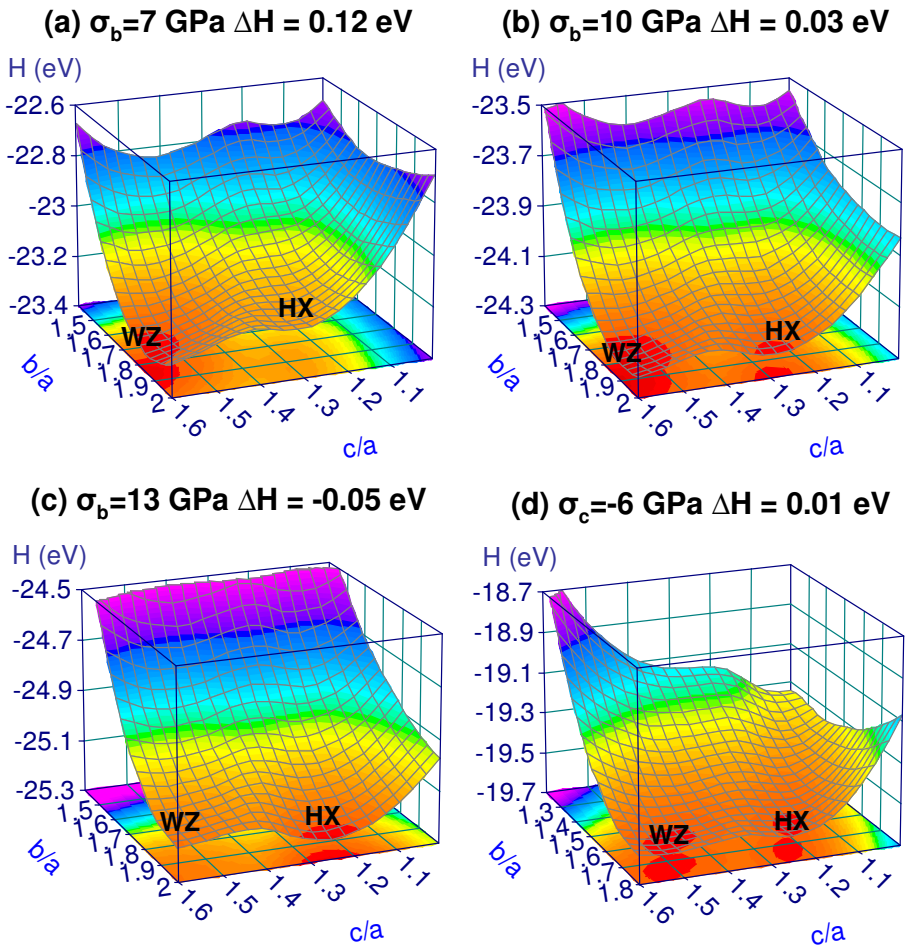

Figure 4.7 Enthalpy surface maps from DFT calculations for uniaxial tensile stress of (a) $\sigma_b = 7$ GPa, (b) $\sigma_b = 10$ GPa and (c) $\sigma_b = 13$ GPa along the *b* axis and uniaxial compressive stress of (d) $\sigma_c = -6$ GPa along the *c* axis.

At a tensile stress of 7 GPa [Figure 4.7(a)], ${}^{b}H_{\min}^{\mathrm{WZ}}$ is much lower than ${}^{b}H_{\min}^{\mathrm{HX}}$ ($\Delta H^{b} = {}^{b}H_{\min}^{\mathrm{HX}} - {}^{b}H_{\min}^{\mathrm{WZ}} = 0.12$ eV), hence, no transformation takes place. As the stress is increased to 10 GPa, ${}^{b}H_{\min}^{\mathrm{HX}}$ and ${}^{b}H_{\min}^{\mathrm{WZ}}$ become comparable ($\Delta H^{b} = 0.03$ eV) and consequently both WZ and HX are equally favored. At an applied stress of 13 GPa [Figure 4.7(c)], ${}^{b}H_{\min}^{\mathrm{HX}}$ is lower than ${}^{b}H_{\min}^{\mathrm{WZ}}$ ($\Delta H^{b} = -0.05$ eV), indicating that HX is more stable. The transformation barrier between the two phases of 0.06 eV is quite low, compared with the barrier of ~0.15 eV for the high pressure WZ→RS transformation

(Limpijumnong and Jungthawan 2004). A similar behavior is observed under uniaxial compression along the [0001] direction. The WZ and HX enthalpy wells are comparable at $\sigma_c = -6$ GPa [$\Delta H^c = 0.01$eV, Figure 4.7(d)]. At higher compressive stresses, ${}^cH_{\min}^{\mathrm{HX}}$ is lower than ${}^cH_{\min}^{\mathrm{WZ}}$, indicating the relative favorability of HX under such conditions. As the magnitude of either σ_c or σ_b is increased above the corresponding equilibrium transition value, HX becomes more stable and the transformation barrier becomes even lower, resulting in an even higher driving force for transformation. In summary, the distinct minima in the vicinities of the HX and WZ structures on the enthalpy maps obtained through DFT calculations confirm what is discovered in MD calculations by pointing out that (1) HX is energetically favored over WZ above a critical applied tensile stress value of $\sigma_b \approx 10$ GPa along the $[01\bar{1}0]$ direction or a critical compressive stress value of $\sigma_c \approx -6$ GPa along the [0001] direction and (2) the barrier for the transformation decreases as applied stress increases.

4.2 Wurtzite to Body-Centered-Tetragonal Phase Transformation

4.2.1 Tensile Response of [0001] Nanorods

Figure 4.8 shows the stress-strain response of a nanorod with lateral dimension *d* = 32.5 Å. Four distinct stages are observed. The first stage (A→B) corresponds to the elastic stretching of the WZ structure up to a strain of 7.5%. Further deformation results in a precipitous stress drop (B→C) associated with the WZ to BCT-4 phase transformation. The transformation completes at a strain of 8.5%. Continued loading causes elastic stretching of the BCT-4 structure (C→D) and culminates in the eventual failure at a strain of 16.9% (point E). To analyze the stability of the parent and transformed structures, unloading is performed from states prior to transformation initiation (first peak tensile stress, FPTS, point B) and failure initiation of the nanorod

(second peak tensile stress, SPTS, point D). The unloading path from B coincides with the loading path, confirming that the deformation from A to B is indeed the elastic response of the WZ-structured nanorod. Unloading from D also results in the elastic recovery of the BCT-4 structure and continued unloading beyond the transformation completion strain (point C) does not result in a reverse transformation. Instead, the nanorod retains the BCT-4 structure when the stress is reduced to zero (F in Figure 4.8).

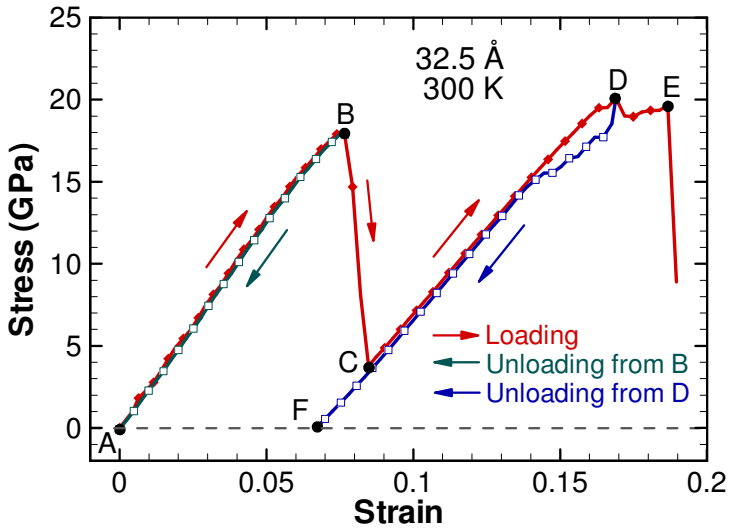

Figure 4.8 Stress-strain curve of [0001] nanorod with d = 32.5 Å at 300 K during loading and unloading (Wang et al. 2007).

4.2.2 Transformation Mechanism

The WZ to BCT-4 transformation occurs through a combination of (1) the breaking of every other Zn-O bonds along the [0001] direction [bond A in Figure 4.9(a)] and (2) the formation of an equal number of Zn-O bonds along the same direction [bond B in Figure 4.9(a)] next to the broken bonds. This process repeats on alternate planes along the $[01\bar{1}0]$ direction. The transformed structure retains the tetrahedral coordination with each Zn/O atom at the center and four O/Zn atoms are at the vertices of a tetrahedron. The geometry of the tetrahedron can be characterized through the O-Zn-O bond angles (α_i, $i = 1..6$), as shown in Figure 4.9(a). For WZ, all bond angles are

approximately equal ($\alpha_i \approx 108^\circ$). For BCT-4, the formation of 4-atom rings results in three distinct bond angles ($\alpha_1 \approx 90^\circ$, $\alpha_2 \approx 112.7^\circ$ and $\alpha_3 \approx 113.7^\circ$).

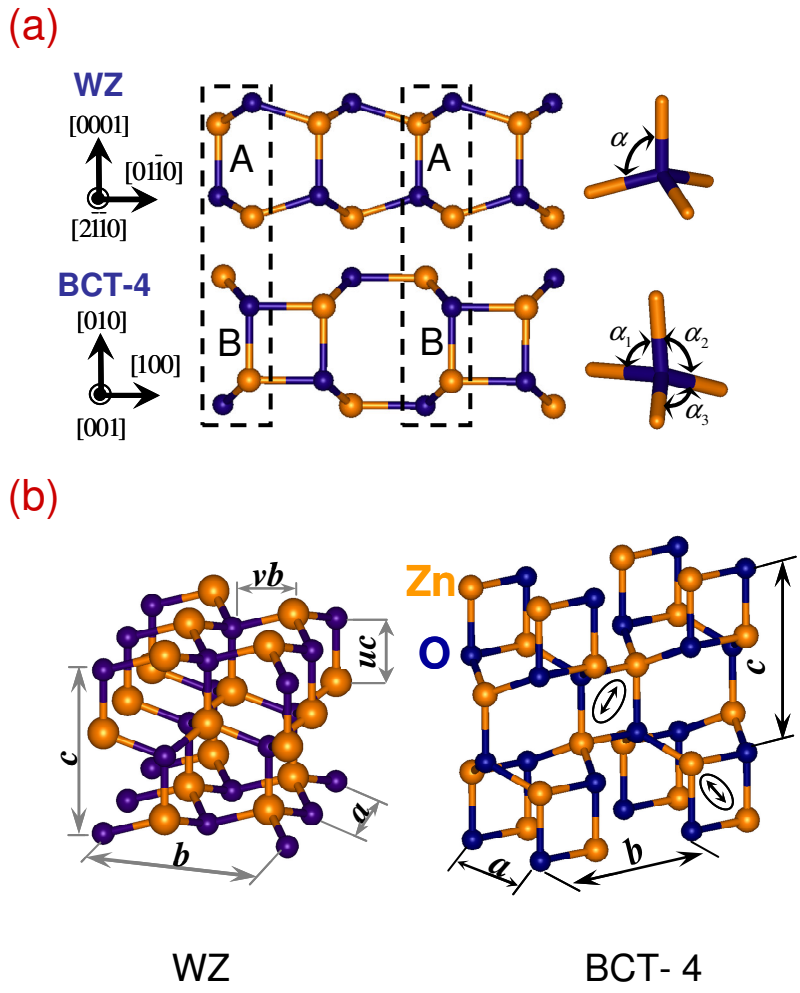

Figure 4.9 (a) Wurtzite (WZ) and newly discovered body-centered tetragonal with four atom rings (BCT-4) structures and (b) crystallographic transition through breaking and formation of bonds and differences in bond angles between the WZ and the BCT-4 structures.

As seen from Figure 4.9(b), the transformed phase consists of 4-atom (2 Zn and 2 O) rings arranged in a BCT lattice. Note that, the 4-atom ring at the center is rotated by 90º relative to the rings at the corners of the tetragonal lattice cell. Strictly speaking, the unit cell consists of two-ring clusters (one of each orientation, total of 8 atoms) positioned in a simple tetragonal primitive lattice. Figure 4.9(b) also shows the lattice

parameters *a*, *b* and *c* for the WZ and BCT-4 structures. Their respective values as obtained from MD and DFT calculations (in square brackets) at various stress levels are listed in Table 4.2 along with unit cell volumes. For WZ, the ratios *c/a* and *b/a* are 1.60 and 1.73, respectively. Throughout the transformation, the *b/a* ratio remains at its initial value of 1.73 (±0.02), reflecting the symmetries of the loading and the lattice. On the other hand, upon transformation to BCT-4 at a stress above 7 GPa, the *c/a* ratio increases to 1.8. Phenomenologically, the predilection for the BCT-4 phase over the WZ phase under the tensile loading conditions considered here can be explicated by its elongated configuration in the [0001] direction (higher *c/a* ratio) relative to that of the WZ structure. Upon unloading, the residual strain at F in Figure 4.8 is 6.8% according to both MD and DFT. It reflects the dimensional difference between the unstressed WZ and BCT-4 structures in the [0001] direction in Figure 4.9(a). This unstressed BCT-4 structure corresponds to the "ideal" BCT-4 structure predicted by the DFT calculations with *b/a* = *c/a* = 1.73.

Table 4.2 Lattice constants for WZ and BCT-4 ZnO in tension along the c-axis obtained via MD and DFT [square brackets] calculations.

Parameters	WZ	BCT-4			
	$\sigma = 0$	$\sigma = 0$	$\sigma = 4$	$\sigma = 7$	$\sigma = 10$
a (Å)	3.29 [3.20]	3.24 [3.17]	3.22 [3.13]	3.20 [3.09]	3.19 [3.06]
b (Å)	5.67 [5.55]	5.58 [5.48]	5.54 [5.42]	5.51 [5.35]	5.48 [5.32]
c (Å)	5.17 [5.13]	5.52 [5.48]	5.67 [5.71]	5.77 [5.87]	5.84 [5.98]
V=abc(Å^3)	96.4 [91.1]	99.8 [95.2]	101.2 [96.9]	101.7 [97.0]	102.1 [97.3]
ΔV(Å^3)	0.0 [0.0]	3.4 [4.1]	4.8 [5.8]	5.3 [5.9]	5.7 [6.2]
c/a	1.57 [1.60]	1.71 [1.73]	1.76 [1.82]	1.80 [1.9]	1.83 [1.95]
b/a	1.72 [1.73]	1.72 [1.73]	1.72 [1.73]	1.72 [1.73]	1.71 [1.73]

The BCT-4 structure is analyzed using the radial distribution function (RDF). Figure 4.10 shows the RDF profiles for the WZ structured rod after initial relaxation (corresponding to point A in Figure 4.8) and the BCT-4 structured rod upon transformation completion (corresponding to point C in Figure 4.8). For both structures, the first peak occurs approximately at 1.98 Å which corresponds to the Zn-O bond distance. Similarly, the second peaks for the two structures (corresponding to lattice constant *a*) coincide, indicating that the two structures have the same lattice parameter along the initial $[2\bar{1}\bar{1}0]$ orientation. Additionally, the '*b*' peaks for the WZ and BCT-4 structures also coincide, suggesting that the *b/a* ratio remains constant during the transformation. However, the profiles (and hence the structures) are different from the third peaks onward. The '*c*' peak for WZ at 5.20 Å shifts to 5.63 Å for BCT-4, causing the *c/a* ratio to increase from 1.60 to 1.73. This change in *c* is consistent with the applied loading and the strain associated with the transformation into BCT-4.

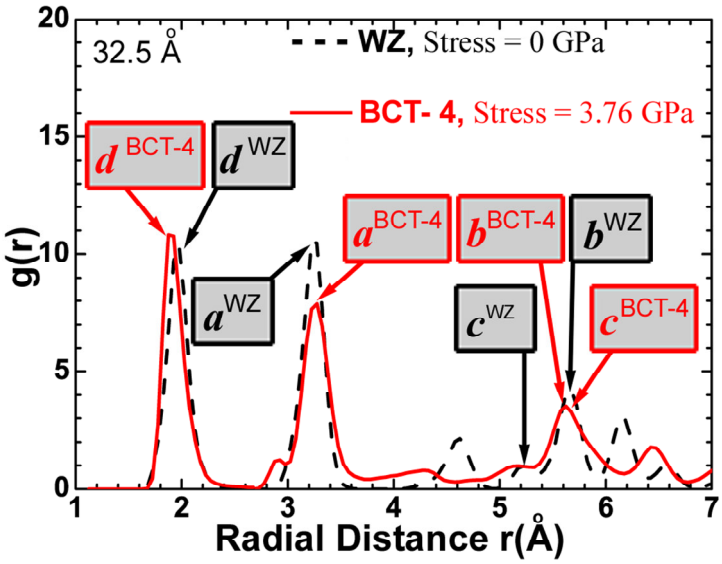

Figure 4.10 Radial distribution function (RDF) profiles for a 32.5 Å WZ-structured nanorod before loading (point A in Figure 4.8, dash line) and upon completion of structure transformation to BCT-4 (point C in Figure 4.8, solid line).

4.2.3 Energetic Favorability

The relative favorability of the two phases is studied by calculating the enthalpy (per 4 Zn-O pairs) using DFT calculations (Limpijumnong and Jungthawan 2004; Kulkarni et al. 2006). The complete enthalpy surfaces show that the BCT-4 structure has minimum enthalpy at *b/a* = 1.73 for all values of tensile stress considered. For clarity without loss of generality, the discussions here use Figure 4.11 which shows the enthalpy values (eV per 4 Zn-O pairs) for both structures for b/a = 1.73 at σ = 0, 4, 7 and 10 GPa.

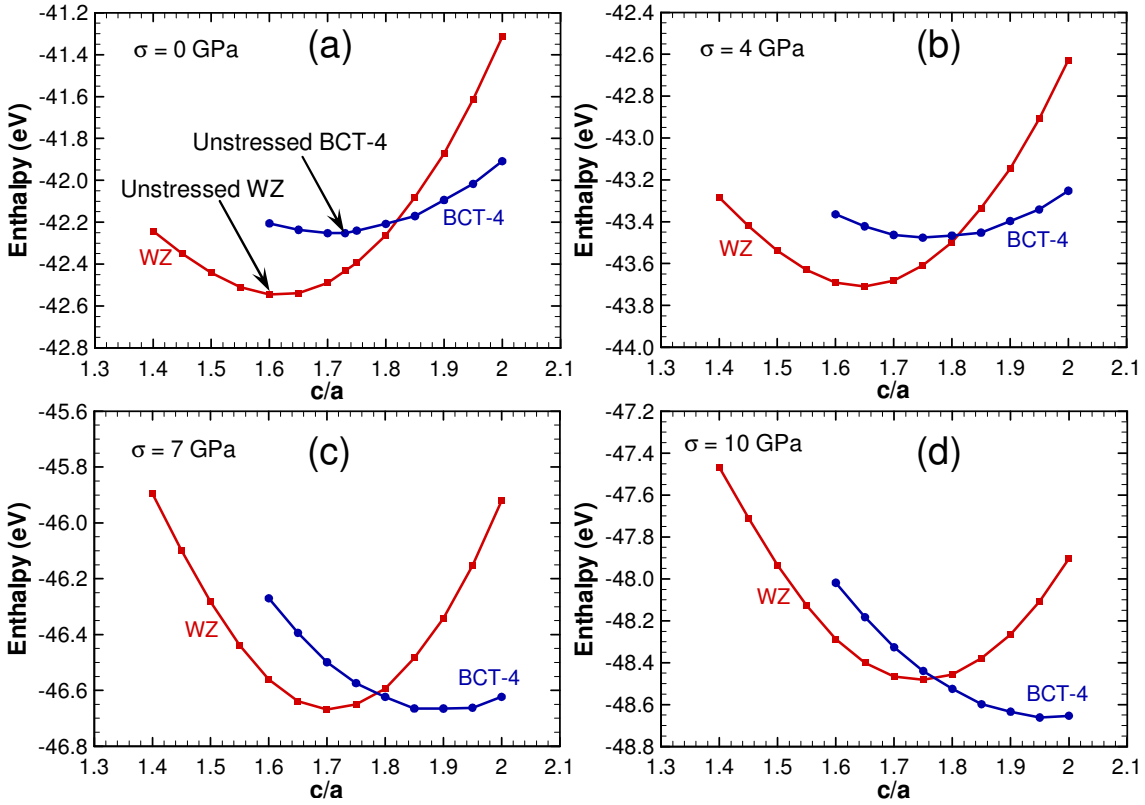

Figure 4.11 Enthalpy (per 4 Zn-O pairs) as a function of *c/a* obtained from DFT calculations for *b/a* = 1.73 at tensile stresses of (a) $\sigma = 0$ GPa, (b) $\sigma = 4$ GPa, (c) $\sigma = 7$ GPa and (d) $\sigma = 10$ GPa in the [0001] direction.

At any stress level, each structure has its own enthalpy minimum. The first minimum is in the vicinity of c/a ≈ 1.6 which corresponds to WZ with lattice parameters slightly different from those at zero stress and the second minimum is in the vicinity of

c/a ≈ 1.7-1.9 which corresponds to BCT-4. At zero stress, WZ is the stable crystal structure and its enthalpy is lower than that of BCT-4 by 0.3 eV [Figure 4.11(a)]. As the stress is increased to 4 GPa [Figure 4.11(b)], the difference in enthalpies decreases and at a stress of 7 GPa [Figure 4.11(c)], the two minima become comparable indicating that WZ and BCT-4 are equally favored. This value of stress corresponds to the equilibrium transition stress for the two phases. Since an energy barrier (associated with intermediate transitional states) exists for the transformation, a stress level higher than the 7 GPa equilibrium stress is required to initiate the transformation. At a stress of 10 GPa [Figure 4.11(d)], the enthalpy of BCT-4 is lower and this structure is clearly favored. Further increases in stress result in the eventual initiation of the phase transformation. The specific stress level at which the transformation initiates depends on the rod size and temperature. For the particular nanorod in Figure 4.8 at 300 K, the critical stress level is $\sigma = 17.9$ GPa. The gradual evolution of the local enthalpy minimum for the BCT-4 at $\sigma = 0$ into a global minimum as stress increases confirms that the phase transformation observed in MD simulations is indeed energetically favored.

4.2.5 Size and Temperature Effects

The effect of lateral size on the response of the nanowires is also analyzed. Figure 4.12(a) shows the stress-strain curves for nanorods of different sizes. The critical stress required for the nucleation of the transformation (FPTS) decreases by 25% from 21.90 to 16.50 GPa as the size increases from 19.5 to 45.5 Å [Figure 4.12(b)]. The failure stress (SPTS) is also size-dependent, decreasing 33% from 27.02 to 18.05 GPa over the same range of wire size. Detailed results are listed in Table 4.3.

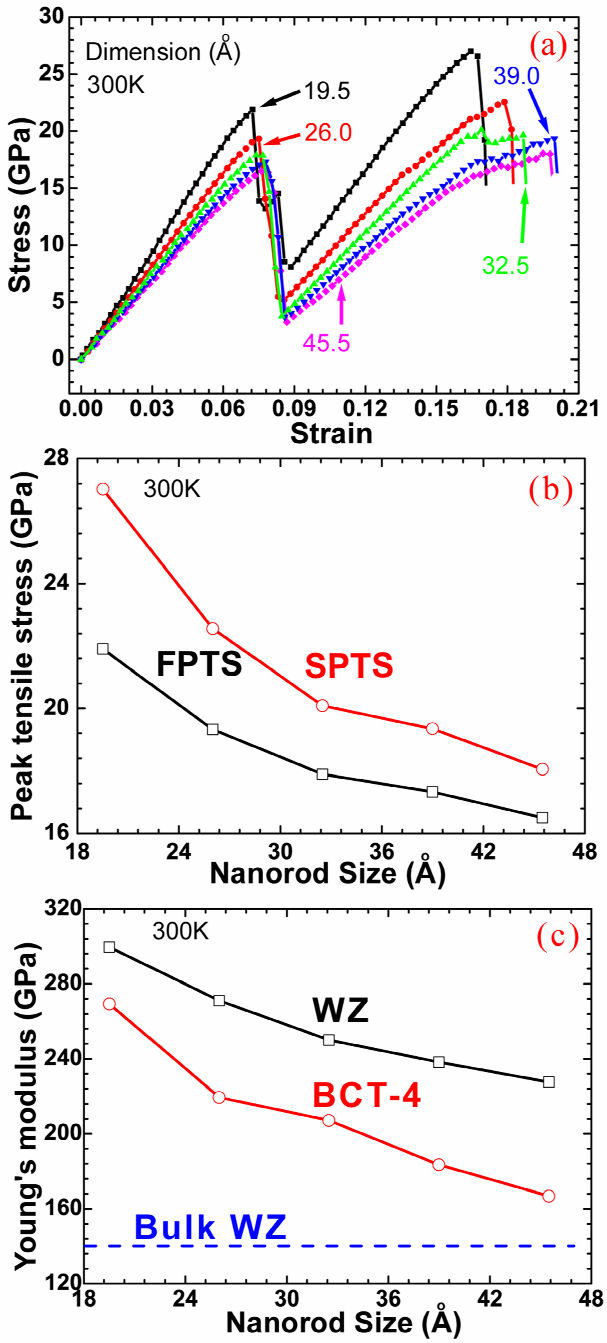

Figure 4.12 Size dependence of elastic responses, (a) Stress-strain relations, (b) critical stress for transformation nucleation (FPTS) and failure strength (SPTS) and (c) elastic moduli of WZ and BCT-4.

The elastic moduli of the nanorods (both WZ structured and BCT-4 structured) are higher than the corresponding value of 140 GPa (Kong and Wang 2003; Chen et al. 2006b) for bulk WZ and decrease as the size increases, as shown in Figure 4.12(c). The

modulus of WZ structured rods decreases by 24% from 299.49 to 227.51 GPa as the lateral dimension is increased from 19.5 to 45.5 Å. On the other hand, the modulus of the BCT-4 structured rods decreases by 38% from 269.29 to 166.86 GPa over the same size range. The size dependence observed here can be explained by considering the state of stress in the nanorods. The high surface-to-volume ratios of the nanorods and the tensile surface stress induce significant compressive stresses in the cores of rods. It has been shown that surface-stress-induced internal (compressive) stresses are inversely proportional to the lateral dimensions of nanostructures (Diao et al. 2003; Sander 2003; Gall et al. 2004; Liang and Zhou 2005; Kulkarni and Zhou 2006b), effectively causing the size effect observed here. When cross-sectional dimensions are sufficiently large, surface-stress-induced compressive stresses are small and the surface effects are inconsequential. As a result, the material behavior approaches that of its bulk counterpart.

Table 4.3 Critical stress for nucleation (FPTS), maximum tensile strength (SPTS), critical strains and elastic moduli of the nanorods at 300 K.

Size (Å)	**19.5**	**26.0**	**32.5**	**39.0**	**45.5**
FPTS (GPa)	21.90	19.33	17.89	17.33	16.50
Strain at FPTS (%)	7.24	7.50	7.40	7.78	7.61
SPTS (GPa)	27.02	22.55	20.09	19.35	18.05
Strain at SPTS (%)	16.44	17.88	16.90	19.99	19.50
Elastic Modulus of WZ (GPa)	299.49	271.05	250.02	238.19	227.51
Elastic modulus of BCT-4 (GPa)	269.29	219.50	207.14	183.43	166.86
Residual strain (%)	6.06	6.30	6.67	6.56	6.65

Temperature also has a significant effect on the critical stress required for transformation initiation and on the elastic responses of the WZ and BCT-4 structured rods. Figure 4.13(a) shows the stress-strain curves associated for a 32.5 Å nanorod at 300, 600, 900, 1200 and 1500 K. The two linear elastic stages of deformation and the stress drop associated with the transformation are clear at all temperatures. A significant

dependence of FPTS on temperature is observed. Specifically, as the temperature increases from 300 to 1500 K, the FPTS decreases 87.8% from 17.89 to 2.19 GPa, as shown in Table 4.4 and Figure 4.13(b). This decrease in transformation initiation stress is due to the enhanced ability of the nanorod to overcome the energy barrier at higher temperatures. At temperatures above 600 K, a transitional stage of linear response is observed. This stage of deformation corresponds to the stretching of a composite WZ+BCT-4 structure. The primary reason for the intermediate stage is that, at higher temperatures, the FPTS is lower and the strain energy stored in the WZ structured rod is not sufficient to drive the WZ→BCT-4 transformation for the whole rod. Instead, further stretching is required for the transformation to complete. Note that the deformation analyzed here is strain-controlled. At temperatures above 900 K, the FPTS is low enough such that there simply is not enough elongation of the rod at the initiation of the phase transformation (e.g., 1.98% and 1.21% for 1200 and 1500 K, respectively) to accommodate the dimensional increase associated with the WZ→BCT-4 transformation (approximately 6.8% for a 32.5 Å rod, see point F of Figure 4.8). As a result, compressive stresses develop in the rods at such temperatures.

The enhanced mobility of atoms at higher temperatures promotes the formation of defects and causes significant thermal softening. As a result, a significant temperature dependence of the responses of the WZ and BCT-4 structures is also observed. Specifically, for 32.5 Å rod the elastic moduli of the WZ and BCT-4 structures decrease 18% and 16%, respectively, as temperature is increased from 300 to 1500 K [Figure 4.13(c)]. Over the same temperature range, the SPTS and the maximum elongation decrease by 40% and 8.17%, respectively, as shown in Figure 4.13.

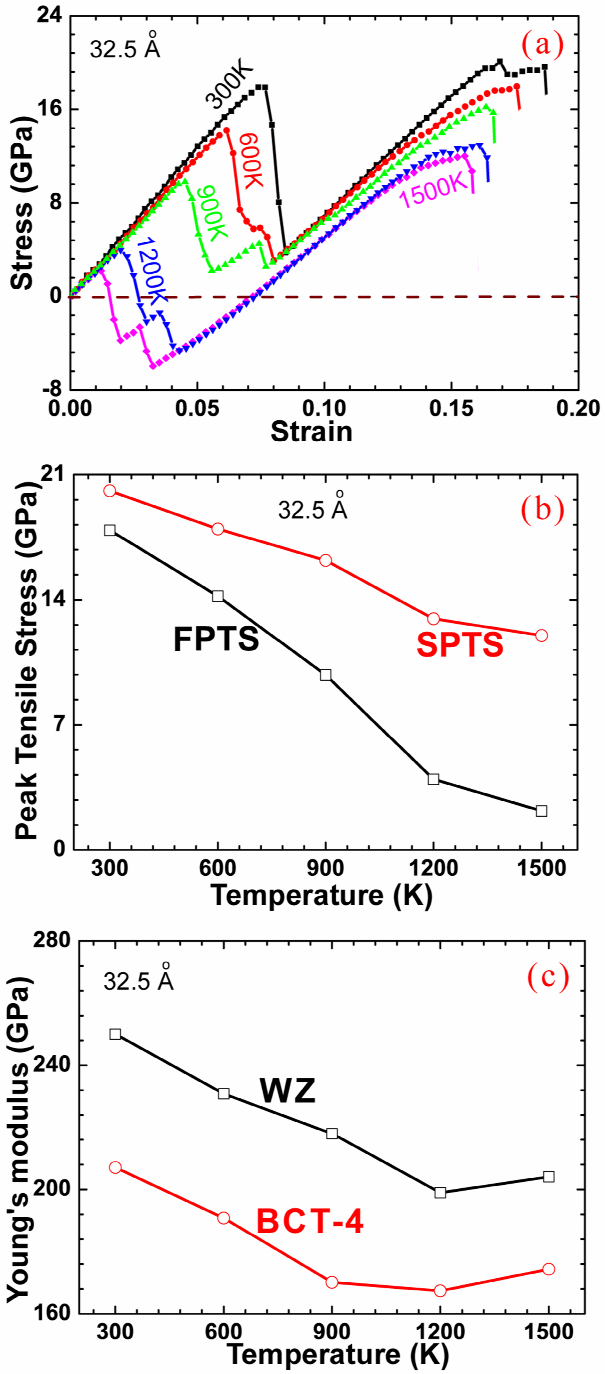

Figure 4.13 Temperature dependence of response, (a) Stress-strain relations, (b) critical stress for transformation nucleation (FPTS) and failure strength (SPTS) and (c) elastic moduli of WZ and BCT-4.

Table 4.4 Critical stress for nucleation (FPTS), maximum tensile strength (SPTS), critical strains and elastic moduli of a 32.5 Å nanorod at different temperatures.

Temperature (K)	**300**	**600**	**900**	**1200**	**1500**
FPTS (GPa)	17.89	14.20	9.79	3.96	2.19
Strain at FPTS (%)	7.40	6.14	4.52	1.98	1.21
SPTS (GPa)	20.09	17.97	16.20	12.94	12.00
Strain at SPTS (%)	16.90	17.57	16.36	16.11	15.52
Elastic Modulus of WZ (GPa)	250.02	230.84	217.98	198.95	204.09
Elastic Modulus of BCT-4 (GPa)	207.14	190.79	170.11	167.34	174.33

4.2.6 Transformation Assisted Property Variations

The WZ-to-BCT-4 phase transformation observed here alters the electrical, thermal and mechanical responses of the nanorods. Recently, [0001]-oriented ZnO nanorods with a WZ structure have been used to successfully generate direct electric current through mechanical bending (Zhao et al. 2004). The transformation from the piezoelectric WZ structure to the non-piezoelectric BCT-4 structure establishes an upper bound for the maximum possible current generation and operational strain for this application. Specifically, the electric field output E_3 can be related to the longitudinal strain ε_3 through $E_3 = \varepsilon_3 / d_{33}$ where $d_{33} \approx 20.5$ pm/V is the piezoelectric coefficient for the ZnO nanorods. Since the strain at the initiation of transformation [B in Figure 4.8] is approximately 7.5% for all rod sizes, the maximum electric field output is therefore 3.7 V/nm. The mechanical response of BCT-4 also differs significantly from that of WZ. In particular, the enthalpy curves for BCT-4 are flatter than those for WZ (Figure 4.11), indicating that the elastic stiffness of BCT-4 is lower than that for WZ. Indeed, in Figure 4.8 the slope of curve AB (228 GPa which is [0001] elastic modulus of WZ) is higher than that of curve FD (167 GPa which is the corresponding modulus of BCT-4). The thermal response of semiconductors such as ZnO is dominated by phonons and the interactions between phonons and surfaces (Kulkarni and Zhou 2006a). The WZ to BCT-

4 phase transformation changes the atomic arrangement and hence the phonon spectrum, resulting in potentially large changes in thermal conductivity. The electronic band structures of WZ and BCT-4 are shown in Figure 4.14. Note that the total number of bands for BCT-4 is twice that for WZ because the unit cell of BCT-4 has twice as many atoms as WZ. Both phases have direct band gaps at Γ. Although DFT calculations with local density approximations are known to underestimate band gaps and therefore are not normally used to predict absolute band gap values, they can provide valid relative comparisons between the two phases. The calculated band gap and average electron effective mass of BCT-4 are, respectively, 12% and 17% smaller than those of WZ, giving the nanorod a smaller bandgap and potentially higher electron mobility after the WZ-to-BCT-4 transformation. These mechanically induced electrical property shifts may have novel applications in devices that depend on coupling between responses.

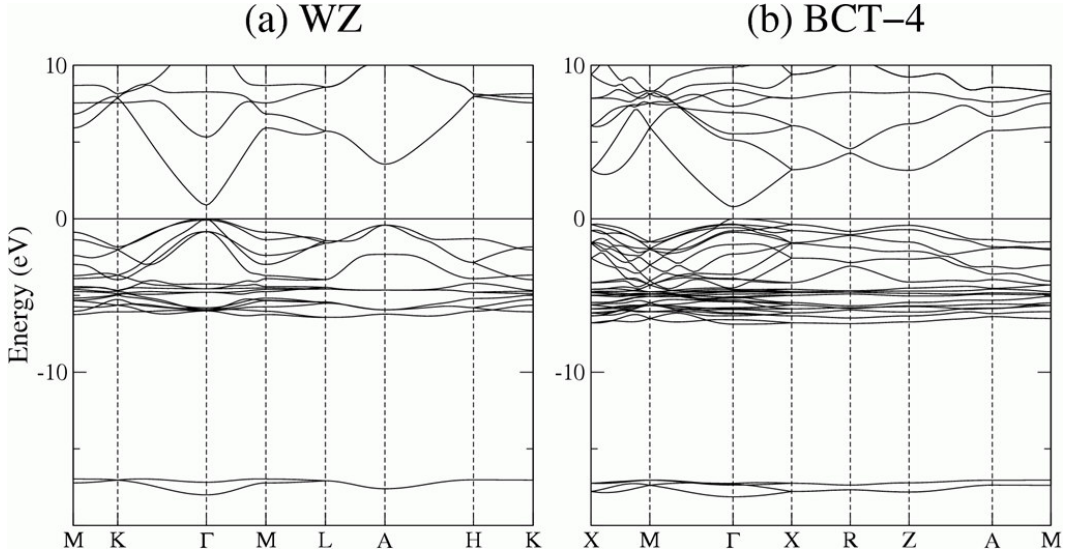

Figure 4.14 Band structures of (a) WZ ZnO and (b) BCT-4 ZnO obtained by DFT calculations. The energy is relative to the top of the valence bands.

4.9 Chapter Summary and Insights

The discovery of two novel phase transformations observed in the tensile loading of nanowires and nanorods is reported. Each transformation results in a previously-

unknown crystal structure for ZnO. Uniaxial loading of $[01\bar{1}0]$-oriented ZnO nanowires results in the transformation of the parent wurtzite (WZ) structure to a graphite-like phase (HX). Crystallographically, this newly discovered polymorph of ZnO has a five-fold coordination, in contrast to the four-fold coordination of the initial WZ structure, implying that the transformation proceeds towards higher ionicity. The transformation results in a pseudoelastic behavior with recoverable strains up to 16%.

Wurtzite to a body-centered-tetragonal structure with four-atom rings (BCT-4) is observed in hexagonal ZnO nanorods with the [0001] growth direction. As a result of this transformation, the response of the nanorods to uniaxial tensile loading manifests in three stages, including (i) the elastic stretching of the WZ structure, (ii) a structural transformation from WZ to BCT-4 and (iii) the stretching of the BCT-4 structure. A significant dependence of deformation on rod size is observed. As the lateral dimension is increased from 19.5 to 45.5 Å, the elastic modulus values of the WZ and BCT-4 structured rods decrease by 24% and 38%, respectively, and the critical stress for transformation initiation decreases by 25%. The behavior of the nanorods is also temperature-dependent, with the elastic moduli of the WZ and BCT-4 structures decreasing 18% and 16%, respectively, as temperature increases from 300 to 1500 K. The critical stress for transformation initiation shows the most pronounced temperature dependence, decreasing 87.8% over the same temperature range.

Most importantly, the identification of the BCT-4 and HX structures leads to a more complete understanding of the nature and extent of polymorphism in ZnO and its dependence on load triaxiality. Joining Wurtzite (WZ), Zinc Blende (ZB), Rocksalt (RS), HX and BCT-4 constitute the fourth and fifth polymorphs of ZnO discovered so far. It is now possible to construct a structure-load triaxiality map for ZnO, as shown in Figure 4.15. Among the previously well known phases, WZ is the most stable and naturally occurring phase and RS is observed under hydrostatic compressive conditions (Kulkarni et al. 2007b). Both BCT-4 and HX are stabilized under uniaxial loading, with HX

occurring under tension along the $[01\bar{1}0]$ and/or $[2\bar{1}\bar{1}0]$ directions as well as compression along the $[0001]$ direction and BCT-4 occurring under tension along the $[0001]$ direction. It is worthwhile to note that ZB grows epitaxially on specific surfaces of cubic crystals and can not be obtained via a transformation from WZ under external loading, therefore, it is not included in this map.

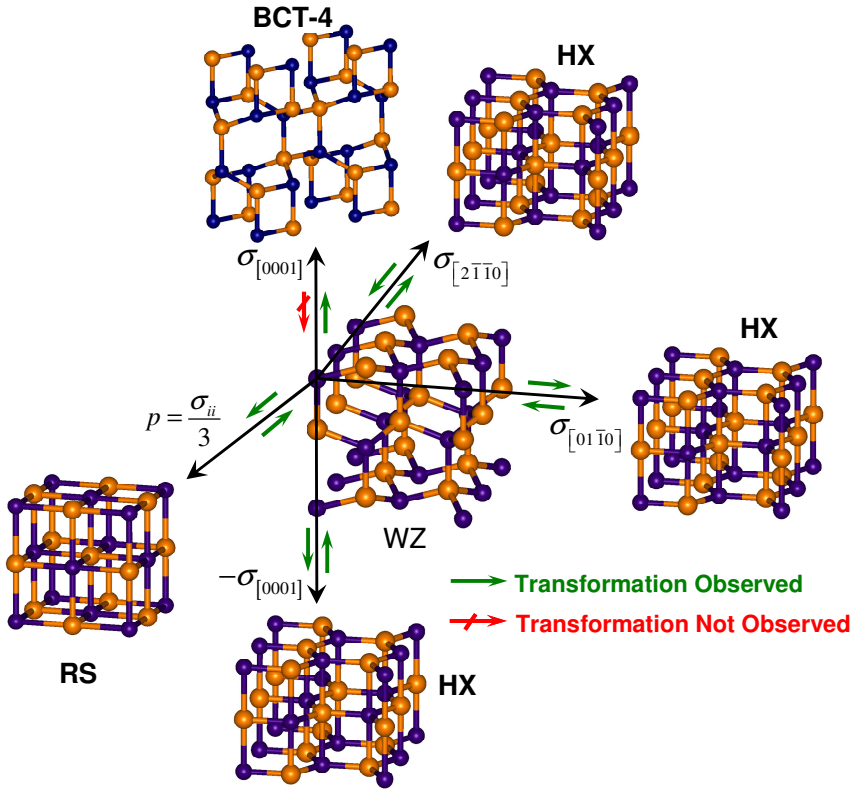

Figure 4.15 Crystalline structure-load triaxiality map summarizing the nature and much wider extent of polymorphism in ZnO than previously known; WZ is the natural state at ambient conditions, RS occurs under hydrostatic or near hydrostatic compression, HX occurs under tension along the $[2\bar{1}\bar{1}0]$ and $[01\bar{1}0]$ directions as well as compression along the $[0001]$ direction, and the newly identified BCT-4 occurs under tension along the $[0001]$ direction. The green and red allows indicate, respectively, possible and impossible transformation paths under relevant load direction reversals. ZB cannot be obtained via a transformation from WZ under external loading and is not included in this map.

CHAPTER 5 : PSEUDOELASTICITY

Pseudoelasticity and shape memory effect (SME) are normally observed in shape memory alloys and elastomers (Otsuka and Wayman 1998). Such effects have recently been discovered in single crystalline metal nanowires (Liang and Zhou 2005; Liang et al. 2005b; Park et al. 2005; Liang and Zhou 2006). In the previous chapter, we have seen that a novel pseudoelastic behavior is observed in $[01\bar{1}0]$-oriented ZnO nanowires which arises from a reversible phase transformation from WZ phase to the newly discovered HX phase (Kulkarni et al. 2006). This previously unknown five-fold coordinated polymorph of ZnO can result from either tensile loading along the $[01\bar{1}0]$ direction or compressive loading along the [0001] direction. For $[01\bar{1}0]$ nanowires in tension, recoverable strains, which comprise of the elastic stretching of the WZ and HX phases and a contribution from the transformation, can be up to 16%. While the ability to undergo a phase transformation is the primary reason for the unusual pseudoelastic behavior, the nearly defect-free nature of these nanowires and the large surface-to-volume ratios, which enhance atomic mobility, also contribute to the wires' ability to undergo deformation without fracture. The high strengths, large recoverable strains and property variations associated with transformation make these nanowires ideal candidates as nanocomponents in NEMS. However, a fundamental understanding of the constitutive behavior, the nature of the phase transformation and the characteristics of the transformed phase is needed in order to unleash the potential of these nanowires.

This chapter focuses on characterizing the pseudoelastic response of the $[01\bar{1}0]$ ZnO nanowires with lateral dimensions of 21.22×18.95, 31.02×29.42 and 40.81×39.89 Å under quasi-static tensile loading. The characterization accounts for temperatures between 100 and 700 K. The analysis focuses on the formation of the new HX crystalline structure and the transformation path from WZ to HX under uniaxial tensile loading. In

particular, the atomic motions or lattice distortion resulting in the formation of the HX structure are quantified through the gradient of a continuum deformation map. The analysis lends itself to the quantification of the recoverable strains associated with the pseudoelastic behavior of the nanowires, including contributions from the elastic stretching of the WZ and the HX phases and lattice size change due to the phase transformation. The size- and temperature-dependence of important parameters including the critical stress for the initiation of phase transformation, maximum recoverable strain, and hysteretic dissipation are also quantified.

Secondly, a micromechanical continuum model is developed to characterize the observed pseudoelastic behavior. The emphasis is on capturing the major characteristics of and accounting for the size and temperature effects embedded in the overall constitutive behavior. The model considers the elastic deformation of the pure phases and the WZ→HX transformation during loading and the HX→WZ transformation during unloading. The transformation is decomposed into a reversible process of structural transitions between WZ and HX through a sequence of phase equilibrium states (PES) and a dissipative process of interface propagation. The equilibrium transition process is modeled using the framework of strain energy functions with multiple local minima (Abeyratne and Knowles 1993; Abeyratne and Kim 1994; Abeyratne and Bhattacharya 2001). The dissipative nature of the interface propagation process is related to the ruggedness of the energy landscape associated with (1) the elastic energy storage during the stretching of the heterogeneous nanowire structure and (2) the energy release associated with interface formation and motion.

5.1 Pseudoelastic Response

Figure 5.1 (a) shows the tensile stress strain curve of a 40.81×39.89 Å wire during loading and unloading at 100 K. The configurations of this wire at four different stages (three of which are during loading) of deformation along the curve are shown in Figure

5.1(b), with the atoms colored by their coordination numbers. In the wurtzite structure [initial configuration, (i) in Figure 5.1(b)], each atom has a coordination number of 4, typical for tetrahedral structures. Atoms on surfaces and edges have coordination numbers of 3 or less. In the HX phase [(ii) and (iii) in Figure 5.1(b)], on the other hand, each atom has a coordination number of 5 due to the additional Zn-O bond along the [0001] axis as compared to the WZ phase.

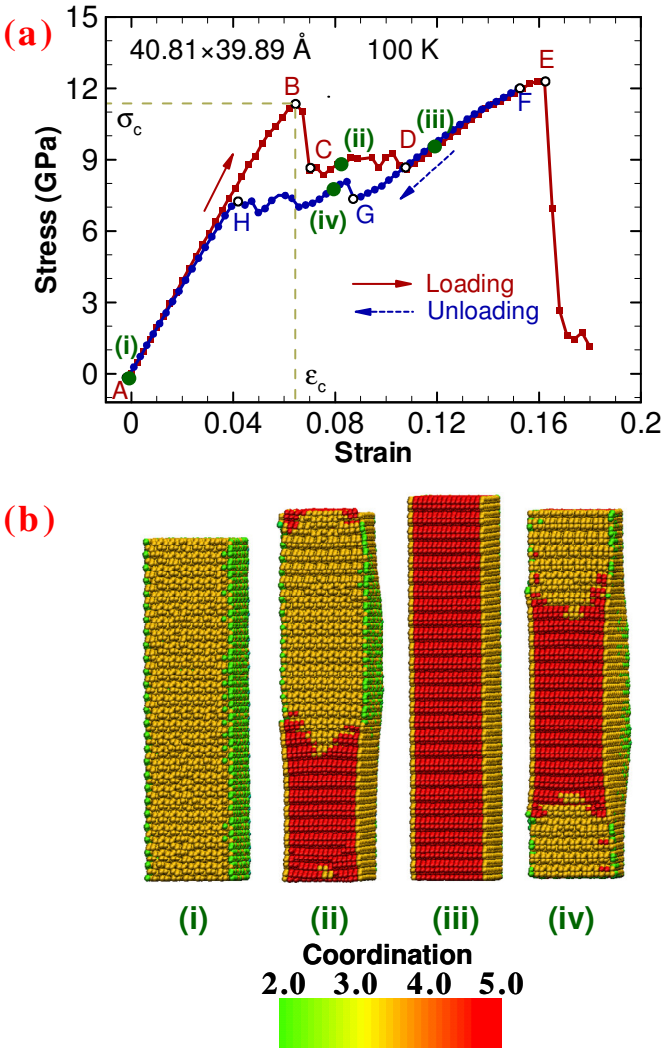

Figure 5.1 Tensile behavior of a 40.81×39.89 Å nanowire, (a) stress-strain curve under loading and unloading; (b) deformed configurations at different stages of loading and unloading.

The loading response [Figure 5.1(a)] consists of initial elastic stretching of the WZ wire (A→B), structural transformation from WZ to HX (B→D) and elastic stretching of the HX wire (D→E), culminating in the eventual failure at E. The stress-strain relation in the elastic regime between A and B is essentially linear. Deformation beyond the elastic regime results in a stress drop from 11.31 to 10.45 GPa (B→C). This relaxation event indicates the initiation of a phase transformation (Olson and Cohen 1982). The HX phase nucleates near the wire's surface at a strain of 0.065 [Figure 5.1(a)]. As the deformation progresses, the transformed region sweeps through the whole specimen [C→D and configuration (ii) in Figure 5.1(b)] and the transformation is completed at a strain of 0.108 and a stress of 10.58 GPa [point D in Figure 5.1(a)]. Continued loading beyond point D causes elastic stretching of the transformed structure [D→E in Figure 5.1(a) and configuration (iii) in Figure 5.1(b)] and the eventual failure at a strain of 0.162 and a stress of 12.28 GPa through cleavage along $(\bar{1}2\bar{1}0)$ type planes.

Unloading of a HX structured wire from any strain prior to wire fracture activates the novel pseudoelastic behavior. Take the wire in Figure 5.1 for example; unloading from a strain of 14.5% (point F) initially results in the recovery of the elastic straining of the HX and goes beyond the end point of the WZ→HX transformation during loading (point D). This elastic unloading within the HX structure continues until point G where a reverse transformation from HX to WZ initiates at a strain of 0.087 and a stress of 7.38 GPa. Further unloading results in the complete reversal of the HX→WZ transformation at H (with a strain of 0.039 and a stress of 7.04 GPa). Unloading between H and A follows the elastic trend of the WZ phase and the hysteresis loop is completed.

For the wire in Figure 5.1, the total recoverable strain is ~16% which is significant since ZnO is a ceramic. The hysteretic energy dissipation in one loading and unloading cycle is ~0.14 GJm^{-3}. This dissipation level is significantly lower than that observed for wurtzite to rocksalt (WZ→RS) transformations in bulk ZnO (~1.38 GJm^{-3} per cycle), therefore, limiting heat generation and heat-related damage and making the nanowires ideal for applications involving cyclic loading and unloading (Desgreniers 1998). The low level of dissipation can be attributed to the fact that (1) the crystallographic transition between the WZ and HX structures, which does not require the formation of defects such as dislocations or twin boundaries, is smooth and (2) the energy barrier for the transformation between the WZ and the HX structures is relatively low (Kulkarni et al. 2006).

5.2 Effects of Size and Temperature

Temperature and lateral dimensions have significant effects on the pseudoelastic behavior of the wires. Figure 5.2(a-c) show the loading part of the stress-strain curves over 100-700 K for the 21.22×18.95, 31.02×29.42 and 40.81×39.89 Å nanowires, respectively. The critical stress for the nucleation of the HX phase (σ_c) is marked by open circles in these figures. Figure 5.2(d) shows the variation of this critical stress as a function of size and temperature. Overall, the critical stress decreases as the wire size is reduced. The critical stress also decreases as temperature is increased. Over the temperature range analyzed, σ_c for the 31.02×29.42 Å wire is up to 42 % higher than that for the 21.22×18.95 Å wire, while the values for the 40.81×39.89 Å wire are approximately 11-15% higher than those for the 31.02×29.42 Å wire.

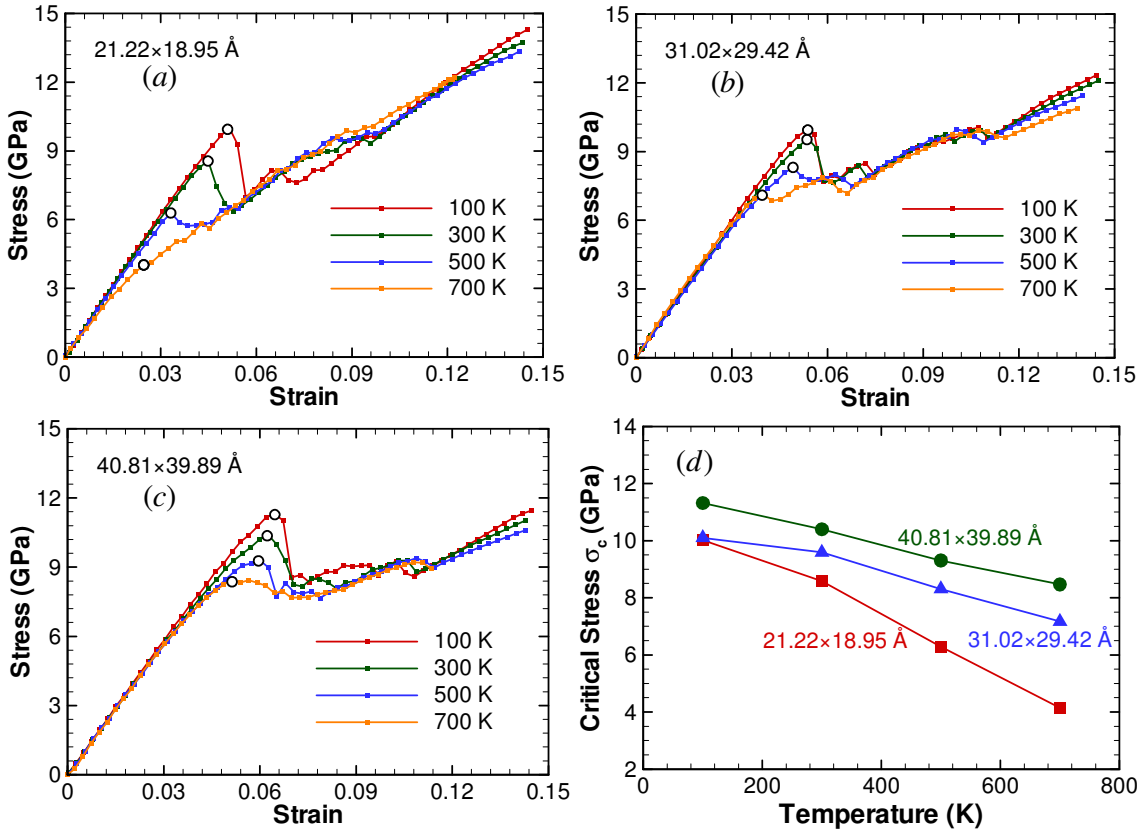

Figure 5.2 Stress-strain curves of (a) a 21.22×18.95 Å wire, (b) a 31.02×29.42 Å wire, and (c) a 40.81×39.89 Å wire at different temperatures; and (d) the critical stress for the initiation of phase transform (σ_c) as a function of lateral dimensions and temperature.

In contrast to the well-established trend that the stiffness of nanowires increases as wire size is reduced (Kulkarni and Zhou 2006b), σ_c decreases as the wire size is reduced. The higher surface-to-volume ratios at smaller wire sizes cause both effects. Note that, as the wire size is reduced from 50 Å to 10 Å, the surface-to-volume ratio increases by ~35%. In particular, for polar (0001) surfaces, the imbalance of charges results in extensive surface reconstruction. Figure 4.1 shows the positions of atoms on layers perpendicular to the [0001] direction before and after the initial relaxation. Obviously, relative to the ideal bulk structure, the surface layers contract and the Zn and O basal planes become essentially coplanar, resulting in a layered surface structure (LY) which is crystallographically similar to the HX structure. This phenomenon has been

predicted by first-principle calculations and observed in experiments on ZnO nanofilms (Claeyssens et al. 2005; Freeman et al. 2006). The reconstructed LY surfaces in the initial wire before loading play an important role because they can act as nucleation sites for and lower the energy barrier of the WZ→HX transformation due to the geometric similarities between the LY and HX structures. The smaller wire cores at smaller wire sizes facilitate the initiation of the phase transformation from the surfaces, resulting in the lower σ_c values.

As temperature increases from 100 K to 700 K, a 25.2% decrease in σ_c is observed for the 40.81×39.89 Å wire [Figure 5.2 (d)]. This effect is attributed to thermal softening and the ability of the nanowire to overcome the energy barrier for the transformation at higher temperatures. Note that over the same range of temperature, the elastic modulus of the nanowire decreases by 24% (Kulkarni and Zhou 2006b). Temperature changes also significantly affect hysteretic dissipation. To illustrate this effect, the stress-strain curves of the 40.81×39.89 Å wire at 100 K, 300 K, 500 K, and 700 K are shown in Figure 5.3. The corresponding dissipation during the loading-unloading cycle along with those for the 21.22×18.95, 31.02×29.42 wires at these temperatures is given in Figure 5.4. For the 40.81×39.89 Å wire, the dissipation decreases by 39.6% as temperature is increased from 100 K to 700 K. A similar trend is seen for the 21.22×18.95 and 31.02×29.42 Å wires which show decreases of 52.9% and 56.6%, respectively over the same temperature range.

Table 5.1 lists the values of several key parameters quantifying the pseudoelastic behavior at various cross-sectional sizes and temperatures. In particular, note that the maximum recoverable strain decreases significantly as temperature is increased, while the strain at which the WZ→HX transformation completes is essentially temperature-independent. The enhanced mobility of atoms at higher temperatures promotes the formation of defects and may be a factor contributing to the failure at lower strain levels.

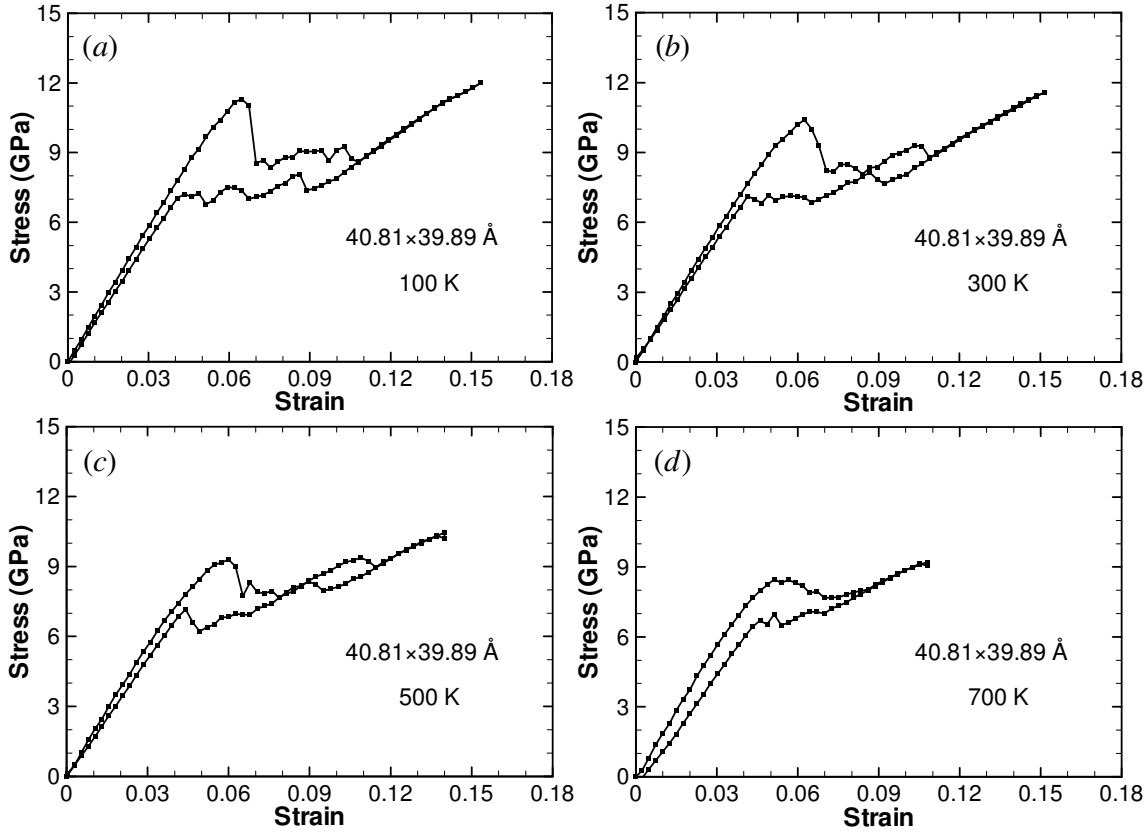

Figure 5.3 Stress-strain responses of a 40.81×39.89 Å wire during one loading-unloading cycle at (a) 100 K, (b) 300 K, (c) 500 K and (d) 700K.

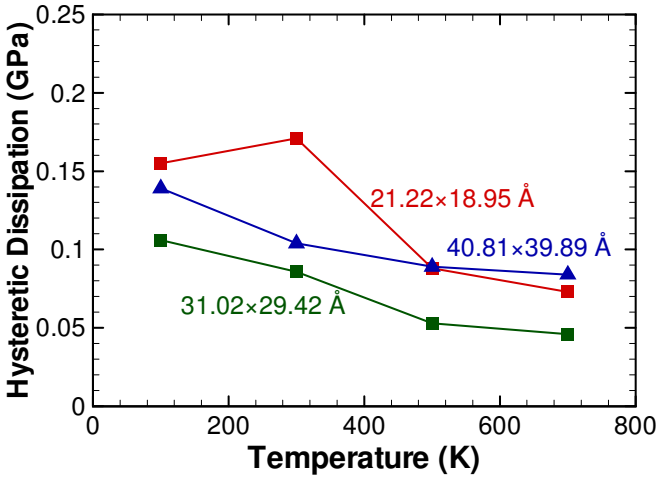

Figure 5.4 Hysteretic dissipation in one loading-unloading cycle as a function of lateral dimensions and temperature.

Table 5.1 Size and temperature dependence of the stress-strain response of the nanowires

Cross-section Dimensions ($Å^2$)	Temperature (K)	σ_c (GPa)	ε_c	Strain at completion of transformation	Maximum Recoverable Strain	Ultimate tensile strength (GPa)	Hysteretic Dissipation (GJm^{-3})
21.22×18.95	100	10.02	0.051	0.100	0.165	15.56	0.155
	300	8.59	0.045	0.096	0.155	14.50	0.171
	500	6.29	0.033	0.097	0.148	13.56	0.088
	700	4.15	0.027	0.091	0.127	12.34	0.073
31.02×29.42	100	10.10	0.053	0.110	0.155	13.05	0.106
	300	9.59	0.053	0.110	0.154	12.50	0.086
	500	8.31	0.049	0.098	0.140	11.44	0.053
	700	7.17	0.040	0.116	0.138	10.89	0.046
40.81×39.89	100	11.32	0.065	0.108	0.159	12.30	0.139
	300	10.40	0.063	0.109	0.162	11.68	0.104
	500	9.31	0.060	0.114	0.143	10.60	0.089
	700	8.47	0.051	0.086	0.108	9.21	0.084

5.3 Characterization of Deformation

The deformation can be quantified in a continuum sense through the deformation gradients $\boldsymbol{F}_i$ ($i = 1, 2,$ and 3) associated with the three stages of deformation, with $i = 1$ denoting the first stage [elastic stretching of WZ, A→B in Figure 5.1(a)], $i = 2$ denoting the second stage [transformation from WZ to HX, B→D in Figure 5.1(a)], and $i = 3$ denoting the third stage [elastic stretching of HX, D→E in Figure 5.1(a)]. In such an analysis, the deformation of a representative volume of $\Omega = \bar{a} \times \bar{b} \times \bar{c}$ (Figure 5.5) is used, with dimensions $\bar{a}$, $\bar{b}$ and $\bar{c}$ being the average values of lattice constants a, b and c, respectively. Since the average values of the lattice parameters are used here, the deformed wire is regarded as a repetition of this representative volume.

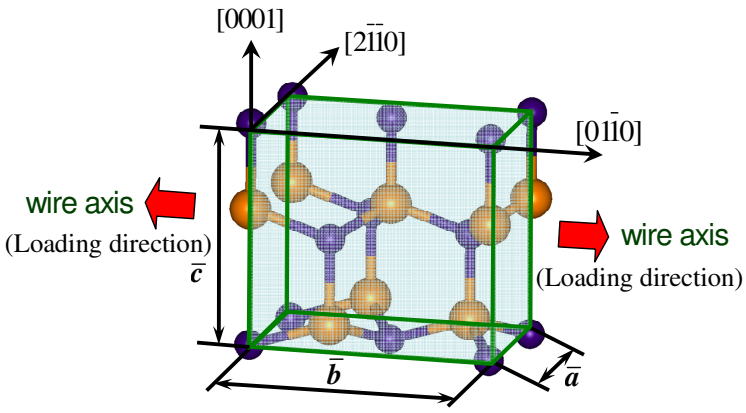

Figure 5.5 Representative volume defined in a unit cell of the wurtzite lattice for the purpose of deformation analysis.

The deformation gradient for each stage can then be expressed as

$$\boldsymbol{F}_i = \begin{pmatrix} \dfrac{\bar{a}_i}{\bar{a}_{i-1}} & 0 & 0 \\ 0 & \dfrac{\bar{c}_i}{\bar{c}_{i-1}} & 0 \\ 0 & 0 & \dfrac{\bar{b}_i}{\bar{b}_{i-1}} \end{pmatrix}, \quad i = 1, 2, 3. \tag{5.1}$$

In the above expressions, $\bar{a}_{i-1}, \bar{b}_{i-1}$, and $\bar{c}_{i-1}$ are the average lattice constants at the beginning of stage *i* and $\bar{a}_i, \bar{b}_i$, and $\bar{c}_i$ are the average lattice constants at the end of stage *i*. Note that $\bar{a}_0, \bar{b}_0$, and $\bar{c}_0$ are the constants for the initial (undeformed, WZ) wire. The relative volume change associated with stage *i* is

$$\frac{\Omega_i}{\Omega_{i-1}} = \det\left(\boldsymbol{F}_i\right), \tag{5.2}$$

where Ω is the volume of the wire at the beginning and end of stage *i*, respectively.

For a 40.81×39.89 Å wire at 100 K, the deformation gradient for the first stage [A→B in Figure 5.1(a)] is

$$\boldsymbol{F}_1 = \begin{pmatrix} 0.991 & 0 & 0 \\ 0 & 0.960 & 0 \\ 0 & 0 & 1.065 \end{pmatrix}. \tag{5.3}$$

The associated volume increase is 1.27% and the longitudinal (elastic) strain $\varepsilon_{33} = F_1^{33} - 1 =$ 0.065 consistent with that seen from the stress-strain curve in Figure 5.1(a).

During the second stage of deformation (phase transformation, [B→D in Figure 5.1(a)]), $\bar{a}$ increases and $\bar{c}$ decreases. The corresponding deformation gradient is

$$\boldsymbol{F}_2 = \begin{pmatrix} 1.047 & 0 & 0 \\ 0 & 0.876 & 0 \\ 0 & 0 & 1.043 \end{pmatrix}. \tag{5.4}$$

The volume ratio associated with the transformation is $\Omega_2/\Omega_1 = 0.957$, indicating a slight decrease in volume of 4.3%. This decrease in volume under tensile loading is counterintuitive. It is a direct consequence of the discrete lattice structure and the structural transformation. Specifically, the uniaxial tensile stress in the $[01\bar{1}0]$ or '*b*' direction causes the interatomic distances in the [0001] Zn and O basal planes (*a*) to

increase, causing the two types of basal planes to become coplanar and, therefore, the volume decrease.

The deformation gradient for the elastic deformation of the HX phase in the third stage [D→E in Figure 5.1(a)] is

$$\boldsymbol{F}_3 = \begin{pmatrix} 1.008 & 0 & 0 \\ 0 & 0.962 & 0 \\ 0 & 0 & 1.05 \end{pmatrix}. \tag{5.5}$$

Although the '*a*' and '*b*' directions are perpendicular to each other, *a* increases slightly (with a corresponding strain of $\varepsilon_{11} = 0.008$) under the tensile loading along the '*b*' direction. This gives rise to a negative phenomenological Poisson's ratio of

$$\nu_{13} = -\frac{\varepsilon_{11}}{\varepsilon_{33}} = -0.16\,. \tag{5.6}$$

The total elastic strain of the wire beyond the completion of the phase transformation and before fracture [between D and F in Figure 5.1(a)] is $\varepsilon_{33} = F_3^{33} - 1 = 0.05$. Here, the reference state of this strain is the length of the wire at the completion of transformation (point D). The corresponding volume increase is 1.68%.

Overall, the total strain of the wire between points A and E is $\varepsilon = F_1^{33} F_2^{33} F_3^{33} - 1 = 0.162$. Here, the reference length is the original length of the wire.

5.4 Micromechanical Continuum Model

As previously discussed, $[01\bar{1}0]$-oriented ZnO nanowires are found to undergo a reversible phase transformation from WZ to HX under tensile loading. This transformation leads to a pseudoelastic behavior. Figure 5.6 shows a schematic representation of this pseudoelastic response which can be decomposed into the following eight deformation stages:

1. (A→B): Elastic deformation of the WZ-structured wire;
2. (B→C): Precipitous drop in stress associated with the nucleation of the WZ-to-HX phase transformation;
3. (C→D): Propagation of the phase boundary from HX regions into WZ regions, with point D corresponding to the completion of the transformation;
4. D→E: Elastic deformation of the HX-structured wire;
5. E→F: Elastic unloading of the HX-structured wire, note that the unloading response continues beyond the point of initial transformation completion (D).
6. F→G: Nucleation of the reverse (HX-to-WZ) transformation with a corresponding stress increase;
7. G→H: Reverse transformation involving the propagation of the phase boundary from WZ regions into HX regions, culminating at point G where the entire nanowire reverts back to the WZ structure;
8. H→A: Elastic unloading of the WZ-structure wire.

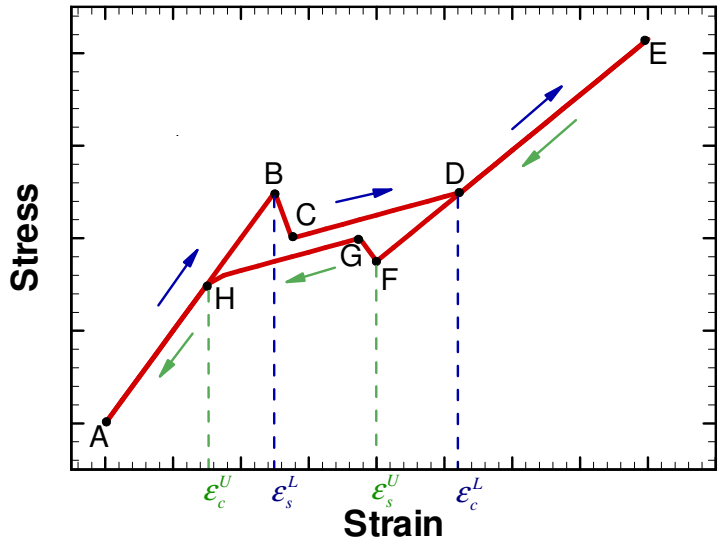

Figure 5.6 Schematic illustration of the pseudoelastic response of a $[0\bar{1}\bar{1}0]$-oriented nanowire under quasistatic loading and unloading.

This section discusses the development of a micromechanical continuum model that captures major characteristics of the overall pseudoelastic behavior of the nanowires. In what follows next, thermodynamic considerations are put forth to discuss the interplay between internal energy, energy dissipation and external work during loading and unloading. An expression for the total energy of the nanowires, including contributions from internal energies of the pure phases and the interface between the phases is formulated, allowing the elastic deformation process of the wires in one of the two pure phases before transformation initiation or after transformation completion (A→B, D→E, E→F, and B→A) and the elastic part of the deformation during the transformation process (B→C→D and F→G→H) to be characterized. The internal energies for the WZ and HX states are calculated using MD simulations. The energy contribution from the interfaces is quantified phenomenologically as a function of the volume fractions of the phases. Within this framework, the total energy depends on three parameters: (a) the strain in the WZ phase relative to its equilibrium state, (b) the strain in HX relative to its own equilibrium state and (c) the volume fractions of transformed and parent phases. At any given level of macroscopic deformation of a wire, these microscopic independent parameters are determined via constrained energy minimization. As the interfacial contribution to the total energy, the dissipative part of the transformation process associated with interface propagation is also accounted for phenomenologically, through a functional form with the volume fractions of the phases as independent state variables. Overall, the first law of thermodynamics allows an expression for the macroscopic stress to be obtained as the sum of a conservative contribution from the internal energy and a dissipative contribution from the interface propagation.

5.4.1 Thermodynamics of Loading and Unloading

The total deformation during the transformation can be regarded as a combination of a process of elastic transition between the equilibrium WZ and HX states and a process

of interface propagation. The first process is reversible and the second process is irreversible. At the macroscopic level, the reversible part involves the continuous evolution of the volume fraction of the transformed phase with the overall macroscopic strain and a part of the mechanical work from the applied stress is converted into bulk and interfacial strain energy. The irreversible part accounts for the dissipation associated with overcoming the energy barrier between the WZ and HX states as the transformation progresses through the propagation of the interfaces between the WZ and the HX regions. The first law of thermodynamics relates the change in internal energy, work input and dissipation as

$$\mathrm{d}W = \mathrm{d}U + \mathrm{d}Q\,. \tag{5.7}$$

where $\mathrm{d}W$ is the work done by applied loading, $\mathrm{d}U$ is the change in internal energy in the nanowire and $\mathrm{d}Q$ is the energy dissipated in the form of heat exchange. During the loading and unloading of single phase nanowires (A→B, D→E, E→F, and H→A in Figure 5.6), there is no dissipation (i.e., $\mathrm{d}Q = 0$). Hence,

$$\mathrm{d}W = \mathrm{d}U\,. \tag{5.8}$$

However, when phase transformation occurs (B→C→D and F→G→H in Figure 5.6), $|\mathrm{d}Q| > 0$.

Table 5.2 Signs of mechanical work, internal energy and dissipation during loading and unloading.

	$\mathrm{d}W$	$\mathrm{d}U$	$\mathrm{d}Q$
Loading (WZ→HX)	+	+	+
Unloading (HX→WZ)	−	−	+

Table 5.2 gives the signs of the three thermodynamic quantities. In this convention, work done on the system and heat dissipated (flowing out of the system) are considered positive and vice versa. During loading, external work $\mathrm{d}W$ is positive and

part of it goes toward increasing the strain energy $\mathrm{d}U$ and part of it is dissipated as heat $\mathrm{d}Q$. The relation can be written as

$$\left|\mathrm{d}W\right| = \left|\mathrm{d}U\right| + \left|\mathrm{d}Q\right|. \tag{5.9}$$

During unloading, the strain energy in the nanowire decreases. Part of the decrease is expended on providing work to the surroundings and part of it is dissipated as heat. The relation is

$$\left|\mathrm{d}W\right| = \left|\mathrm{d}U\right| - \left|\mathrm{d}Q\right|. \tag{5.10}$$

5.4.1.1 Macroscopic Stress and Strain

The total mechanical work is

$$W = V^0 \int_0^{\varepsilon} \sigma \, \mathrm{d}\varepsilon, \tag{5.11}$$

where σ and ε are the macroscopic stress and strain, respectively, and V^0 is the volume of the undeformed WZ wire. Here, the macroscopic strain ε is the nominal engineering strain relative to the undeformed WZ wire and is calculated as

$$\varepsilon = \frac{\Delta L}{L^0}, \tag{5.12}$$

with ΔL being the overall length change of the wire and L^0 being the length of the unstressed WZ wire. The total stress σ in the wire is

$$\sigma = \frac{1}{V^0}\frac{\partial W}{\partial \varepsilon}. \tag{5.13}$$

Thus, the stresses during loading and unloading are, respectively,

$$\begin{aligned} \sigma^L &= \frac{1}{V^0}\frac{\mathrm{d}U}{\mathrm{d}\varepsilon} + \frac{1}{V^0}\frac{\mathrm{d}Q}{\mathrm{d}\varepsilon} = \sigma^c + \sigma^d, \quad \text{during loading;} \\ \sigma^U &= \frac{1}{V^0}\frac{\mathrm{d}U}{\mathrm{d}\varepsilon} - \frac{1}{V^0}\frac{\mathrm{d}Q}{\mathrm{d}\varepsilon} = \sigma^c - \sigma^d, \quad \text{during unloading.} \end{aligned} \tag{5.14}$$

5.4.2 Elastic Part of the Behavior

5.4.2.1 Total Internal Energy

The total energy of the system is calculated using the framework developed by Muller and Raniecki (Muller 1989; Muller and Xu 1991; Raniecki and Lexcellent 1994, 1998; Hirsinger et al. 2004). In the following discussions, subscripts 1 and 2 refer to the WZ and HX phases, respectively. The total internal energy of the phase mixture is expressed as the sum of the internal energy of WZ (U_1), the internal energy of HX (U_2) and the energy of the interface between the two phases (U_{int}). Specifically, the total energy of the system is

$$U = U_1 + U_2 + U_{\text{int}} . \tag{5.15}$$

The internal energy of the pure phases in the mixture can be written as

$$U_p = U_1 + U_2 = u_1 V_1^0 + \tilde{u}_2 V_2^0 , \tag{5.16}$$

where u_1 is the energy density of the WZ phase reckoned over the "undeformed" volume $\left(V_1^0\right)$ of the WZ phase at zero stress and $\tilde{u}_2$ is the energy density of the HX phase reckoned over the hypothetical free volume of the HX phase $\left(V_2^0\right)$ at zero stress accounting for the volumetric change associated with the WZ→HX transformation. Specifically,

$$\begin{aligned} u_1 &= \frac{U_1}{V_1^0}, \text{ and} \\ \tilde{u}_2 &= \frac{U_2}{V_2^0}. \end{aligned} \tag{5.17}$$

At a given level of macroscopic strain ε, the total current volume of the wire is V and the current volumes of the WZ and HX regions are V_1 and V_2, respectively. For the purpose of formulating a consistent theory, it is illustrative to define the volumes V_1^0 and

V_2^0 the WZ and HX regions of the wire would assume, respectively, if they were unloaded to zero stress *with the current phase boundary held unchanged* (i.e., unloading without phase transformation). For WZ, this imagined unloading is physically possible and simply involves the recovery of the elastic deformation. For HX, this imagined unloading is not possible since the HX structure does not exist at zero stress. Here, V_2^0 is defined through

$$V_2^0 = V_1^0 (1+\xi). \tag{5.18}$$

where ξ represents the volumetric strain associated with the WZ→HX phase transformation. This volumetric strain changes slightly with wire size and temperature and is $\xi = -4.3\%$ for a 40.81×39.89 Å wire at 100 K. For the wires size and temperature ranges analyzed, ξ is found to be between -1.6 to -4.3%. Note that the definition in Eq. (5.18) is rather an instrument that facilitates the formulation of relevant quantities (energy densities, in particular) relative to fixed reference states. With the above definitions, the expression in Eq. (5.16) can be written as

$$U_p = u_1 V_1^0 + u_2 \frac{V_2^0}{(1+\xi)}; \quad u_2 = \frac{U_2}{V_1^0}. \tag{5.19}$$

In the above relations, the energy densities of both phases are referred to the undeformed volume of WZ. It should be pointed out that the specific values of ξ and its size- and temperature-dependencies are implicitly accounted for in the MD calculations that yield u_1 and u_2 directly for each set of conditions.

During the transformation, conservation of mass dictates that the sum of the masses of the two phases be equal to the total mass of the nanowire, i.e.,

$$M_1 + M_2 = M, \tag{5.20}$$

where $M_1 = \rho_1 V_1^0$ and $M_2 = \rho_2 V_2^0$ are the masses of the WZ and HX phases, respectively, $M = \rho_1 V^0$ is the mass and V^0 is the volume of the unstressed WZ nanowire. ρ_1 and ρ_2

are the densities of WZ and HX, respectively. Since the mass of the HX phase can also be expressed as

$$M_2 = \rho_1 \frac{V_2^0}{(1+\xi)}, \tag{5.21}$$

Eq. (5.20) reduces to

$$V_1^0 + \frac{V_2^0}{(1+\xi)} = V^0. \tag{5.22}$$

This states that the sum of the volumes of the untransformed WZ phase and the transformed HX phase referred to its equivalent volume in the WZ state are equal to the original undeformed volume of the wire. Equation (5.22) can also be written as

$$\frac{V_1^0}{V^0} + \frac{V_2^0}{V^0(1+\xi)} = 1, \tag{5.23}$$

where the terms on the left hand side represent the volume fractions of the WZ and HX phases, respectively. Equations (5.19) and (5.23) combine to give the total strain energy density of the pure phases as

$$u_p = (1-f)u_1 + fu_2, \tag{5.24}$$

where $f = V_2^0 \big/ \left[V^0(1+\xi)\right]$ is the volume fraction of the HX phase.

5.4.2.2 Internal Energy of WZ and HX Phases

The internal energy densities of the WZ- and HX-structured nanowires (u_1 and u_2) are critical in the modeling of the phase transformation, since they determine the relative stability of the two phases and the evolution of the transformation. In nanowires, the internal energy depends not only on the bulk structure and deformation but also on surface orientations and surface energies. Due to the high surface-to-volume ratios, surface energy constitutes a major portion of the total configurational energy. The surface energy and the internal energy of a nanowire are functions of wire size. This phenomenon

is different from what is the case for bulk materials whose internal energy depends solely on strain. In addition, it is useful to note that the internal energy does not vanish at zero strain (or zero stress). Here, the strain defined relative to the equilibrium bulk state. As shown by Sander (Sander 2003), the surface energy curve has a positive slope at zero surface strain, indicating that the minimum surface energy occurs at a compressive surface strain. This is a consequence of the reduced charge transfer and imbalance of ionic forces on surfaces where atoms have fewer neighbors relative to those in the core. As a result, WZ-structured nanowires undergo relaxation through surface reconstruction and adjustment of interior lattice spacing, leading to lower overall configurational energy. In this paper, this relaxed state is taken as the reference state. The strain in the WZ structure (ε_1) defined with respect to this reference state is

$$\varepsilon_1 = \frac{l_1 - l_1^0}{l_1^0}, \tag{5.25}$$

where l_1 and l_1^0 are the current and reference lengths. For the HX phase, special considerations similar to those in the definition of V_2^0 are required. Since HX does not exist at zero stress, the strains in the HX phase are defined relative to the reference length of

$$l_2^0 = l_1^0 (1+\eta). \tag{5.26}$$

Here, η is the longitudinal strain associated with the WX-to-HX transformation and, according to MD calculations, has values in the range of 2.3 – 4.3% for the wire sizes and temperatures analyzed. With the reference state, the strain in HX is defined as

$$\varepsilon_2 = \frac{l_2 - l_2^0}{l_2^0}. \tag{5.27}$$

The internal energy density of each phase is expressed as

$$u_i = u_i^0 + u_i^\varepsilon (\varepsilon_i), (i = 1, 2). \tag{5.28}$$

Here, u_i^0 is the energy of formation, $u_i^{\varepsilon}(\varepsilon_i)$ is the strain energy density and ε_i is the strain of the i^{th} phase. The formation energy depends on temperature and the elastic constants are functions of both temperature and strain.

The one-dimensional nature of the wires and the uniaxial tensile loading permits the use of 1D internal energy functions. For each phase, the internal energy density at each wire size and each temperature is obtained through MD calculations. The internal energy functions thus developed account for the effects of temperature and size (through explicit inclusion of surfaces in the MD model), allowing the size- and temperature-dependence of wire responses to be analyzed. Figure 5.7 shows the internal energy densities of WZ and HX structures for a 40.81×39.89 Å wire at 100 K. The formation energies of the two phases are indicated. Note that the formation energy of WZ is lower than that of HX, consistent with the fact that WZ is the natural state of the wires at 100 K without external loading.

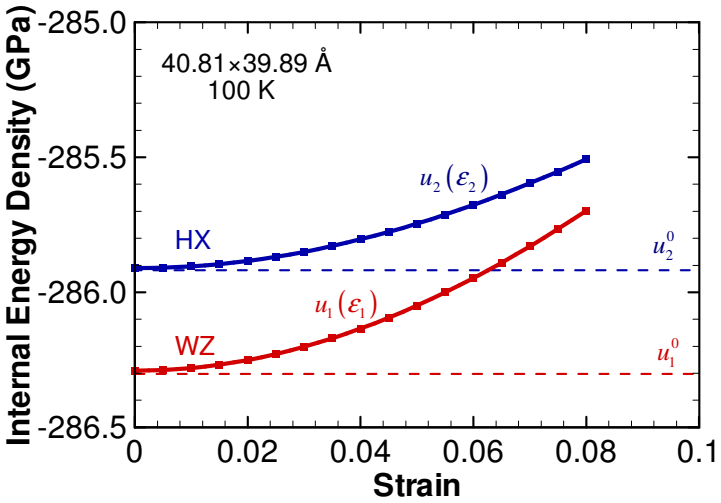

Figure 5.7 Internal energy density functions of a 40.81×39.89 Å wire in WZ and HX phases.

5.4.2.3 Interfacial Energy

Interfacial energy includes contributions from the formation energy of the interface, elastic misfit of the phases and elastic interactions of neighboring domains. Its accurate evaluation is somewhat complicated and various methods have been proposed in the literature (Gall et al. 2000; Muller and Bruhns 2006), primarily due to complex geometry and anisotropy. Here, the phenomenological approach developed by Muller and Xu (1991) is adopted. Specifically, the interfacial energy density is written as

$$u_{\text{int}} = \frac{U_{\text{int}}}{V^0} = 4f(1-f)u_{\text{int}}^m, \tag{5.29}$$

where u_{int}^m is the maximum value when the wire is evenly divided by the WZ and HX phases ($f = 0.5$). Obviously, $4f(1-f) = u_{\text{int}}/u_{\text{int}}^m = S_{\text{int}}/S_{\text{int}}^m$ denotes both the normalized interfacial energy $u_{\text{int}}/u_{\text{int}}^m$ and the normalized interfacial area $S_{\text{int}}/S_{\text{int}}^m$ (Muller and Xu 1991). Here, S_{int} is the interfacial area at a prescribed value of macroscopic strain ε and S_{int}^m is its corresponding maximum value at $f = 0.5$. Note that u_{int} vanishes at $f = 0$ and 1. One underlying assumption of Eq. (5.29) is that the orientation dependence of interfacial energy is negligible and the interfacial energy is only a function of the interfacial area. Figure 5.8 provides a comparison of the model prediction and the MD result of $u_{\text{int}}/u_{\text{int}}^m$ as a function of strain for a 40.81×39.89 Å wire at 100 K. Very good agreement is seen between the mode prediction and the MD data. The part of the profile from the model between $\varepsilon = 0.04$ and 0.072 is not physical and not observed in MD since the model does not account for the energy barrier for the WZ-to-HX transformation. More discussion on this will be given in section 5.4.3.

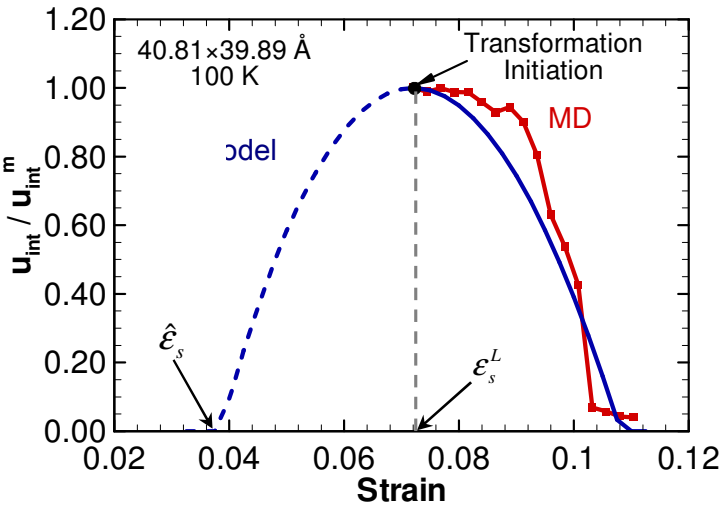

Figure 5.8 Comparison of the model predictions and MD results for the normalized interfacial energy with applied strain obtained for a 40.81×39.89 Å wire at 100 K.

5.4.2.4 Constrained Energy Minimization

The total internal energy density resulting from Eq. (5.15) is

$$u = (1-f)u_1 + fu_2 + 4f(1-f)u_{\text{int}}^m. \tag{5.30}$$

The macroscopic strain ε includes contributions from the elastic strains in the phases (ε_1 and ε_2) and the transformation strain (η) can be obtained by invoking the rule of mixture as

$$\varepsilon = (1-f)\varepsilon_1 + f\varepsilon_2 + f\eta. \tag{5.31}$$

Obviously in Eq. (5.30), the independent state variables are ε_1, ε_2 and f. At any given level of macroscopic strain ε, minimization of the total energy density in (5.30) under the constraint of Eq. (5.31) yields the equilibrium condition that defines the equilibrium state (specified by ε_1, ε_2 and f) of the transforming nanowire. When carried over the whole range of ε, this constrained minimization process yields the full equilibrium path for both the forward WZ-to-HX and the reverse HX-to-WZ transformations. The equilibrium transformation path so obtained for the 40.81×39.89 Å wire at 100 K as measured by f as a function of ε is shown in Figure 5.9. Initially for $\varepsilon < 0.04$, $f = 0$

and the wire exists solely in the WZ phase. At $\varepsilon = \hat{\varepsilon}_s = 0.04$, the WZ-to-HX transformation initiates. Note, however, that $\hat{\varepsilon}_s$ is not equal to the actual transformation initiation strain observed in MD simulations (ε_s^L in Figure 5.6). This difference arises from the fact that the equilibrium analysis does not account for the energy barrier for the forward WZ-to-HX transformation. The actual transformation initiation occurs at ε_s^L in Figure 5.6 and Figure 5.8. As the transformation progresses, the volume fractions of the two phases evolve smoothly. The transformation is complete at $\varepsilon = \varepsilon_c = 0.11$ for the wire in Figure 5.8. Further deformation beyond ε_c corresponds to the purely elastic stretch of the HX-structured wire with $f = 1$.

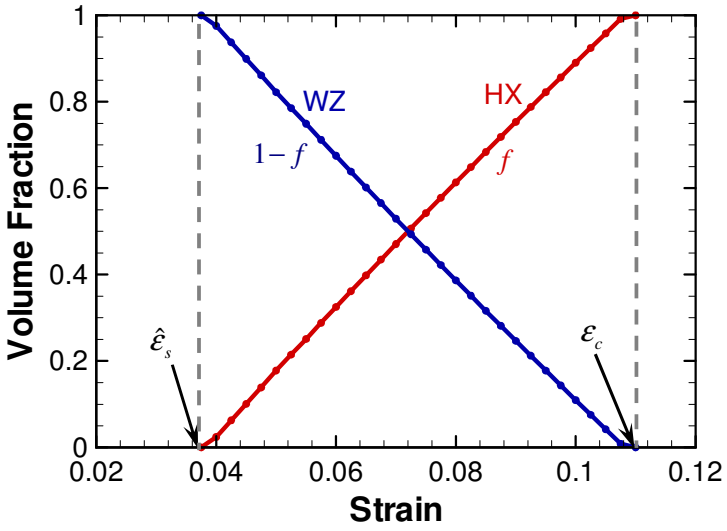

Figure 5.9 Evolution of WZ and HX volume fractions as predicted by the model for a 40.81×39.89 Å wire at 100 K under tensile loading.

5.4.2.5 Stress Associated with Equilibrium Transformation Process (σ_c)

During the transformation, the equilibrium part of the stresses in the phases is

$$\sigma_1 = \frac{\partial u_1}{\partial \varepsilon_1} \text{ and}$$
$$\sigma_2 = \frac{\partial u_2}{\partial \varepsilon_2}. \tag{5.32}$$

The stress associated with the equilibrium transformation process is then [Eq. (5.14)]

$$\begin{aligned}
\sigma_c &= \frac{1}{V_0}\left(\frac{\partial U}{\partial \varepsilon}\right) \\
&= \frac{1}{V_0}\left(\frac{\partial U_p}{\partial \varepsilon}\right) + \frac{1}{V_0}\left(\frac{\partial U_{\text{int}}}{\partial \varepsilon}\right) \\
&= \frac{1}{V_0}\frac{\partial}{\partial \varepsilon}\left(u_1 V_1^0\right) + \frac{1}{V_0}\frac{\partial}{\partial \varepsilon}\left[u_2 \frac{V_2^0}{(1+\xi)}\right] + \frac{1}{V_0}\frac{\partial}{\partial \varepsilon}\left[4f(1-f)u_{\text{int}}^m\right] \\
&= \frac{\partial}{\partial \varepsilon}\left[u_1(1-f)\right] + \frac{\partial}{\partial \varepsilon}(u_2 f) + 4(1-2f)u_{\text{int}}^m \frac{\partial f}{\partial \varepsilon} \\
&= (1-f)\frac{\partial u_1}{\partial \varepsilon_1}\frac{\partial \varepsilon_1}{\partial \varepsilon} + f\frac{\partial u_2}{\partial \varepsilon_2}\frac{\partial \varepsilon_2}{\partial \varepsilon} + \frac{\partial f}{\partial \varepsilon}(u_2 - u_1) + 4(1-2f)u_{\text{int}}^m \frac{\partial f}{\partial \varepsilon} \\
&= (1-f)\left(\frac{\partial \varepsilon_1}{\partial \varepsilon}\right)\sigma_1 + f\left(\frac{\partial \varepsilon_2}{\partial \varepsilon}\right)\sigma_2 + \frac{\partial f}{\partial \varepsilon}(u_2 - u_1) + 4(1-2f)u_{\text{int}}^m \left(\frac{\partial f}{\partial \varepsilon}\right).
\end{aligned} \tag{5.33}$$

Here, ε_1, ε_2, $\partial\varepsilon_1/\partial\varepsilon$, $\partial\varepsilon_2/\partial\varepsilon$ and f as functions of ε are determined from the constrained energy minimization process discussed in section 5.4.2.4.

σ_c describes the reversible part of the deformation process. Note that Eq. (5.33) is also applicable to the wire as it deforms fully elastically in the WZ state before the initiation of the transformation ($f = 0$) and in the HX state after the completion of the transformation ($f = 1$). For example, for the loading and unloading of a single phase WZ wire,

$$f = 0, \quad \frac{\partial f}{\partial \varepsilon} = 0 \text{ and } \frac{\partial \varepsilon_1}{\partial \varepsilon} = 1. \tag{5.34}$$

The stress reduces to that in the WZ phase, i.e.,

$$\sigma = \sigma_1.. \tag{5.35}$$

Similarly, for the elastic loading and unloading of a single phase HX wire, $f = 1$, $\partial f / \partial \varepsilon = 0$, $\partial \varepsilon_2 / \partial \varepsilon = 1$ and $\sigma = \sigma_2$.

Note that σ_c only captures equilibrium part of the transformation process, since the nanowire goes through a sequence of unstable and equilibrium states (more discussions in section 5.4.3). For example, the stress-strain response of the 40.81×39.89 Å wire at 100 K is given in Figure 5.10. Both the MD data and the model prediction for σ_c are shown. The MD profile shows alternate stages of stress increases (toward unstable states) and decreases (toward equilibrium states) during loading and alternate stages of stress decreases (toward unstable states) and increases (toward equilibrium states) during unloading. Obviously, σ_c are close to the valleys in loading and the peaks in unloading since these valleys (loading) and peaks (unloading) correspond to more relaxed states of the nanowire.

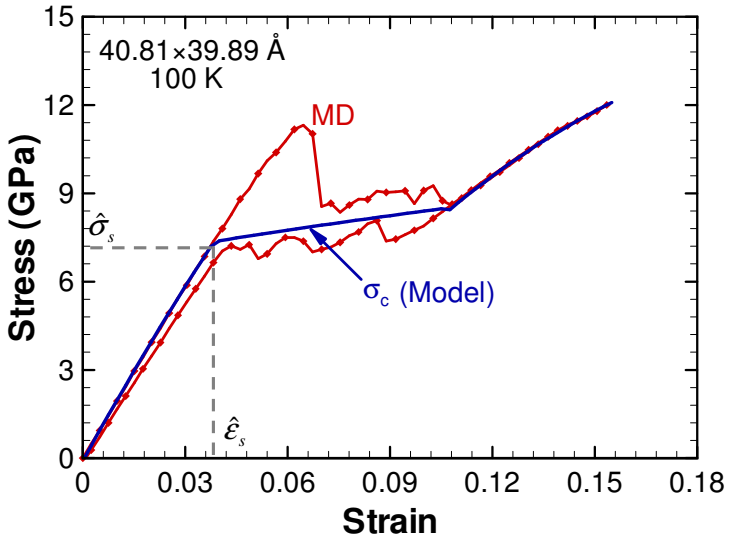

Figure 5.10 Comparison of predicted values of σ_c with the MD results for 40.81×39.89 Å wire at 100 K under uniaxial loading-unloading.

5.4.3 Dissipative Process of Interface Propagation

The irreversible part of the phase transformation involves contributions from barriers for both the initiation and propagation of the transformation through the nucleation and motion of interfaces. A schematic illustration of the energy and stress profiles associated with the process is given in Figure 5.11. The initiation of transformation occurs at the formation of the first nucleus of the HX phase (forward WZ-to-HX transformation during loading) or the WZ phase (reverse HX-to-WZ transformation during unloading). The stress at which the WZ-to-HX transformation initiates (point B, Figure 5.6) can be obtained from the value of ε_s^L and the constitutive behavior of the WZ phase (Figure 5.7). Similarly, the stress at which the WZ-to-HX transformation initiates (point F, Figure 5.6) can be obtained from the value of ε_s^U and the constitutive behavior of the HX phase (Figure 5.7). Since the elastic behaviors for $\varepsilon < \varepsilon_s^L$ (A↔B, Figure 5.6) and $\varepsilon > \varepsilon_s^U$ (F↔E, Figure 5.6) are also fully described by the single phase responses of the WZ and HX wires, respectively, the discussion on the dissipative process of interfacial propagation concerns only the deformation stages of C→D (loading) and G→H (unloading).

The propagation of phase boundaries after phase nucleation involves a sequence of unstable and stable states. This process is a consequence of the ruggedness of the energy profiles associated interface propagation. For example, during loading, the nanowire initially stores energy [C→P in Figure 5.11(a)] and is brought to an unstable high energy state [point P in Figure 5.11(a)]. At point P, the wire reaches instability and further nucleation of the HX phase takes place, resulting in the propagation of the phase boundary. This structural change is accompanied by an energy drop ΔU from its value at point P to the value at point V, bringing the wire closer to the more relaxed equilibrium state represented by the dotted line. The released energy ($\Delta U = U^P - U^V$) is dissipated as heat and constitutes part of the dissipation $\Delta Q^{P\to V}$ as defined in Eq. (5.7).

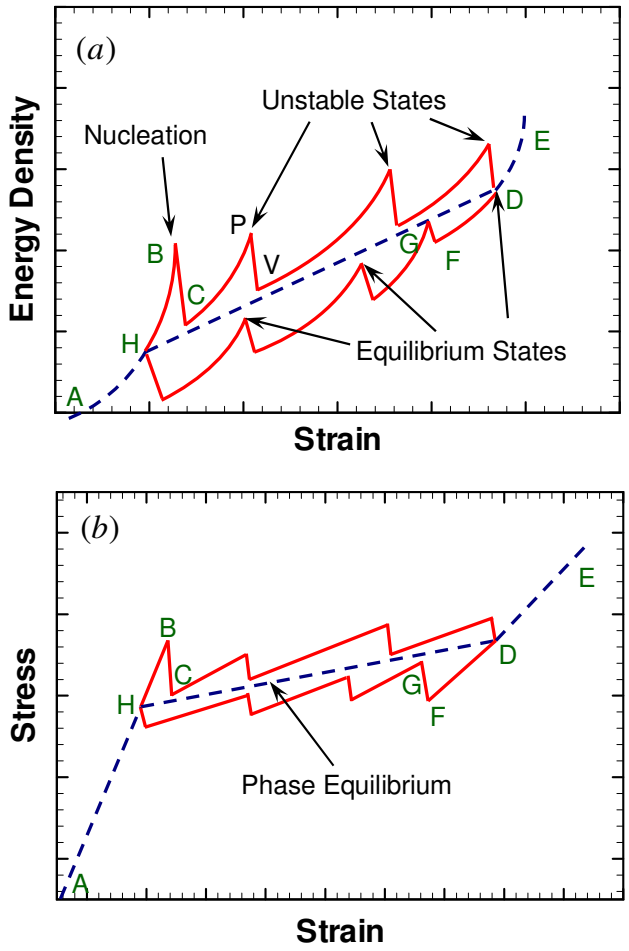

Figure 5.11 Schematic representation of the variations in (a) internal energy density and (b) stress, during transformation.

During this period of "energy accumulation and release", stress σ first increases between A and B and decreases precipitously between B and C [Figure 5.11(b)]. The stress at C may approach σ_c in Eq. (5.33). Figure 5.12 shows several configurations in the stage of $0.075 < \varepsilon < 0.084$ of the nanowire referred to in Figure 5.8 and Figure 5.10. These pictures show states of the wire immediately after the initiation of the WZ-to-HX transformation. Obviously over this stage (strain up to 0.08), the structure of the wire remains essentially unchanged without significant progression of transformation in either direction (therefore, without significant dissipation), while at the same time the mechanical work input is converted into strain energy and stored in the wire. As soon as

the strain exceeds 0.08, the interface starts to propagate and clear progression of the WZ-to-HX transformation occurs. This process is a direct reflection of the ruggedness of the energy landscape discussed earlier.

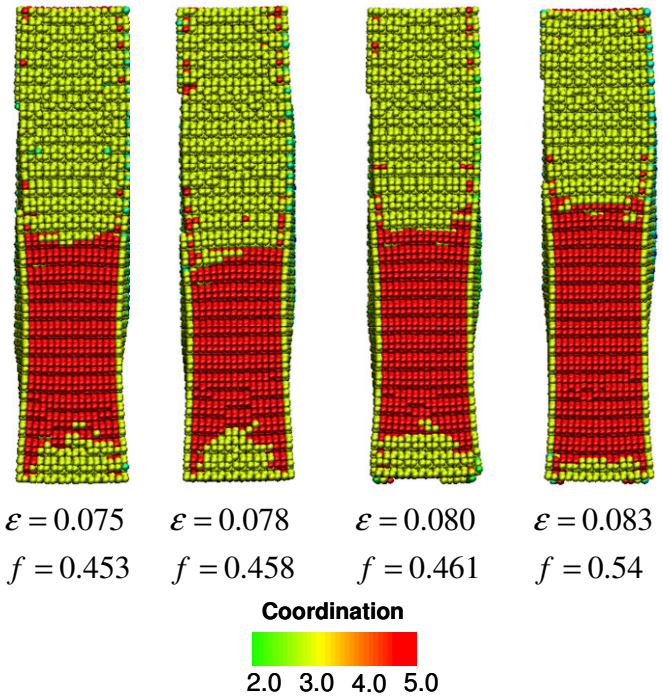

Figure 5.12 Nanowire configurations during loading of 40.81×39.89 Å wire at 100 K. Note that the volume fraction f is almost constant for $\varepsilon \le 0.08$ and changes significantly for $\varepsilon > 0.08$.

Just as the interfacial energy is proportional to the interfacial area, the energy required to move the WZ-HX phase boundaries naturally increases with the size of the interface, leading to a dependence of the dissipative stress (σ_d) on the size of the phase boundary which changes as the transformation progresses. To reflect this dependence, σ_d is assumed to be proportional to the normalized interfacial area fraction $S_{\text{int}}/S_{\text{int}}^m$ and varies with f according to

$$\sigma_d = 4f(1-f)\sigma_d^m. \tag{5.36}$$

Here, σ_d^m is the maximum value of σ_d which occurs at $f = 0.5$. The history of σ_d/σ_d^m is shown in Figure 5.13(a) and the history of energy dissipated per unit volume

$q = Q/V^0$ normalized by its maximum value is shown in Figure 5.13(b). For comparison, the history of f as a function of ε for the nanowire referred to in Figure 5.8 and Figure 5.10 is also shown. Note that $\sigma_d = 0$ for $f = 0$ $(\varepsilon \le \hat{\varepsilon}_s)$ and $f = 1$ $(\varepsilon \ge \varepsilon_c)$.

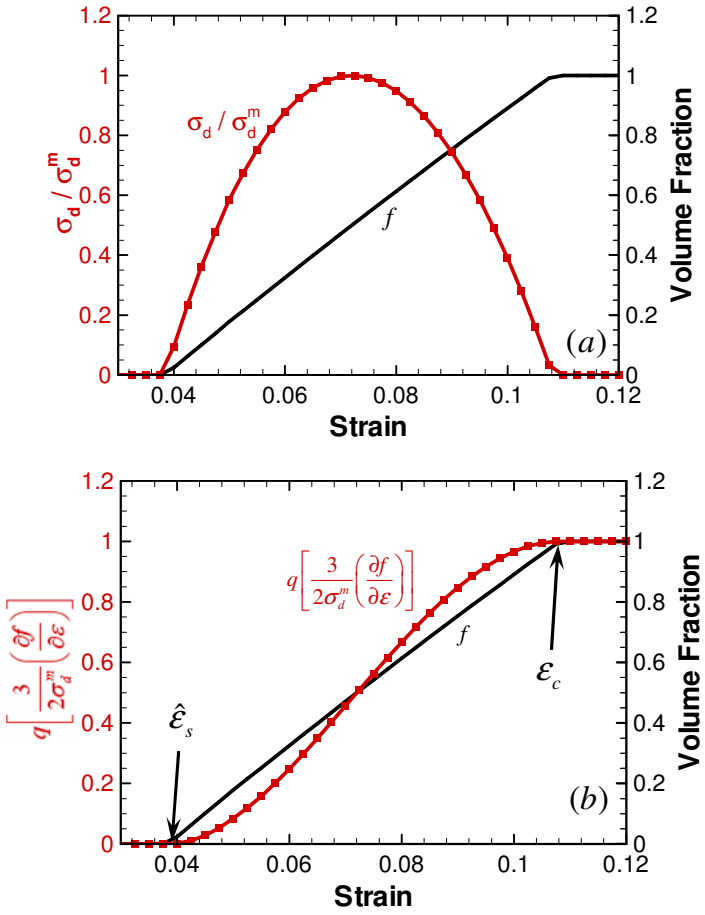

Figure 5.13 Evolution of (a) normalized stress associated with dissipation and (b) normalized energy dissipated, with strain during the transformation.

5.4.4 Macroscopic Stress σ

Equations (5.14), (5.33) and (5.36) combine to give the macroscopic stress as

$$\sigma = \frac{1}{V_0}\left(\frac{\partial U}{\partial \varepsilon}\right) \pm \frac{1}{V_0}\left(\frac{\partial Q}{\partial \varepsilon}\right)$$

$$= \underbrace{(1-f)\left(\frac{\partial \varepsilon_1}{\partial \varepsilon}\right)\sigma_1 + f\left(\frac{\partial \varepsilon_2}{\partial \varepsilon}\right)\sigma_2 + \frac{\partial f}{\partial \varepsilon}(u_2 - u_1) + 4(1-2f)u_{\text{int}}^m\left(\frac{\partial f}{\partial \varepsilon}\right)}_{\sigma^c} \pm \underbrace{4f(1-f)\sigma_d^m}_{\sigma^d}, \quad (5.37)$$

where the positive and negative signs correspond to loading and unloading, respectively.

5.4.5 Comparison with MD Results

The stress-strain relation predicted by the model and that obtained from MD simulations for the 40.81×39.89 Å wire at 100 K are shown in Figure 5.14.

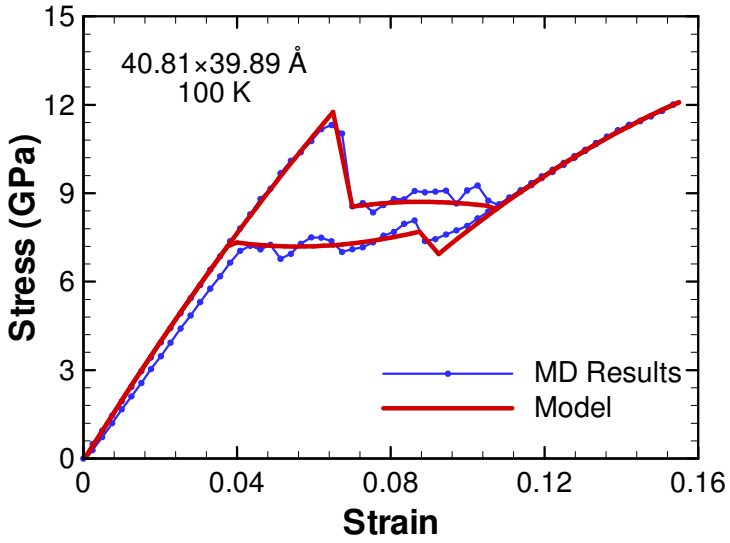

Figure 5.14 Comparison of MD results and predicted values of σ for 40.81×39.89 Å wire under tensile loading-unloading at 100 K.

In calculating the model results, the constitutive behaviors of the two phases are determined by fitting to MD calculations, as detailed in section 5.4.2.2. The elastic part of the stresses (σ_i) and the strain (ε_i) in each phase, the derivatives of the strains ($\partial\varepsilon_i/\partial\varepsilon$) and the volume fraction f at each ε are calculated through constrained energy minimization. The model developed here has two independent parameters (u_{int}^m and σ_d^m). The maximum interfacial energy density (u_{int}^m) is related to the evolution of equilibrium states and is determined through fitting to MD results for each size and temperature. The value of u_{int}^m and its variation with temperature and size determines the phase equilibrium stress during the evolution of the transformation for various wire sizes and temperatures.

On the other hand, the maximum value of dissipative stress (σ_d^m) is related to the dissipation associated with interface propagation and its value determines the size of the hysteresis loop in a loading-unloading cycle. The value of σ_d^m is also determined by fitting to MD results for the wire sizes and temperatures considered. The individual contributions to the macroscopic stress for the WZ-to-HX forward transformation are compared in Figure 5.15. The primary contribution (~83%) comes from the gradient term $\partial f/\partial\varepsilon\left(u_2-u_1\right)$ which decreases slightly as ε increases, reflecting the fact that most of the external work dW is converted into the internal energy of the HX phase. The contributions of the other terms are relatively low. The term $(1-f)\left(\partial\varepsilon_1/\partial\varepsilon\right)\sigma_1$ decreases as the volume fraction of the HX phase increases, while the term $f\left(\partial\varepsilon_2/\partial\varepsilon\right)\sigma_2$ shows a gradual increase. The dissipative stress σ_d first increases and then decreases. The contribution from the interfacial energy $4\left(1-2f\right)u_{\text{int}}^m\left(\partial f/\partial\varepsilon\right)$ is also quite small (< 7% of the overall stress) throughout the transformation.

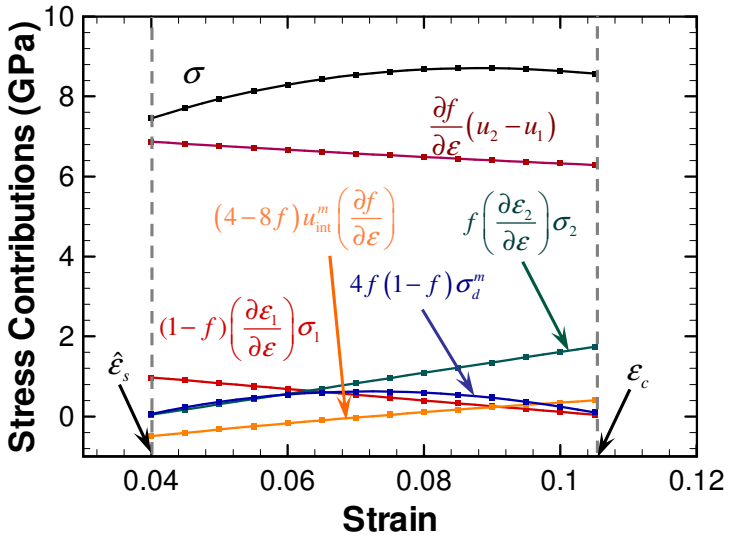

Figure 5.15 Decomposition of the total stress into individual contributions from associated stress quantities represented in Eq. (5.37).

The relative magnitudes of these terms affect the size and temperature dependence of the behavior of the wires. To quantify the effects, the micromechanics framework developed here is used to analyze the pseudoelastic behavior of wires with the lateral dimensions of 21.22×18.95, 31.02×29.42 and 40.81×39.89 Å over the temperature range of 100-500 K. The internal energy functions of the WZ and HX phases for these sizes and temperatures are calculated using MD simulations. The model predictions and MD results are shown in Figure 5.16. Excellent agreement is seen for all the cases analyzed. Obviously, the model captures the overall characteristics of the behaviors of the wires and correctly accounts for the size and temperature effects.

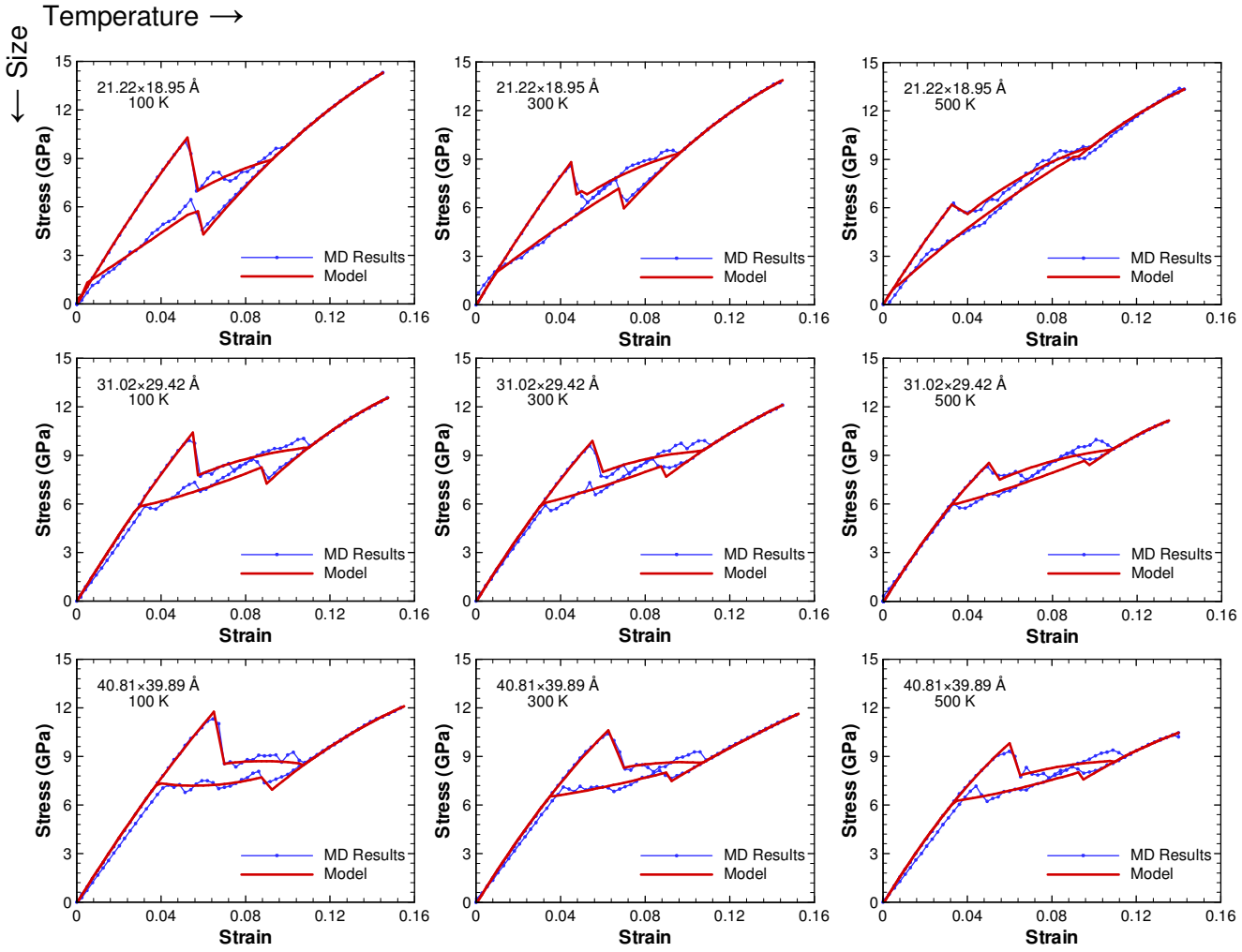

Figure 5.16 MD results and model predictions for the size and temperature effects on the pseudoelastic response of the nanowires.

5.4.5.1 Size and Temperature Effects

To analyze the effects of size and temperature, the responses of three wire sizes (21.22×18.95, 31.02×29.42 and 40.81×39.89 Å) at 300 K and the response of a 31.02×29.42 Å wire at three temperatures are considered.

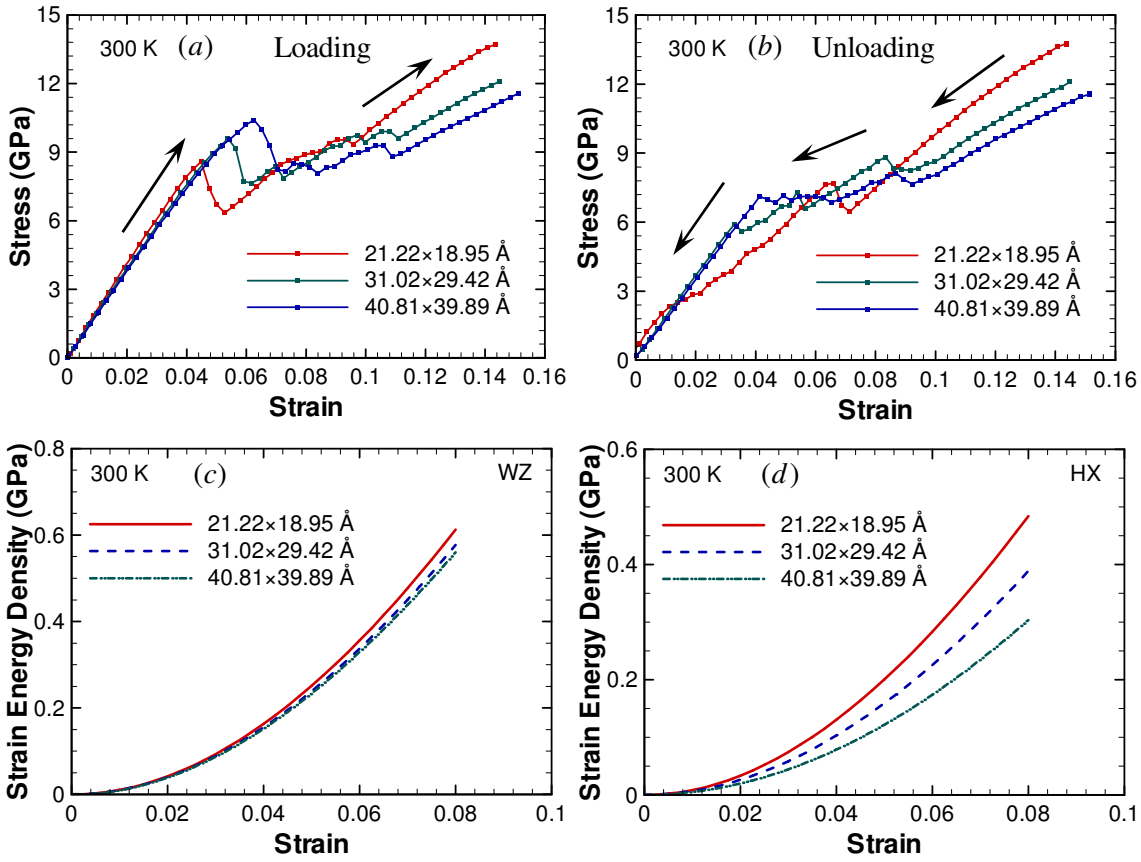

Figure 5.17 Size-dependence of response. (a) Loading and (b) unloading response at 300 K, (c) strain energy function for WZ structure and (d) strain energy functions for HX structure.

The effect of wire size on response is analyzed in Figure 5.17(a) (loading) and Figure 5.17(b) (unloading). The MD results shown are obtained for a temperature of 300 K. The elastic moduli in the elastic stages of deformation increase with wire size, owing to the higher surface-to-volume ratios at smaller sizes. This stiffening effect can be

explained by the strain energy profiles for WZ [Figure 5.17(c)] and HX [Figure 5.17(d)]. The size-dependence is more pronounced for the HX structure, primarily because the energy densities of the surfaces for HX wires are higher than the energy densities of the surfaces of the WZ wires. The critical stresses for transformation initiation decrease as wires size decreases. Again, the effect of surfaces is at work and the mechanism has to do with the fact that the structure of reorganized (0001) side surfaces of WZ wires have atomic configurations similar to those of the surfaces of HX-structured wires, as previously observed by (Claeyssens et al. 2005; Freeman et al. 2006) in both experiments and first principles calculations. The similarity in surface behaviors between WZ- and HX-structured wires allows bulk behavior to dominate the transformation process. The higher surface-to-volume rations at smaller wire sizes reduce the effect of the wire core, causing the critical stresses to decrease with size, despite the fact that the formation energy difference between HX and WZ wires (Δu^0) is slightly higher at smaller wires sizes [Figure 5.18(a)]. This effect can be phenomenologically seen from the values of the maximum interfacial energy u_{int}^m in Figure 5.18(b) and the values of $\hat{\sigma}_s$ [the stress corresponding to the strain of $\varepsilon = \hat{\varepsilon}_s$ (Figure 5.10) at which the two phases are equally favored under equilibrium conditions] in Figure 5.18(c). Finally, it is worthwhile to note that the dissipative process of interfacial propagation does not have an appreciable contribution to the size dependence of the overall wire response, as can be seen from Figure 5.18(d) which relates σ_d^m to wire size.

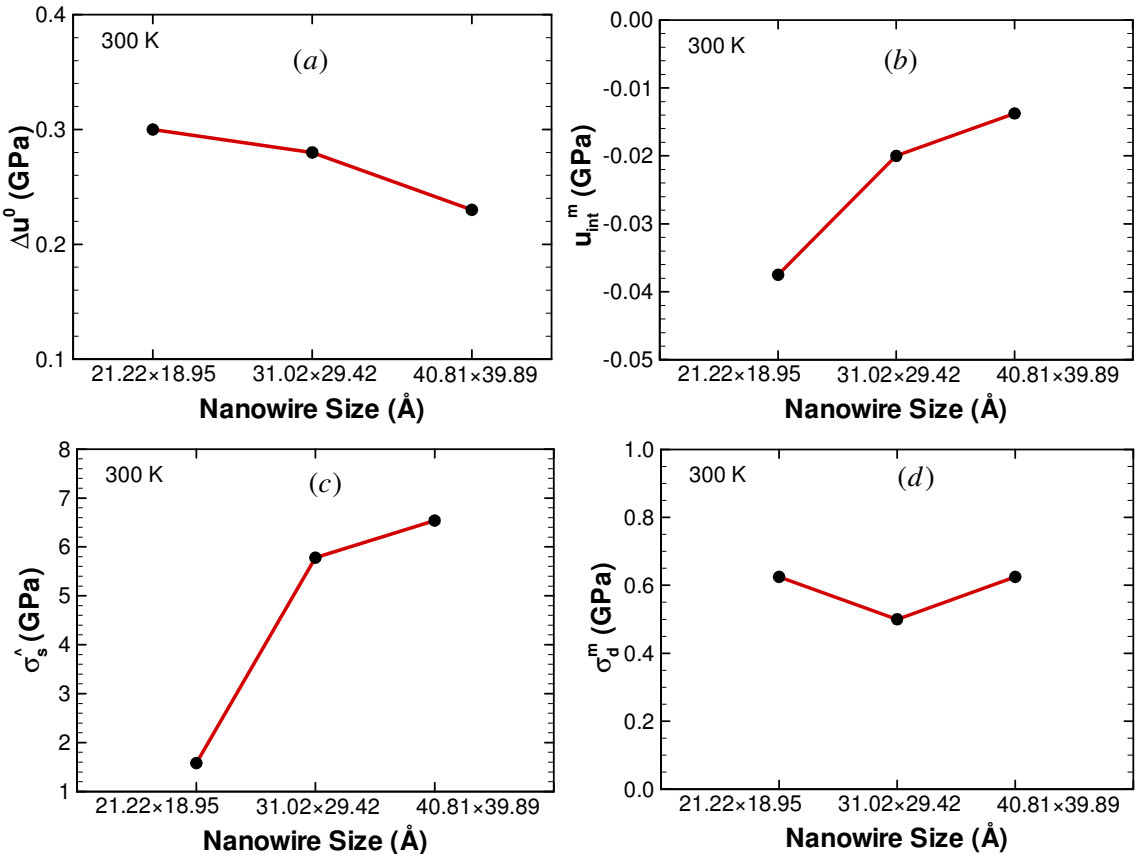

Figure 5.18 Variation of (a) formation energy difference (Δu^0) between WZ and HX structures, (b) maximum interfacial energy, (c) stress ($\hat{\sigma}_s$) and maximum stress (σ_d^m) associated with energy dissipation, with nanowire size.

The responses of a 31.02×29.42 Å wire at 100, 300 and 500 K are shown in Figure 5.19(a) (loading) and Figure 5.19(b) (unloading). There is a moderate decrease in stress at higher temperatures. This thermal softening arises from both changes in the constitutive response of the WZ and HX phases and changes in the difference between the energy barriers for the transformations and available thermal energy in the system. The first aspect can be quantified explicitly. Figure 5.19(c) and Figure 5.19(d) show, respectively, the strain energy profiles for WZ and HX at 100, 300 and 500 K. The dependence on temperature is a weak one and is more appreciable at large strains. The dependence of the formation energy densities (u_i^0) of WZ and HX on temperature over

the range of 100 to 500 K is shown in Figure 5.20(a). While the actual values of u_i^0 affect phase stability, the difference $\Delta u^0 = u_2^0 - u_1^0$ influences the total stress during transformation. This can be clearly seen in the term $(u_2 - u_1)\partial f / \partial \varepsilon$ (Figure 5.14) which depends on Δu^0. For the 31.02×29.42 Å wire, Δu^0 is only weakly temperature-dependent, suggesting that it is not the primary source of the temperature dependence of the transformation stress.

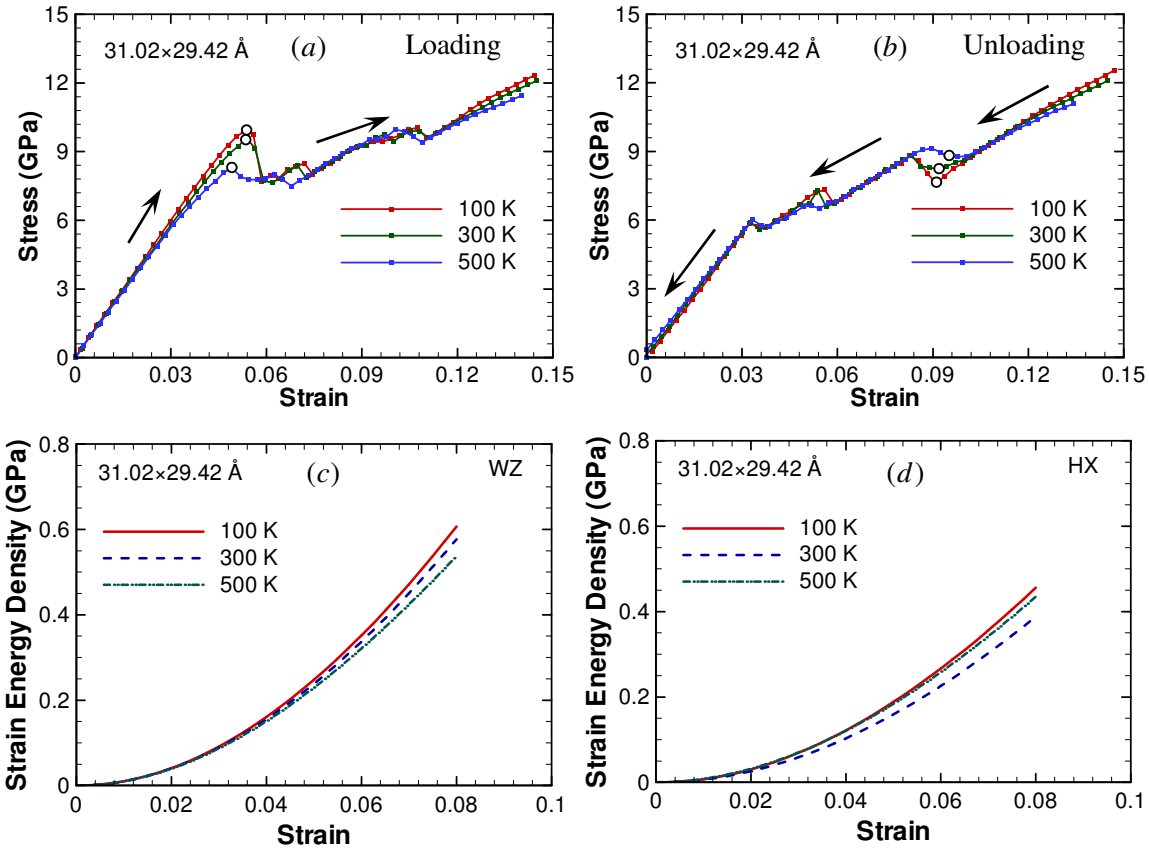

Figure 5.19 Temperature dependence of response. (a) Loading and (b) unloading response of 31.02×29.42 Å wire, (c) strain energy function for WZ structure and (d) strain energy functions for HX structure, at 100, 300 and 500 K.

The dependence of the transformation stress on temperature arises primarily out of the dissipative part of the transformation process, as can be seen from the maximum

stress associated with dissipation (σ_d^m) which shows a clear dependence on temperature [Figure 5.20(b)]. Obviously, σ_d^m decreases as higher thermal energy levels at higher temperatures reduce the mechanical work required to the barriers for interface propagation both during loading and unloading.

Finally, it is worth noting that the maximum interfacial energy (u_{int}^m) is rather constant over the temperature range analyzed, suggesting that the interface does not contribute significantly to the temperature dependence of the pseudoelastic behavior of the wires and the temperature effect primarily comes from the bulk processes already discussed.

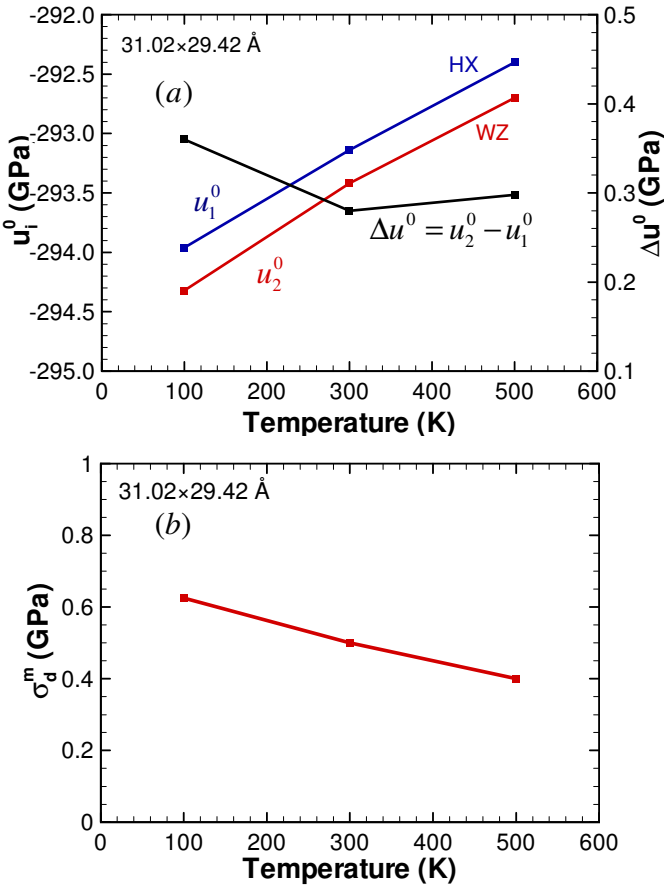

Figure 5.20 (a) Change in formation energy densities (u_i^0) of WZ and HX structures and their difference (Δu^0), and (b) increase in maximum stress associated with dissipation (σ_d^m), as the temperature is increased from 100 to 500 K.

5.5 Pseudoelasticity without Shape Memory

The pseudoelastic behavior quantified here is reminiscent of a very similar pseudoelastic behavior [which leads to a novel shape memory effect] in FCC metal nanowires discovered and analyzed by Liang and Zhou (2006). This similarity in the pseudoelastic behaviors between nanowires of the two classes of materials naturally raises the question of if a similar SME also exists in the ZnO nanowires analyzed here. To answer this question, we first note that the pseudoelasticity and the SME in the FCC metal nanowires are driven primarily by a surface-stress-induced lattice reorientation process which requires the formation of intermediate transitional structures involving partial dislocations. One attribute of that unique lattice reorientation process is that an energy barrier exists between the phases even at very low temperatures. Therefore, spontaneous relaxation occurs only at temperatures above a critical value. It is this temperature dependence that gives rise to the SME in the FCC metal wires.

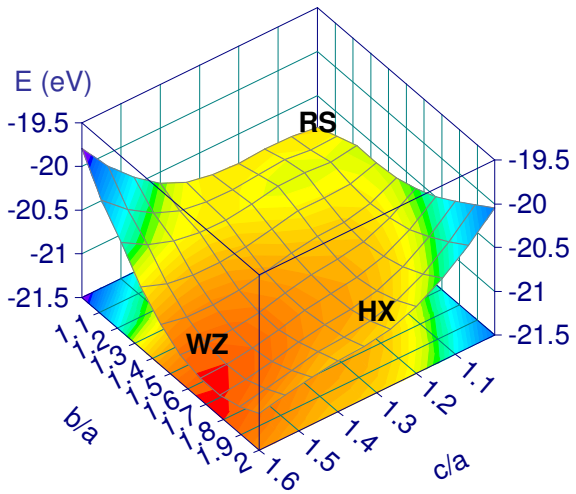

Figure 5.21 Potential energy map of ZnO with highlights of the WZ, RS and HX lattice structures.

To ascertain if a SME exists in the ZnO nanowires analyzed here, partially and fully transformed wires were cooled to various final temperatures, the lowest being 10 K. Subsequently, unloading is carried out at the low temperatures to determine if the HX

phase can be retained without external stress. For all wire sizes considered and under all initial/final temperature combinations analyzed, the wires reverted fully back to the WZ structure. This result shows that there is no critical temperature below which either partially or fully HX-structured wires can exist without external loading. The absence of such a critical temperature and the lack of a HX structure at zero loading effectively rule out the possibility of a SME in the ZnO nanowires. This finding can be explained by the enthalpy surface for ZnO at 0 K and zero external loading. Figure 5.21 shows the potential energy profile of one ZnO unit cell at different structural configurations (when there is no external loading, the enthalpy is equal to the potential energy) obtained through first principle calculations. Lattice structures corresponding to WZ, RS and HX are labeled in this figure. Note that only two local minima (energy wells) exist, one at the WZ structure and the other at the RS structure. A well is not seen at the HX structure. Obviously, WZ is the stable phase and any sample with the HX structure would spontaneously transform into the WZ structure. On the other hand, the RS structure is a metastable phase which may exist if temperature and load histories are carefully controlled. In contrast, it is not possible for HX to exist without loading since no energy well is seen for it on the energy surface. Of course, the enthalpy surface can be modified by appropriate external loading to include a local minimum (well) at the HX structure. Tensile loading of sufficient magnitude along the b-direction is such an example and has been shown to cause the WZ→HX phase transformation (Kulkarni et al. 2006).

Crystallographically, the two-way WZ↔HX transformation occurs through smooth lattice structure evolution without the formation of defects or intermediate structures. In particular, the process can be illustrated by a look at the buckling and unbuckling of the [0001] Zn and O basal planes. Figure 5.22 shows the evolution of the 3-D O-Zn-O bond angle (α) at various stages of deformation. The strain values are associated with the loading process of the 40.81×39.89 Å wire. The evolution of α during unloading is very similar except that the corresponding wire strain values are

slightly different. For a perfect, undeformed WZ lattice, $\alpha \approx 108.2^{\circ}$ [Figure 5.22(a)]. As deformation progresses, α increases as loading is increased and the structure evolves [Figure 5.22(b) and Figure 5.22(c)]. Upon full WZ→HX transformation, the basal planes flatten out and α becomes 120° [Figure 5.22(d)], at the same time, a new bond is formed along the [0001] axis [Figure 4.4]. During unloading, the reverse process is seen, with α decreasing as the load is decreased. The lack of defect or intermediate structure formation in the process makes ZnO nanowires different from FCC metal nanowires such that the energy requirement for the nucleation of the WZ↔HX transformation is very low. Therefore, during the actual unloading of a HX wire, the barrier for the HX→WZ transformation is primarily due to the breaking of the additional [0001] bond formed during the forward transformation. This barrier is relatively small and is easily overcome by the strain energy stored in the HX structure (Kulkarni et al. 2006). Consequently, spontaneous HZ→WZ transformation occurs at all temperatures and no SME is observed in the ZnO nanowires.

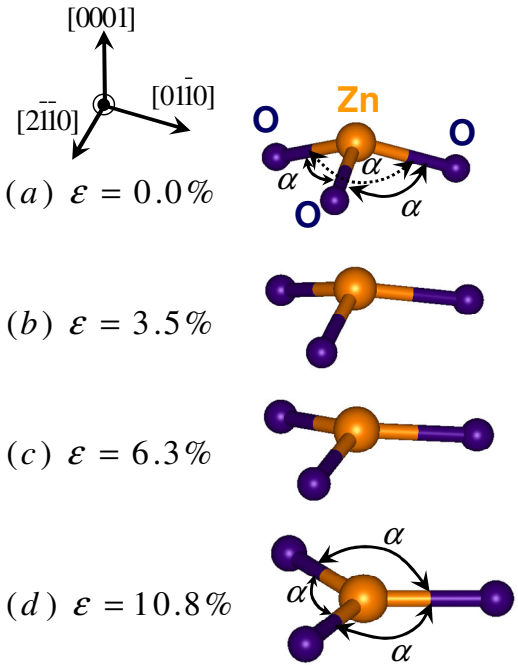

Figure 5.22 Increase in the O-Zn-O bond angle (α) between Zn and O atoms on [0001] basal planes at various levels of strain during tensile loading along the [01$\bar{1}$0] wire axis.

5.6 Chapter Summary and Insights

A novel pseudoelastic behavior discovered in $[01\bar{1}0]$-oriented ZnO nanowires over the temperature range of 100-700 K has been characterized. MD simulations of the uniaxial tensile loading and unloading of nanowires with lateral dimensions between 19 and 41 Å show that this behavior results from the unique structural transformation from WZ to a previously unknown phase (HX). The transformation is fully reversible upon unloading with recoverable strains up to 16%. The hysteretic dissipation associated with a loading-unloading cycle is 0.05-0.14 GJm^{-3} and this value is significantly lower then the value for the reversible WZ-RS transformation in ZnO. Significant temperature- and size-dependence of the pseudoelastic response is observed. In particular, the critical stress for the nucleation of the HX phase and the maximum recoverable strain decreases as temperature increases. In addition, the critical stress is lower at smaller wire sizes. Extensive surface reconstructions that minimize surface charge polarity and surface energy contribute to these temperature- and size-effects.

A continuum model is developed to capture this novel pseudoelastic behavior. Based on the first law of thermodynamics, the model splits the behavior into a reversible process of evolution of phase equilibrium states and an irreversible process of energy dissipation. Expressions are developed for the internal energy of the wires and the dissipation. Constrained energy minimization is carried out to determine the stress associated with the equilibrium process and a phenomenological model is proposed for the dissipative stress. The macroscopic stress during loading and unloading is expressed as a combination of the conservative and dissipative stress contributions established through thermodynamic considerations. Model predictions for three wire sizes (21.22×18.95, 31.02×29.42 and 40.81×39.89 Å) at 100, 300 and 500 K are seen to agree excellently with MD results. The size dependence of wire response is observed to originate from the surface-to-volume ratio dependence of the elastic behavior as seen

from the strain energy profiles of the two phases. Phenomenologically, the model captures the size effect through the variation in interfacial energy and phase equilibrium stress with nanowire size. Temperature effect on the pseudoelastic response is primarily due to variation in the dissipative stress. Specifically, the maximum dissipative stress decreases as the temperature is increased and consequently, the macroscopic stress and the hysteretic dissipation decrease at higher temperatures.

Unlike the pseudoelasticity in FCC metal nanowires, which underlies a novel shape memory effect, the pseudoelasticity in the ZnO nanowires analyzed here does not lead to a SME. The primary reason for this lack of a SME is the absence of an energy barrier between the WZ and the HX lattice structures when no external loading is applied. The absence of an energy barrier between WZ and HX at zero stress can be regarded as a consequence of the smooth and continuous nature of the crystallographic transition which does not require the formation of defects such as dislocations and twin boundaries. The result is that stretched HX ZnO nanowires can spontaneously revert back to the WZ state at any temperature.

CHAPTER 6 : THERMAL RESPONSE

ZnO nanowires and nanorods show unique properties sometimes unattainable in bulk. Unlike at the macroscale where the effect of surfaces on material response is negligible due to very low surface-to-volume ratios, surfaces play a dominant role in altering the thermal behavior at the nanoscale. It has been observed that the thermal conductivity of nanostructures is up to two orders of magnitude lower than what it is in bulk primarily due to the surface scattering of phonons (Volz and Chen 1999b; Kim et al. 2001; Li et al. 2003; Shi et al. 2004). Also, properties such as thermal conductivity, elastic moduli and fracture strains often regarded as constants at higher scales display dimensional dependence owing to the high surface-to-volume ratios at the nanoscale. A great challenge and perhaps also an opportunity in regulating such properties for device integration is this dependence on size at the nanoscale. Characterization of the thermal response and its variations with size is therefore important. Most thermal analyses at the nanoscale concern single-element systems whose heat transfer characteristics are primarily dominated by acoustic phonon interactions(Jund and Jullien 1999; Volz and Chen 1999b; Kim et al. 2001; Schelling et al. 2002; Li et al. 2003; Shi et al. 2004). However, in compounds like ZnO higher frequency acoustic and optical phonon interactions can play significant roles, especially at higher temperatures. So far, the effects of such phonon interactions have not been systematically characterized and little quantification is available, especially at the nanoscale.

Furthermore, in semiconductors such as ZnO, thermal conductivity is significantly affected by lattice structure and distortions. Transitions in thermal conductivity and the coefficient of thermal expansion under pressure have been reported for the quartz-coesite, olivine-γ-spinel, coesite-stishovite transformations in minerals (Jeanloz and Roufosse 1982; Roufosse and Jeanloz 1983; Andersson 1985; Slack and

Ross 1985). It has also been shown that the thermoelectric properties of bulk antimony bismuth telluride can be tuned and optimized through applied pressure (Polvani et al. 2001). Although thermal transport at the macro- and nano-scales is well characterized, the effect of stress on the thermal response of nanostructures has not been extensively studied. In particular, for nanowires, this coupling between the mechanical and thermal responses provides a mechanism for tuning and increasing the thermal conductivity through the application of mechanical input. As a result, characterization of the variation in thermal conductivity with structural distortions is imperative for nanowires where the thermal conductivities are 1-2 orders of magnitude lower than corresponding bulk values, (Volz and Chen 1999b; Walkauskas et al. 1999; Lu et al. 2002; Cahill et al. 2003; Li et al. 2003; Lu et al. 2003; Shi et al. 2004; Kulkarni and Zhou 2006b, 2006a). The characterization of the thermal response as a function of strain considered here is important since axial elongation is one of the most relevant modes of deformation for slender 1D nanomaterials.

This chapter focuses on characterizing the thermal response of the nanowires using the Green-Kubo formalism in a MD framework. Two aspects are studied: (1) effect of high surface-to-volume ratios of the nanowires on their thermal response and (2) evolution of thermal conductivity with applied strain. Specifically, the thermal conductivity of $[01\bar{1}0]$-oriented ZnO nanowires with lateral dimensions of 19-41 Å over the temperature range of 500-1500 K (melting temperature of ZnO: 2250 K) is quantified. A model based on the equation for phonon radiative transport theory (Majumdar 1993; Lu et al. 2002) is used to determine the contributions of different scattering mechanisms. Subsequently, the effect of novel reversible phase transformation from WZ to HX on the thermal conductivity of such nanowires is characterized. The analysis focuses on variations in thermal conductivity during the elastic stretching of the initial WZ-structured wire, the phase transformation into the HX structure, and upon completion of phase transformation.

6.1 Variation in Thermal Conductivity with Size

6.1.1 Effect of surface scattering of phonons

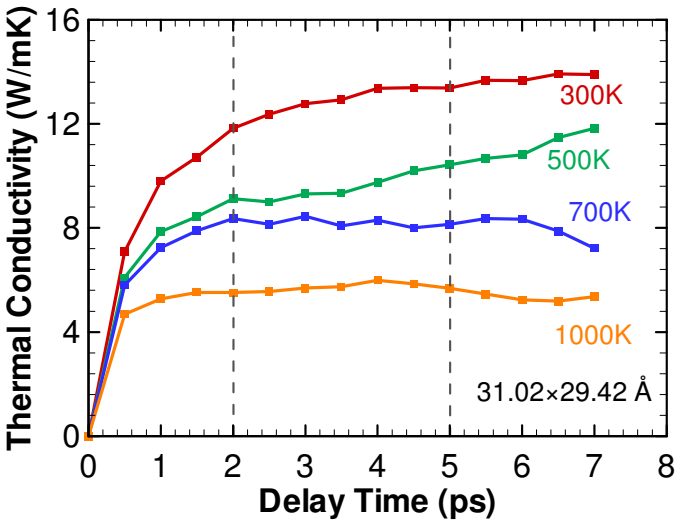

Figure 6.1 Thermal conductivity of a 31.02×29.42 Å wire as a function of delay time at temperatures between 300-1000 K.

In the Green-Kubo framework, calculation of thermal conductivity according to Eq. (3.4) theoretically allows for the infinite time required for a system to attain thermal equilibrium. However, to calculate thermal conductivity in a realistic manner, the calculation is truncated after a certain time period which is defined as the delay time τ_m. The thermal conductivity of the nanowires is therefore calculated as a function of delay time. Figure 6.1 shows the variation of the calculated values for a 31.02×29.42 Å wire. In the responses shown, short delay times ($\tau_m < 2\ ps$) correspond to only very small temperature changes associated with thermal conduction, thus limiting the accuracy of the calculation and allowing random heat fluctuations to significantly affect the evaluation. The increasing trend of calculated conductivity values for this regime of delay time in Figure 6.1 reflects this inaccuracy. On the other hand, long delay times ($\tau_m > 5$ *ps*) reduce the number of time origins available for averaging since the simulation time

window is finite, causing statistical errors to increase. Because of the above factors, the intermediate delay time regime of $2 < \tau_m < 5\ ps$ is found to give a good balance between the different constraints. The profiles in Figure 6.1 show a plateau of relative constant calculation results in this regime. The average value over this regime is taken as the thermal conductivity of the nanowires for the conditions analyzed.

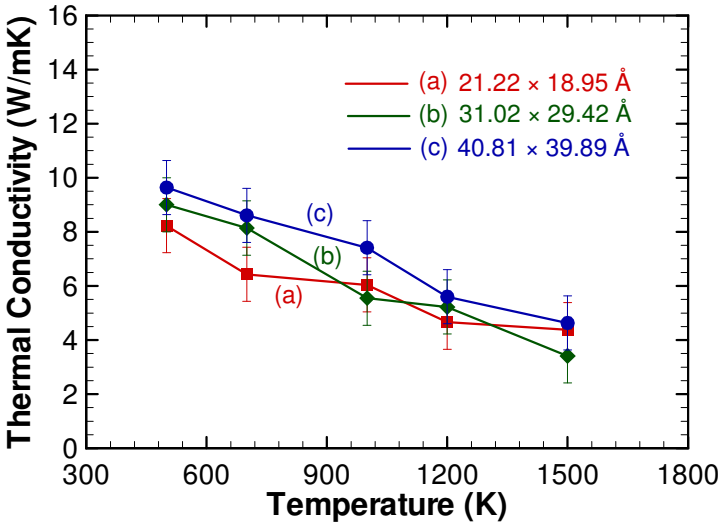

Figure 6.2 Thermal conductivity as a function of lateral size and temperature.

Figure 6.2 shows thermal conductivity as a function of temperature for the wires analyzed. The values (3-10 W/mK) are an order of magnitude lower than that for bulk ZnO (~100 W/mK) (Wolf and Martin 1973). Also, over 500-1500 K, the conductivity of the 21.22×18.95 Å wire is approximately 8-0.5% lower than that of the 31.02×29.42 Å wire and the conductivity of the 31.02×29.42 Å wire is approximately 6-5% lower than that of the 40.81×39.89 Å wire. This significant difference is primarily associated with the high surface-to-volume ratios of the nanowires. Specifically, the relatively large fractions of surface atoms enhance surface scattering of phonons and decrease the phonon mean free path, resulting in lower conductivity which is proportional to the mean free

path. The kinetic theory of fluids relates thermal conductivity k to the phonon mean free path Λ through

$$k = \frac{1}{3} C_v v \Lambda , \tag{6.1}$$

where C_v is specific heat and v is the velocity of heat carriers (for ZnO, the heat carriers are phonons and hence v represents the average phonon group velocity). Obviously, thermal conductivity is approximately proportional to the mean free path.

Surface attributes also affect heat transfer. For the nanowires, the interlayer spacings between the two outermost layers of (0001) and $(2\bar{1}\bar{1}0)$ planes decrease by 73% and 9%, respectively, relative to the values for bulk ZnO, resulting in higher atomic densities in the surfaces as shown in Figure 4.1. Such a deviation from perfect core atomic arrangement alters the surface scattering of phonons and lowers the conductivity. Boundary scattering is also influenced by surface specularity (probability of specular phonon reflection). Under conditions that phonon-phonon and phonon-defect interactions are negligible, the phonon mean free path can be expressed as (Zou and Balandin 2001)

$$\Lambda = \frac{d}{(1-p)} , \tag{6.2}$$

where p is the probability of specular scattering (which is a function of surface roughness and temperature) and d is the effective size of the nanowire. For a body with perfectly specular (atomistically smooth) surfaces, $p = 1$, consequently the mean free path and hence the thermal conductivity are not affected by boundary scattering. On the other hand, for a body with perfectly diffuse surfaces, $p = 0$, consequently the mean free path is equal to the size of the nanowire i.e., $\Lambda = d$. In the nanowires, the specularity value is between the limiting cases ($0 < p < 1$) and depends significantly on the surface attributes. Surface reconstructions discussed earlier modify surface atomic arrangement (Figure 4.1), alter the surface scattering behavior of phonons, and reduce the specularity. Also, as shown by Berman *et al.* (Berman et al. 1955), surface specularity decreases as an inverse

power of temperature, especially at higher temperatures. Consequently, the nanowire surfaces are never perfectly specular and the mean free path is limited by the lateral dimensions of the wires. To state differently, the mean free path in the nanowires is much smaller than that in bulk materials, effectively causing the observed size effect in thermal conductivity. In bulk materials, the characteristic length is much larger and the effect of boundary scattering of phonons is negligible, resulting in larger mean free paths and much higher conductivity values.

Figure 6.2 also shows the decrease in thermal conductivity with temperature. Between 500 and 1500 K, decreases of about 52% are observed. This effect is attributed to thermal softening and higher frequency phonon interactions at higher temperatures. The lower elastic stiffness of lattices at higher temperatures (which results from the nonlinearity of interatomic interactions) correspond to lower average phonon group velocities and lower levels of heat flux (see Figure 6.3). Also at higher temperatures, higher frequency acoustic and optical phonon interactions become appreciable, leading to smaller mean free path and lower conductivity values (Joshi et al. 1970). The decrease in specularity is also partly responsible for decreases in thermal conductivity over the temperature range analyzed, as discussed earlier.

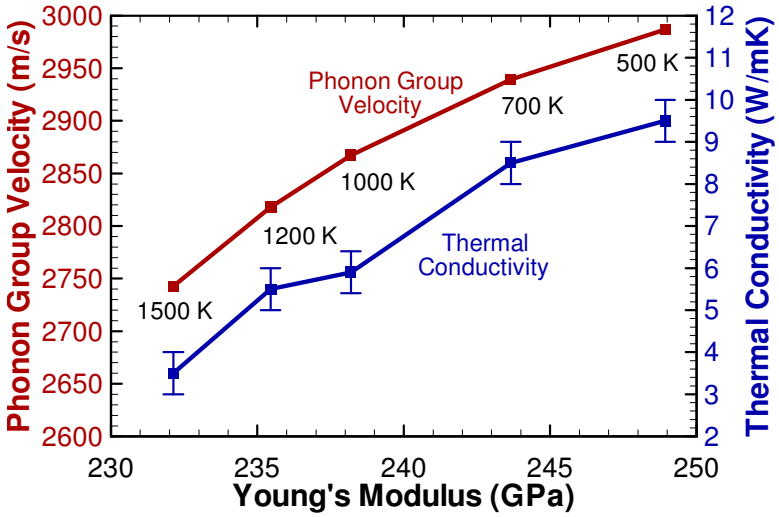

Figure 6.3 Average phonon group velocity and thermal conductivity of the 31.02×29.42 wire as functionals of its Young's modulus.

6.1.2 Equation for phonon radiative transport

Heat transport in semiconducting and insulating materials has predominantly been modeled using the Boltzmann Transport Equation (BTE) with a Bose-Einstein distribution for phonons (Ziman 1960). A new approach was developed by Majumdar (Majumdar 1993) by treating phonon dominated thermal behavior as radiative heat transfer. This approach has been further extended to the study of nanowires by Lu et al. (2002) to account for phonon behavior in nanostructures. The modifications include the boundary conditions in the solution of EPRT as well as the incorporation of a boundary scattering term in the expression for the relaxation time. In the present work, this EPRT model has been extended to fit the thermal conductivity data obtained for ZnO wires through MD simulations.

The size and temperature effects observed in the thermal conductivity of the nanowires can therefore be quantitatively delineated the EPRT model for thermal conductivity expressed as

$$\kappa(T,d) = \frac{k_B}{2\pi^2 v}\left(\frac{k_B T}{\hbar}\right)^3 \int_0^{\theta_D/T} \frac{x^4 e^x}{\left(e^x - 1\right)^2} \tau(T,x) G(\eta)\, dx \tag{6.3}$$

where $x = h\omega / k_B T$, ω is phonon frequency, v is phonon group velocity, $\hbar$ is Planck's constant, $\eta = d/\Lambda(x)$, d is the lateral dimension of the nanowire, Λ is phonon mean free path and τ is relaxation time. $G(\eta)$ accounts for the effect of surfaces which gives rise to the size dependence discussed here. This term tends to unity as the lateral size approaches infinity and Eq. (6.3) reduces to that for bulk materials. The relaxation time τ is calculated using Matthiessien's rule, accounting for contributions from boundary, three-phonon (Normal and Umklapp), and four-phonon scattering as

$$\frac{1}{\tau} = \frac{1}{\tau_{Umklapp}} + \frac{1}{\tau_{Normal}} + \frac{1}{\tau_{Boundary}} + \frac{1}{\tau_{Four\ phonon}} \tag{6.4}$$

where the individual components are expressed as:

$$\frac{1}{\tau_{Boundary}} = \frac{(1-p)v}{d} \tag{6.5}$$

$$\frac{1}{\tau_{Umklapp}} = B_1 e^{\left(-\theta_D/aT\right)} T\omega^2 \tag{6.6}$$

$$\frac{1}{\tau_{Normal}} = B_2 T\omega^2 \tag{6.7}$$

$$\frac{1}{\tau_{Four\ Phonon}} = ET^2\omega^2 \tag{6.8}$$

where p is the probability of specular scattering, B_1, B_2 and E are constants fitted to bulk properties. The boundary term [Eq. (6.5)] accounts for phonon-surface scattering events while the three phonon [Eqs. (6.6) and (6.7)] and four phonon [Eq. (6.8)] terms account for phonon-phonon interactions. The parameters in the model (specularity and four-phonon relaxation time) are determined by fitting Eq. (6.3) to the results from MD simulations. Constants related to three-phonon relaxation time are determined from experimental data for bulk ZnO in Wolf and Martin (1973). The boundary scattering length in bulk is taken as the Casimir limit in bulk crystal for which the conductivity was experimentally measured (Wolf and Martin 1973).

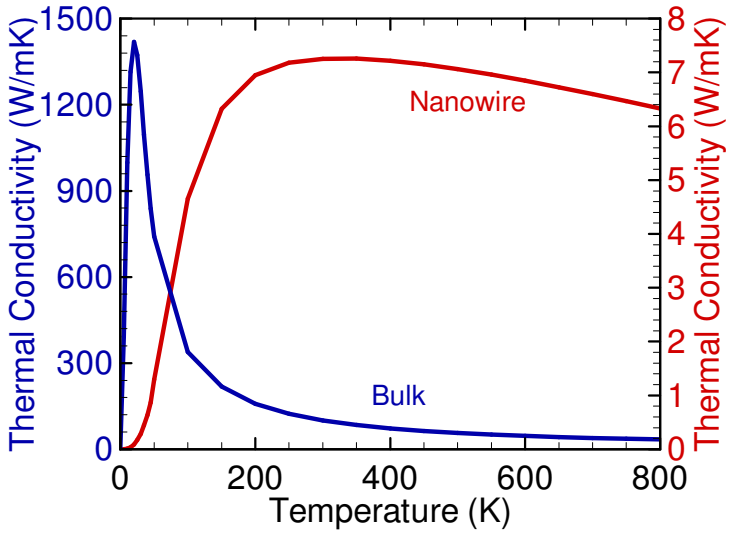

Figure 6.4 EPRT predictions for bulk and nanowire structures.

Figure 6.4 shows the model predictions for bulk and nanowires structures. It can be seen from the figure that for lower temperature, the conductivity of nanowires is an order of magnitude lower than bulk. At very high temperatures, however, the three- and four-phonon processes dominate and the conductivity of the bulk decreases rapidly. However, the conductivity of the nanowire is always lower than bulk due to the influence of boundary scattering.

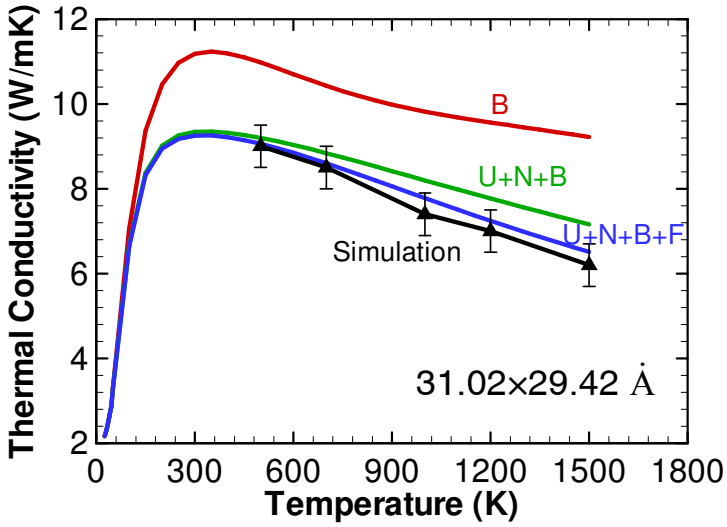

Figure 6.5 Effects of different scattering mechanisms on the thermal conductivity of the 31.02×29.42 Å nanowire as predicted by EPRT.

Figure 6.5 shows the results for the 31.02×29.42 Å wire for cases that account for boundary scattering (B), boundary and three-phonon (Normal and Umklapp) scattering (B+N+U), and boundary, three- and four-phonon scattering (B+N+U+F) processes. Over 500-1500 K, boundary scattering is the most dominant process responsible for ~80-47% decrease in conductivity from the bulk value. A further decrease of ~3-11% is attributed to three-phonon interactions and another decrease of ~3-15% is due to four-phonon interactions. At lower temperatures boundary scattering dominates, while above 600 K the three-phonon and four-phonon terms have to be included. The primary reason is that at higher temperatures, the vibration amplitude of atoms becomes sufficiently large so

that the effect of three- and four-phonon processes emerges as a significant factor. Figure 6.6 shows EPRT predictions for the three nanowires sizes in the 500-1500 K temperature range. The model developed accounts for size and temperature effects through the boundary scattering mechanism and thermal softening and therefore is able to predict the size and temperature dependence of thermal conductivity very well.

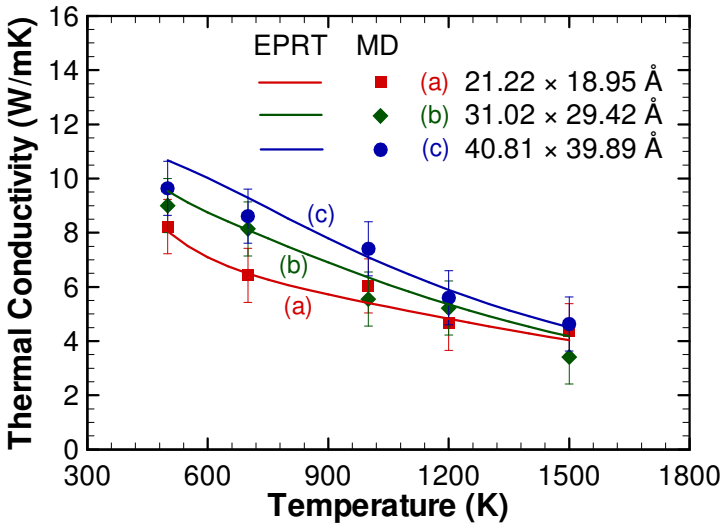

Figure 6.6 EPRT predictions of the thermal conductivity as a function of lateral size and temperature.

6.2 Variation in Thermal Conductivity with Applied Loading

The variation in the conductivity values with applied strain is analyzed using the Green-Kubo framework. In the computational scheme, the conductivity calculations are carried out at the end of the equilibration stage of a relevant strain increment when a steady state has been achieved during loading of the nanowires.

6.2.1 Effect of elastic nonlinearity and phase transformation

Figure 6.7 shows stress and thermal conductivity as functions of strain for a 31.02×29.42 Å wire at 500 K. Three distinct stages of deformation can be identified from the stress-strain response: (1) elastic stretching of the defect-free WZ-structured wire (A-B), (2) transformation from WZ to HX (B-C) and (3) elastic stretching of the defect-free

HX-structured wire (C-D) after completion of transformation (Kulkarni et al. 2006; Kulkarni et al. 2007a).

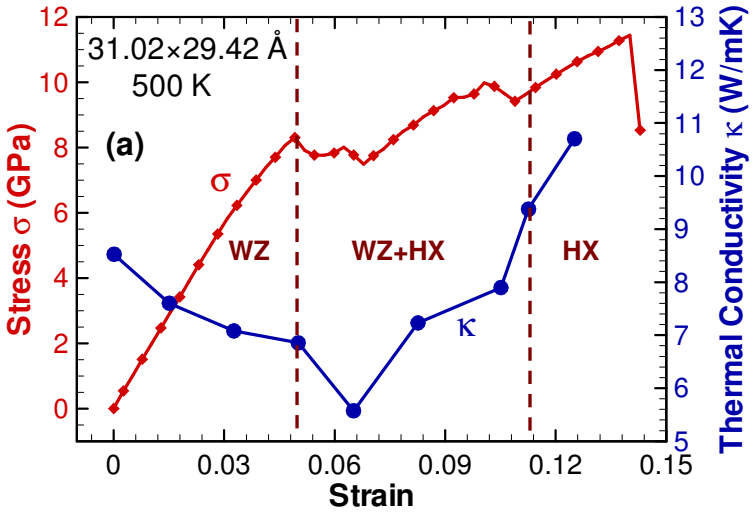

Figure 6.7 Stress and thermal conductivity as functions of applied strain for a 31.02×29.42 Å under tensile loading at 500 K.

6.2.1.1 WZ-structured wire prior to initiation of phase transformation

The thermal conductivity (κ) of a unstressed 31.02×29.42 Å nanowire at 500 K is 8.52 W/mK, an order of magnitude lower than that for bulk ZnO. As previously discussed, this significant difference is primarily associated with the high surface-to-volume ratios of the nanowires. Specifically, decrease in the phonon mean free path due to boundary scattering results in lower conductivity values (Kulkarni and Zhou 2006b, 2006a).

As deformation progresses, κ decreases from its initial value of 8.52 W/mK by 19.6% as strain increases to 0.049. During this stage, the nanowire is fully within the WZ structure and the decrease in κ is primarily due to the nonlinear elastic behavior of WZ along the $[01\bar{1}0]$ orientation, although the increase in lattice anharmonicity at finite values of strain also has a contribution (Picu et al. 2003). The nonlinear elastic response can be quantified through the rate of change of the uniaxial modulus

$$E' = \frac{d^2\sigma}{d\varepsilon^2} = \frac{1}{V}\frac{d^3U}{d\varepsilon^3}, \tag{6.9}$$

where V is the initial volume of the wire, U is the strain energy, σ and ε are, respectively, the stress and strain along the wire. For the $[01\bar{1}0]$ nanowire analyzed, $E' = -1428.7$ GPa and the modulus E decreases by 35% up to the strain at transformation initiation ($\varepsilon = 0.049$). The elastic stretching also causes the volume of the wire to increase and the mass density ρ to decrease. Both changes combine to cause the stress wave speed $\bar{v}$ ($= \sqrt{E/\rho}$) to decrease by 18.9%. Additionally, the decrease in density along with the lattice distortion increases lattice anharmonicity and, consequently, causes the mean free path (Λ) of the phonons to decrease. At temperatures above the Debye temperature, the kinetic theory of fluids relates thermal conductivity to phonon mean free path through Eq. (6.1). Obviously, the conductivity decreases as the WZ-structured nanowire is stretched.

6.2.1.2 WZ/HX-structured wire during phase transformation

Upon the initiation of phase transformation at $\varepsilon = 0.049$, the stress drops precipitously, reflecting a relaxation of the wire structure. Figure 6.8 shows the configurations of the wire at $\varepsilon = 0.065$, 0.083, and 0.105. Three zones, corresponding to WZ, HX and a transitional interface between the two phases, are seen. The nucleation of HX is at the surfaces. The atomic structure on the $(2\bar{1}\bar{1}0)$ plane in the interfacial region is shown in Figure 6.9. Obviously, the interface is coherent and the orientation relationships are maintained in both phases across the interface. The fractions of atoms in the HX, WZ and interfacial regions are shown in Figure 6.9 as functions of strain.

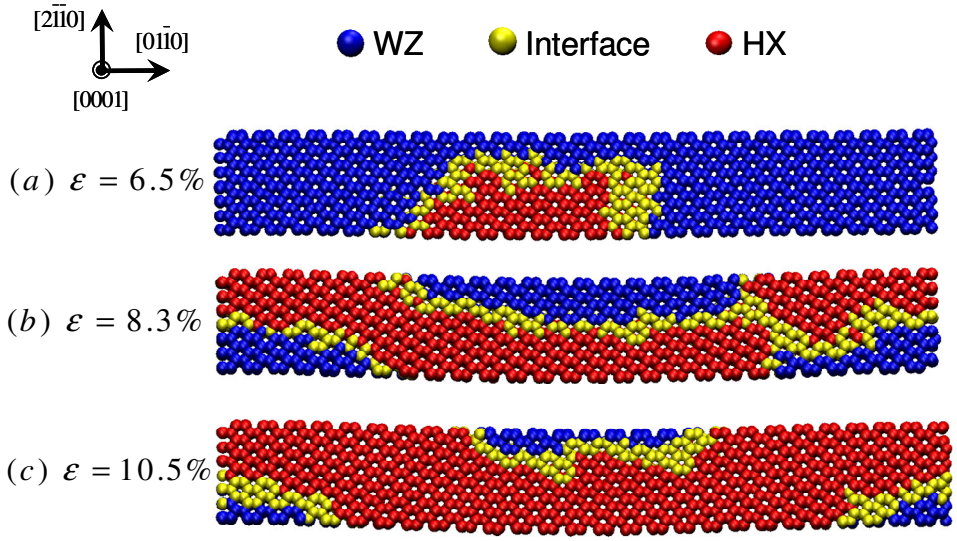

Figure 6.8 WZ, HX and interface regions in a 31.02×29.42 Å wire at (a) $\varepsilon = 6.5\%$, (b) $\varepsilon = 8.3\%$ and (c) $\varepsilon = 10.5\%$.

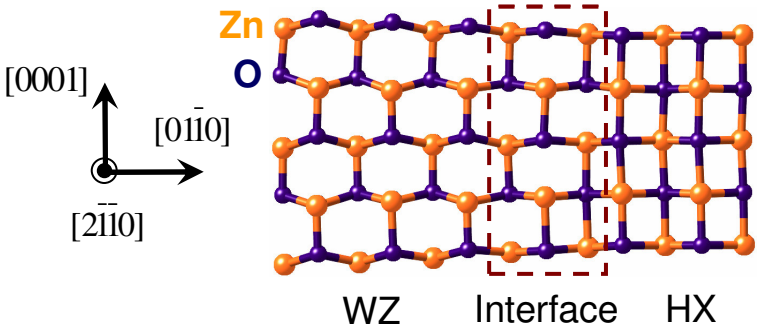

Figure 6.9 Arrangement of atoms on a $(2\bar{1}\bar{1}0)$ plane across an interfacial region.

Initially ($0.049 < \varepsilon < 0.072$, strain range from transformation initiation to the formation of largest interface fraction), the fraction of the HX phase is lower than that of the WZ phase and the thermal response is dominated by the conductivity of the WZ phase and the thermal resistance of the interface. In this stage, κ decreases by 18.7% from 6.86 to 5.58 W/mK as the strain increases from 0.049 to 0.072. This decrease is due to the low thermal transmission coefficient of the interface and enhanced phonon scattering due to (1) discontinuities in lattice across the interface and (2) lattice distortion

associated with the elastic strain field near the interface (Klemens 1954, 1994). Note that over this strain interval the fraction of interfacial atoms increases from 0.12 to a maximum of 0.19. Since the interfacial thermal resistance is proportional to the area of interfaces (quantified here through the fraction of interfacial atoms), κ decreases as strain increases. Continuation of loading beyond $\varepsilon = 0.072$ causes the fraction of HX to exceed that of WZ [Figure 6.8 and Figure 6.10], resulting in the overall thermal response of the wire to be dominated by the HX phase. At the completion of the WZ→HX transformation ($\varepsilon = 0.113$), the conductivity of the HX-structured wire is 9.4 W/mK or 68.3% higher than the lowest value of 5.58 W/mK at $\varepsilon =$ 0.072. This increase in κ is due to several factors, including (1) the higher thermal conductivity of the HX phase (details later), (2) significant decrease (43.3%) in the fraction of interface atoms as the strain increases from 0.072 to 0.113 and (3) the alignment of the interfaces along the direction of heat flow (wire axis) as deformation progresses (Figure 6.8). Arising primarily from bonding state non-uniformity and lattice strains, interfacial thermal resistance is expected to be much lower for directions parallel to an interface than that for the direction perpendicular to it.

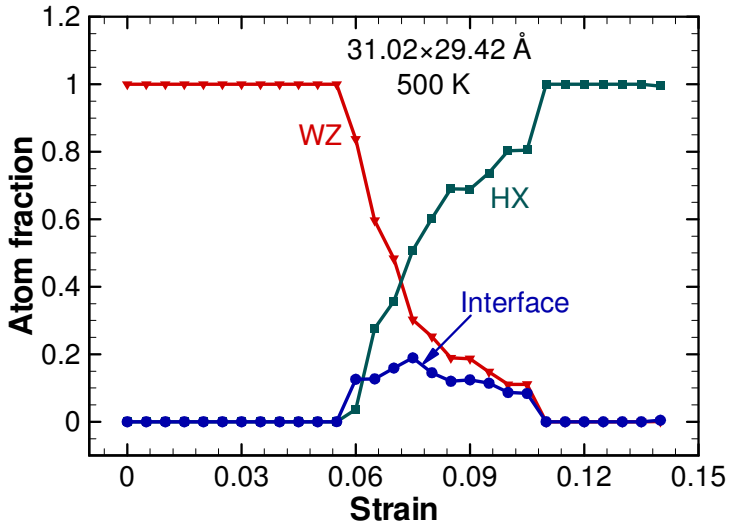

Figure 6.10 Fractions of atoms in WZ, HX and interface regions as functions of strain for a 31.02×29.42 Å wire.

6.2.1.2 HX-structured wire after transformation

The WZ→HX transformation completes at a strain of $\varepsilon = 0.113$. At this stage, some point defects exist due to local variations in the lattices. Further loading causes the defects to disappear, leading to a defect-free HX structure at $\varepsilon = 0.125$. The value of thermal conductivity obtained for this defect-free structure is reported as the characteristic thermal property of the HX wires. Further loading causes the conductivity to decrease, reflecting the nonlinear elastic behavior of the HX-structured wires (not shown). The thermal conductivity of the HX-structured wire in this state is 10.7 W/mK which is 25.6% higher than that of the unstressed WZ wire. Such a significant increase in κ can be qualitatively explained using a simplified model for thermal conductivity (Roufosse and Klemens 1973; Roufosse and Jeanloz 1983). At temperatures above the Debye temperature, the lattice thermal conductivity is limited by anharmonic coupling of phonons and can be expressed as [cf. (Roufosse and Klemens 1973; Roufosse and Jeanloz 1983)]

$$\kappa \approx A \frac{r\bar{v}^3}{3\gamma^2 T} \rho \quad , \tag{6.10}$$

where r is the average interatomic spacing such that the unit cell volume $V_{cell} = r^3$, $\bar{v}$ is the average wave speed, ρ is mass density, γ is the thermal Gruneisen parameter, T is temperature and A is a constant representing the contributions of changes in crystal structure (coordination, bond length, etc.) to thermal conductivity. During the WZ→HX transformation, the number of atoms per unit cell remains the same and the average bond length increases only by ~6%. Hence, the change in A is negligible and, at a given temperature, the effect of the phase transformation on thermal conductivity can be expressed through the change in density, anharmonicity of the lattice and the wave speed as

$$\frac{\kappa_{HX} - \kappa_{WZ}}{\kappa_{WZ}} \approx \left(\frac{\overline{v}_{HX}}{\overline{v}_{WZ}}\right)^3 \left(\frac{\rho_{HX}}{\rho_{WZ}}\right)\left(\frac{\gamma_{WZ}}{\gamma_{HX}}\right)^2 - 1 \tag{6.11}$$

The wave speed $\overline{v}$, calculated from the elastic moduli and densities of each of the two phases, is lower for HX than for WZ. Therefore, the change in wave speed tends to lower thermal conductivity; but this effect is only secondary. Dominant effects that cause the thermal conductivity to increase come from the higher density and higher Gruneisen parameter of HX. During the transformation, the lattice parameter along the [0001] direction (*c*) decreases considerably, causing the cell volume to decrease by 11.98% and the density of the structure to increase by 13.5%. The efficient packing of the HX structure and its higher density lead to a lower anharmonicity (lower thermal Gruneisen parameter) and, ultimately, the higher thermal conductivity (Jeanloz and Roufosse 1982). For the 31.02×29.42 Å wire, the 25.6% increase in κ implies a 27.5% decrease in γ relative to the value of 0.69 for WZ at 500 K (Gadzhiev 2003). This decrease is consistent with the increase in packing efficiency of the HX structure over the parent WZ structure. A quantitative prediction of γ is not feasible here since the model is strictly valid for bulk materials where the effect of surface scattering of phonons is negligible. Nevertheless, this model provides a qualitative explanation for the increase in conductivity observed here.

The difference in surface configurations between WZ- and HX-structured nanowires also contributes to the observed increase in thermal conductivity. To illustrate this issue, Figure 6.11(a) and Figure 6.11(b) show the positions of atoms on layers perpendicular to the [0001] direction for bulk WZ and a WZ-structured wire, respectively, and Figure 6.11(c) shows the configuration of a HX-structured nanowire.

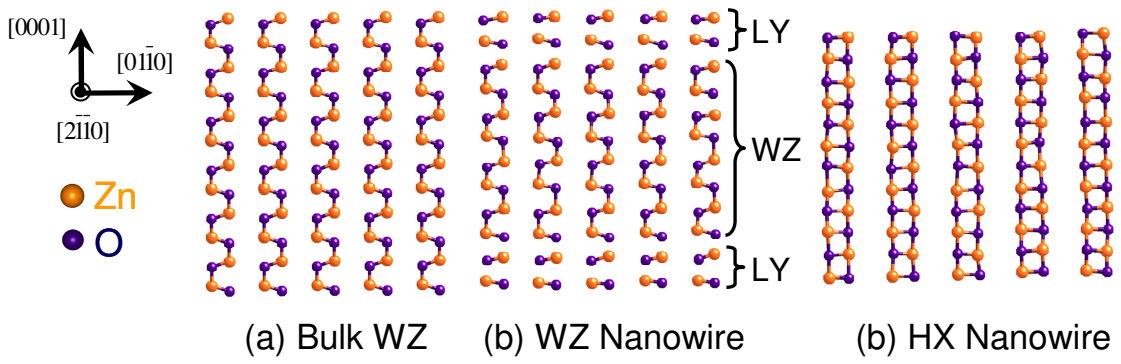

Figure 6.11 Arrangement of atoms in the interior and on the surfaces of a 31.02×29.42 Å wire, the images correspond to (a) bulk WZ, (b) WZ-structured wire with LY-structured surfaces after initial relaxation and (c) HX-structured wire after completion of the WZ→HX transformation.

For WZ wires, the imbalance of ionic forces on the surfaces due to reduced number of neighbors and surface polarity cause extensive surface reconstruction relative to bulk WZ. Obviously, this reconstruction entails the contraction of surface layers and merging of Zn and O basal planes [Figure 6.11(a, b)], resulting in a layered surface structure (LY) which is crystallographically similar to the HX structure (Claeyssens et al. 2005; Freeman et al. 2006). Such reconstructions modify atomic arrangement on surfaces relative to the core of the nanowire and alter the surface scattering behavior of phonons, causing the surface specularity and, hence, the thermal conductivity for WZ-structured nanowire to be much lower than that for bulk WZ. In the HX-structured wire in Figure 6.11(c), the atomic arrangement on surfaces is similar to that in the core and hence the surface disorder is significantly lower than that of the WZ wire in Figure 6.11(b). As a result, the surface specularity for HX wires is much higher than that of WZ-structured nanowires. The effect of surface specularity on conductivity can be characterized through Eqs. (6.1) and (6.2). Consequently, for nanowires with the same characteristic sizes, the phonon mean free path and therefore the conductivity of the HX wires is higher than that of the WZ wires.

6.2.2 Size dependence of thermal conductivity of WZ and HX phases

The bulk and surface effects discussed above combine to give rise to significant dependence of behavior on wire size. Figure 6.12 shows the conductivity values of unstressed WZ and transformed HX wires of three different sizes. For WZ wires, the thermal conductivity is in the range of 8.3-8.6 W/mK which is an order of magnitude lower than that for bulk ZnO and decreases by 3% as the lateral size decreases from 40.81×39.89 to 21.22×18.95 Å. This trend results directly from the higher surface-to-volume ratios and smaller mean free path at the smaller sizes. A clear dependence of conductivity on size is also seen for the HX-structured wires. The WZ-to-HX transformation causes the conductivity to increase to 10.1, 10.7 and 11.1 W/mK for the 21.22×18.95, 31.02×29.42 and 40.81×39.89 Å nanowires, respectively. The 20-28% increase over the values for WZ wires is associated with the lower anharmonicity due to and the higher surface specularity of the HX wires.

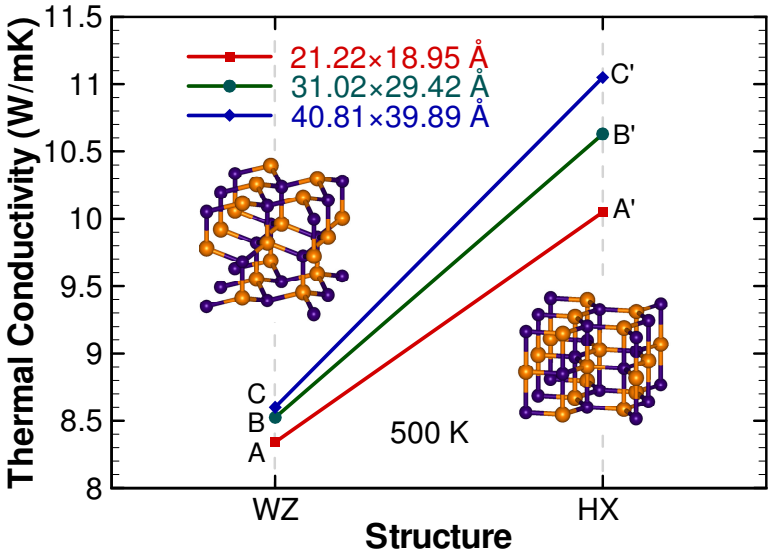

Figure 6.12 Thermal conductivity of unstressed WZ and transformed HX wires of three different sizes.

6.3 Chapter Summary and Insights

MD simulations have allowed the quantification of the effects of size and temperature on the thermal conductivity of ZnO nanowires with lateral dimensions between 21.22×18.95 and 40.81×39.89 Å. The size effects are due to the 1D structures and the high surface-to-volume ratios of the nanowires at the size scale analyzed. The mechanism giving rise to the size effect on thermal conduction is due to enhanced surface scattering of phonons which reduces the mean free paths and is affected by surface specularity. The thermal conductivity is also found to be significantly temperature-dependent over the temperature range of 500-1500 K. This dependence is due to the change of equilibrium lattice spacing with temperature and the nonlinearity of interatomic interactions. A correlation is obtained between the Young's modulus, phonon group velocity, and the thermal conductivity over the temperature range analyzed. The following characterizations have resulted from the analysis described here.

1) The thermal conductivity values for the nanowires (3-15 W/mK) are one order of magnitude lower than the corresponding value for bulk ZnO single crystal (~100 W/mK);
2) Over 500-1500 K, the conductivity of the 21.22×18.95 Å wire is approximately 31-18% lower than that of the 40.81×39.89 Å wire;
3) For the lateral sizes studied, an average decrease on the order of 52% in thermal conductivity is observed when temperature changes from 500 to 1500 K.

The thermomechanical response of $[01\bar{1}0]$-oriented ZnO nanowires under tensile loading is also quantified. Three distinct stages in the thermal and mechanical responses are observed. The mechanical response consists of (1) elastic stretching of WZ, (2) phase transformation from WZ to HX and (3) elastic stretching of HX. The thermal conductivity of the nanowires is a function of applied strain in each of the three stages. Over the size range of 18.95-40.81 Å, the elastic stretching in the WZ structure is

accompanied by 19-27% decrease in the thermal conductivity. The nonlinearity of the elastic response of the wires with lower stiffness (hence lower wave speeds) at higher strains is the origin of this effect. The formation of interfaces during the WZ-to-HX phase transformation causes the thermal conductivity to decrease by another 15-19% as the transformation progresses. Upon completion of the transformation, the thermal conductivity for the HX-structured wires are 20.5-28.5% higher than those of the corresponding WZ-structured wires. This increase in conductivity is due to the higher atomic packing density, lower anharmonic coupling of phonons and higher surface specularity of the HX wires.

Finally, the significant size-and strain-dependence of thermal conductivity analyzed here echoes a similar trend in mechanical response. Such variations in properties at the nanoscale offer potential for novel applications in NEMS that rely on thermomechanical responses.

CHAPTER 7 : CONCLUSIONS

This research focuses on the characterization of the thermal and mechanical behaviors of single crystalline ZnO nanowires. An atomistic framework for MD simulations has been developed to extract the thermomechanical responses. The characterizations involve quasi-static uniaxial loading and unloading of $[01\bar{1}0]$- and [0001]-oriented nanowires to evaluate mechanical properties and a Green-Kubo based framework to quantify the thermal response of nanowires.

Novel phase transformations to previously-unknown crystal structures for ZnO are discovered. Specifically, a graphite-like phase (HX) and a body-centered tetragonal phase (BCT-4) are observed in the $[01\bar{1}0]$ and [0001] wires, respectively, under uniaxial tensile loading using MD simulations. First-principles calculations carried out show that both phases are energetically favorable under the loading conditions prescribed. Crystallographic analysis reveals atomic arrangements and transformation paths for the two structures. HX phase is formed by the flattening of the buckled wurtzite basal plane (Zn and O atoms becoming co-planar). An additional Zn-O bond is formed along the [0001] axis and the Zn atoms are at equal distances from the O atoms along the [0001] axis. Consequently, the structure acquires the additional symmetry of a mirror plane perpendicular to the [0001] axis. The in-plane coordination of the HX structure is 3-fold and the full 3D coordination is 5-fold, compared to the 4-fold coordination in WZ. The BCT-4 structure, on the other hand, results from breaking of every other Zn-O bonds along the [0001] direction and the formation of an equal number of Zn-O bonds along the same direction next to the broken bonds. This process repeats on alternate planes along the $[01\bar{1}0]$ direction resulting in the formation of 4-atom (2 Zn and 2 O) rings arranged in a BCT lattice. The transformed structure retains the tetrahedral coordination with each Zn/O atom at the center and four O/Zn atoms are at the vertices of a tetrahedron.

The novelty of these phase lies not only in their discovery but also in the fact that such transformations have not been observed in bulk ZnO. The primary reason for the difference in bulk vs. nanowire behavior is the high surface-to-volume ratios in nanowires. Specifically, while bulk WZ-ZnO can undergo phase transformation to RS with volumetric strains up to 17% under high pressure, it is brittle in nature with maximum failure strains on the order of 0.1-0.3% under tensile loading. However, since these nanostructures are single-crystalline and nearly defect-free, they have the ability to undergo large deformations without failure under tension. Also, their high surface-to-volume ratios imply higher atomic mobility and therefore promote phase transformations under loading along certain crystalline directions. The discovery of these phases also puts into perspective the extent of polymorphism in materials such as ZnO. HX and BCT-4 constitute the fourth and fifth polymorphs of ZnO discovered so far. The identification of the BCT-4 and HX structures now leads to a more complete understanding of the nature and extent of polymorphism in ZnO and its dependence on load triaxiality

More importantly, the WZ↔HX reversible transformation results in a novel pseudoelastic behavior in the wires. Recoverable strains up to 16% are observed. This is quite extraordinary since compound semiconductors such as ZnO, GaN, InN and BN are known to be brittle under tensile loading. The recoverable strains observed consist of elastic stretching of the WZ and HX wires along with a contribution from the transformation. The energy dissipation associated with a loading-unloading cycle is 0.05-0.14 GJ/m^3, much lower than that for the WZ↔RS transformation in bulk (~1.38 GJ/m^3 with a maximum recoverable volumetric strain of 17% in compression). Significant size and temperature dependence of the critical stress for transformation nucleation, hysteretic dissipation and the recoverable strains are also observed. The variation in surface-to-volume ratio with size, thermal softening and temperature dependence of energy barrier for transformation are determined to be the origins of the size and temperature effects.

A micromechanical continuum model is developed to model this pseudoelastic behavior. The emphasis is on modeling the elastic deformations of the individual phases and the transformation response during loading and unloading. The model considers the transformation as a combination of a reversible component associated with the smooth evolutions of the phase fractions and an irreversible component due to the energy dissipation. Energy minimization with kinematic constraints specified by rule of mixture for strains determines the equilibrium values of stresses and strains in each phase and also their volume fractions. Dissipation during the transformation is due to the ruggedness of the energy landscape associated with the propagation of phase boundaries involving a sequence of unstable and stable states. The difference in energy between each of the unstable and stable states is dissipated to maintain constant temperature. The energy required to take propagate the phase boundaries increases with the size of the interface, leading to a dependence of the dissipative stress on the size of the phase boundary which changes as the transformation progresses. Thermodynamic considerations are used to determine the total macroscopic stress from the stress associated with the phase equilibrium and the dissipative stress. Comparison of model predictions and MD results for three wire sizes in the 100-500 K temperature range show that the model captures the pseudoelastic behavior well and is also able to account for size and temperature effects on the behavior.

The stress-induced phase transformations have important implications for the electronic, piezoelectric, mechanical and thermal responses. In semiconducting materials such as ZnO where the thermal response of semiconductors is dominated by lattice vibrations, any variation in structure, such as due to the phase transformations observed here, can significantly alter their heat transfer characteristics. This is especially important in nanowires, where the conductivity is calculated to be one order of magnitude lower than bulk values. The low values observed are primarily due to the boundary scattering of phonons and also due to the changes in phonon spectrum in the nanostructures. Modeling

of the thermal response of the nanowires using the framework of phonon radiative transport indicates that boundary scattering is responsible for ~80-47% decrease in conductivity from the bulk value. Three- and four- phonon processes also lead to decreases in conductivity at higher temperatures. However, these contributions are much lower than the effect of surfaces.

In addition to the variation of conductivity with nanowire size, applied loading also affects the thermal response. Specifically, in the three regimes of the pseudoelastic response of $[01\bar{1}0]$ wires: (1) elastic stretching of WZ, (2) transformation of WZ to HX and (3) elastic stretching of HX, the thermal conductivity shows large variations with applied strain. Elastic deformation of WZ results in decrease in the conductivity associated with the nonlinearity of the stress-strain response. Upon initiation of transformation, the conductivity drops further due to the resistance of the interfaces formed between WZ and HX. However, as the transformation progresses, increase in the conductivity is observed due to the higher conductivity of HX. The nanowire has ~20% higher conductivity in HX phase than its corresponding value in WZ. The enhancement is primarily due to an increase in atomic packing density, lower anharmonic coupling of phonons and higher surface specularities of the HX-structured wires.

The current research focused on the development of a computational framework including MD simulations of and continuum modeling of the thermomechanical behavior of ZnO nanowires. Novel phase transformations have been discovered and the crystallographic aspects of the newly discovered phases and mechanistic descriptions of their corresponding transformation paths have been characterized. Thermal response under stress-free and strained conditions has been quantified and tunability in the thermal response has been demonstrated. Since these nanowires have been recently fabricated and also these transformations have been newly discovered, future research efforts can be directed at the following aspects

(1) Although, this research focused on the phase transformations to HX and BCT-4 structures for ZnO which is a group II-VI material, it is possible that these polymorphs can exist for other groups IV, III-V and II-VI materials such as GaN, InN and CdSe, all of which are WZ-structured under ambient conditions. A combination of MD simulations and first-principles calculations can be carried out to establish the stability of HX and BCT-4 in these materials. Such characterizations will translate to a complete understanding of the effect of load triaxiality on polymorphic transitions for all materials considered. Based on stability of each phase, factors such as bonding states, bond ionicities and structural symmetries fundamental to the phase transformations can be identified.

(2) The framework of analysis in this work is primarily computational and, in future, can be complemented with experimental characterization. With the current advances in experimental techniques including nanoindentation with AFM probes, the possibility of observing the WZ-to-HX transformation is quite high. Recent investigations on indentations along the [0001] orientation of WZ-ZnO have shown an anomalous decrease in the uniaxial modulus (Lucas et al. 2007a; Lucas et al. 2007b). Such effects could be related to either surface reconstructions to a layered structure (LY) or could involve transformation to the HX structure. Similarly, recent experimental testing on the uniaxial tensile response of [0001]-oriented nanorods has shown fracture strains up to 15%. However crystallographic characterization through techniques such as X-ray diffraction was not carried out. Transformation to BCT-4 structure such as that reported in this work could possibly explain the high values of fracture strains observed. Development of facilities which incorporate crystallographic analysis during mechanical testing would facilitate experimental characterization of phase transformations at the nanoscale. Furthermore, analysis of thermal response with applied strain has been extensively studied at the macroscale. However, currently,

the experimental characterization of thermal response of nanostructures is limited to analyzing stress-free nanowires and nanotubes. The evolution of thermal response under stress and also during phase transformations has not been experimentally studied so far. Limitations imposed by the nanoscale nature of the structures render such analyses extremely difficult and therefore novel testing setups need to be developed.

(3) The constitutive behaviors of WZ and HX phases employed in the continuum model developed here are determined from MD simulations. While this is required since the elastic constants vary with size of the wires, improvements to the model can be made by developing analytical solutions to describe such constitutive behaviors. One approach involves describing the nanowire as a heterogeneous structure consisting of core and surface structures and deriving analytical expressions for their effective moduli (Dingreville et al. 2005b). Such an approach incorporates surface energy and surface stress in the definition of the elastic constants and has been successfully used to model size effects in FCC metal nanowires. Incorporation of this approach in the model for pseudoelastic response necessitates the characterization of surface energies and surface stresses for surface orientations involved. MD simulations or first-principles calculations can be employed for this purpose.

(4) Modeling of thermal response in this research considers the equation for phonon radiative transport. In this model, the variation in thermal conductivity is primarily attributed to boundary scattering of phonons. Recently, it has been proposed that significant changes can occur in the phonon density spectrum in the nanowires due to their nanoscale sizes (Balandin and Wang 1998; Balandin et al. 2004). Various models have also been developed to account for this effect. Future research directions can be directed at characterizing the changes in phonon density spectrum for ZnO nanowires and also including these results in the

modeling of thermal response. Furthermore, novel transitions in the thermal responses of the nanowires have been observed under loading. Specifically, after the transformation from WZ to HX, the thermal conductivity of the nanowires increases significantly. While, phenomenologically, this is attributed to the increase in atomic packing density, lower anharmonic coupling of phonons and higher surface specularities, explicit models need to be developed to characterize this phenomenon and understand the underlying physical mechanisms. Models developed could include the variations in phonon spectrum, phonon group velocities, surface profiles with applied strain.

REFERENCES

Abeyratne, R. and K. Bhattacharya (2001). Strain-energy functions with multiple local minima: modeling phase transformations using finite thermoelasticity, Cambridge University Press.

Abeyratne, R. and S.-J. Kim (1994). "A one-dimensional continuum model for shape memory alloys." International Journal of Solids and Structures **31**: 222-2249.

Abeyratne, R. and J. K. Knowles (1993). "A continuum model of a thermoelastic solid capable of understanding phase transitions." Journal of Mechanics and Physics of Solids **51**: 541-571.

Aflatooni, K. and A. Nathan (1995). "Heat transport properties of semiconductors under nonuniform stress." Applied Physics Letters **66**(9): 1110-1111.

Andersson, P. (1985). "Thermal conductivity under pressure and through phase transitions in solid alkali halides. I. Experimental results for KCl, KBr, KI, RbCl, RbBr and RbI." Journal of Physics C (Solid State Physics) **18**(20): 3943.

Arnold, M. S., P. Avouris, et al. (2003). "Field-effect transistors based on single semiconducting oxide nanobelts." Journal of Physical Chemistry **107**: 659-663.

Asnin, V. M., F. H. Pollak, et al. (1999). "High spatial resolution thermal conductivity of lateral epitaxial overgrown GaN/sapphire.0001. using a scanning thermal microscope." Applied Physics Letters **75**(9): 1240-1242.

Bae, S. Y., H. W. Seo, et al. (2002). "Single-crystalline gallium nitride nanobelts." Applied Physics Letters **81**(1): 126-128.

Bai, X. D., P. X. Gao, et al. (2003). "Dual-mode resonance of individual ZnO nanobelts." Applied Physics Letters **82**(26): 4806-4808.

Balandin, A., D. L. Nika, et al. (2004). "Phonon spectrum and group velocities in wurtzite hetero-structures." Physica Status Solidi C: Conferences **1**(11): 2658.

Balandin, A. and K. L. Wang (1998). "Significant decrease of the lattice thermal conductivity due to phonon confinement in a free-standing semiconductor quantum well." Physical Review B **58**(3): 1544.

Bates, C. H., W. B. White, et al. (1962). "New high-pressure polymorph of zinc oxide." Science **137**(3534): 993.

Berman, R., E. L. Foster, et al. (1955). "Thermal conductivity in artificial sapphire crystals at low temperatures. I. Nearly perfect crystals." Proceedings of the Royal Society of London A **231**(1184): 130-144.

Binks, D. J. (1994). Computational modelling of zinc oxide and related oxide ceramics. Dept. of Chemistry. Harwell, University of Surrey**:** 229.

Binks, D. J. and R. W. Grimes (1993). "Incorporation of monovalent ions in ZnO and their influence on varistor degradation." Journal of the American Ceramic Society **76**(9): 2370-2372.

Branicio, P. S. and J.-P. Rino (2000). "Large deformation and amorphization of Ni nanowires under uniaxial strain: A molecular dynamics study." Physical Review B **62**(24): 16950-16955.

Cahill, D. G., W. K. Ford, et al. (2003). "Nanoscale thermal transport." Journal of Applied Physics **93**(2): 793-818.

Capaz, R. B., H. Lim, et al. (1995). "Ab initio studies of GaN epitaxial growth on SiC." Physical Review B (Condensed Matter) **51**(24): 17755-17757.

Chen, C. Q., Y. Shi, et al. (2006a). "Size dependence of Young's modulus in ZnO nanowires." Physical Review Letters **96**(7): 075505.

Chen, C. Q., Y. Shi, et al. (2006b). "Size Dependence of Young's Modulus in ZnO Nanowires." Physical Review Letters **96**: 075505-1-4.

Claeyssens, F., C. L. Freeman, et al. (2005). "Growth of ZnO thin films—experiment and theory." Journal of Materials Chemistry **15**: 139-148.

Comini, E., G. Faglia, et al. (2002a). "Stable and highle sensitive gas sensors based on semiconducting oxide nanobelts." Applied Physics Letters **81**(10): 1869-1871.

Comini, E., G. Faglia, et al. (2002b). "Stable and highly sensitive gas sensors based on semiconducting oxide nanobelts." Applied Physics Letters **81**(10): 1869-1871.

Dai, Z. R., Z. W. Pan, et al. (2002). "Gallium oxide nanoribbons and nanosheets." Journal of physical chemistry B **106**: 902-904.

Desai, A. V. and M. A. Haque (2007). "Mechanical properties of ZnO nanowires." Sensors and Actuators, A: Physical **134**(1): 169.

Desgreniers, S. (1998). "High-density phases of ZnO: Structural and compressive parameters." Physical Review B **58**(21): 14102-14105.

Diao, J., K. Gall, et al. (2003). "Surface-stress-induced phase transformation in metal nanowires." Nature Materials **2**: 656-660.

Diao, J., K. Gall, et al. (2004a). "Atomistic simulations of the structure and elastic properties of gold nanowires." Journal of mechanics and physics of solids **52**: 1935-1962.

Diao, J., K. Gall, et al. (2004b). "Surface stress driven reorientation of gold nanowires." Physical Review B **70**: 075413.

Diao, J., K. Gall, et al. (2004c). "Yield strength asymmetry in metal nanowires." Nano Letters **4**(10): 1863-1867.

Diao, J., Gall, K.,Dunn, M. L. (2004). "Atomistic simulation of the structure and elastic properties of gold nanowires." Journal of the Mechanics and Physics of Solids **52**(9): 1935-1962.

Dingreville, R., J. Qu, et al. (2005a). "Surface free energy and its effect on the elastic behavior of nano-size particles, wires and films." Journal of the Mechanics and Physics of Solids **53**: 1827-1854.

Dingreville, R., J. Qu, et al. (2005b). "Surface free energy and its effect on the elastic behavior of nano-sized particles, wires and films." Journal of Mechanics and Physics of Solids **53**: 1827-1854.

Fjeldly, T., T. Ishiguro, et al. (1973). "Heat-Pulse Propagation in p-Type Si and Ge under Uniaxial Stress." Physical Review B **7**(4): 1392.

Freeman, C. L., F. Claeyssens, et al. (2006). "Graphitic Nanofilms as Precursors to Wurtzite Films: Theory." Physical Review Letters **96**: 066102-1-4.

Gadzhiev, G. G. (2003). "The thermal and elastic properties of zinc oxide-based ceramics at high temperatures." High Temperature **41**(6): 778-782.

Gall, K. (2007). Personal Communication.

Gall, K., J. Diao, et al. (2004). "The strength of gold nanowires." Nano Letters **4**(12): 2431-2436.

Gall, K., M. L. Dunn, et al. (2002a). "Shape memory polymer nanocomposites." Acta Materialia **50**(20): 5115.

Gall, K., M. L. Dunn, et al. (2002b). "Micro and macro deformation of single crystal NiTi." Journal of Engineering Materials and Technology, Transactions of the ASME **124**(2): 238.

Gall, K., T. J. Lim, et al. (2000). "Role of intergranular constraint on the stress-induced martensitic transformation in textured polycrystalline NiTi." International Journal of Plasticity **16**(10): 1189.

Gao, P. X., C. S. Lao, et al. (2005). "Three-dimensional interconnected nanowire networks of ZnO." Chemical Physics Letters **408**: 174-178.

Gao, P. X. and Z. L. Wang (2005). "Nanoarchitectures of semiconducting and piezoelectric zinc oxide." Journal of Applied Physics **97**: 044304.

Goniakowski, J., C. Noguera, et al. (2004). "Using Polarity for Engineering Oxide Nanostructures: Structural Phase Diagram in Free and Supported MgO(111) Ultrathin Films." Physical Review Letters **93**(21): 215702-1-4.

Grimes, R. W., D. J. Binks, et al. (1995). "The extent of zinc oxide solution in zinc chromate spinel." Philosophical magazine A **72**(3): 651-668.

Haile, J. M. (1997). Molecular Dynamics Simulation. New York, Wiley-Interscience.

Hirsinger, L., N. Creton, et al. (2004). Stress-induced phase transformations in Ni-Mn-Ga alloys: experiments and modelling, Cirencester, UK, Elsevier.

Hoffmann, S., F. Ostlund, et al. (2007). "Fracture strength and Young's modulus of ZnO nanowires." Nanotechnology **18**(20): 205503.

Hughes, W. L. and Z. L. Wang (2003). "Nanobelts as nanocantilevers." Applied Physics Letters **82**(17): 2886-2888.

Huo, Y. and I. Muller (2003). "Interfacial and inhomogeneity penalties in phase transitions." Continuum Mechanics and Thermodynamics **15**(4): 395.

Jaffe, J. E. and A. C. Hess (1993). "Hartree-Fock study of phase changes in ZnO at high pressure." Physical Review B **48**(11): 7903-7909.

Jaffe, J. E., J. A. Snyder, et al. (2000). "LDA and CGA calculations for high-pressure phase transition in ZnO and MgO." Physical Review B **62**(3): 1660-1665.

Jeanloz, R. and M. Roufosse (1982). "Anharmonic properties: ionic model of the effects of compression and coordination change." Journal of Geophysical Research **87**(B13): 10763.

Jelínek, P., R. Pérez, et al. (2003). "First-principles simulations of the stretching and final breaking of Al nanowires: Mechanical properties and electrical conductance." Physical Review B: Condensed Matter and Materials Physics **68**(8): 085403.

Joshi, Y. P., M. D. Tiwari, et al. (1970). "Role of Four-Phonon Processes in the Lattice Thermal Conductivity of Silicon from 300 to 1300°K." Physical Review B **1**: 642-646.

Ju, S.-P., J.-S. Lin, et al. (2004). "A molecular dynamics study of the tensile behavior of ultrathin gold nanowires." Nanotechnology **15**: 1221-1225.

Jund, P. and R. Jullien (1999). "Molecular-dynamics calculation of the thermal conductivity of vitreous silica." Physical review B **59**(21): 13707-13711.

Karzel, H., W. Potzel, et al. (1996). "Lattice dynamics and hyperfine interactions in ZnO and ZnSe at high external pressures." Physical Review B **53**(17): 11425-11438.

Kim, P., L. Shi, et al. (2001). "Thermal transport measurements of individual multiwalled nanotubes." Physical Review Letters **87**(21): 215502-1-4.

Klemens, P. G. (1954). "The scattering of low-frequency lattice waves by static imperfections." Proceedings of the Phys. Soc. LXVIII **12-A**: 1113.

Klemens, P. G. (1994). "Phonon scattering and thermal resistance due to grain boundaries." International Journal of Thermophysics **15**(6): 1345.

Komanduri, R., N. Chandrasekaran, et al. (2001). "Molecular dynamics (MD) simulation of uniaxial tension of some single-crystal cubic metals at nanolevel." international journal of mechanical sciences **43**: 2237-2260.

Komanduri, R., N. Chandrasekaran, et al. (2003). "Molecular dynamics simulation of uniaxial tension at nanoscale of semiconductor materials for micro-lectro-mechanical systems (MEMS) applications." Materials science and engineering A **340**: 58-67.

Kong, X. Y. and Z. L. Wang (2003). "Spontaneous polarization-induced nanohelixes, nanosprings, and nanorings of piezoelectric nanobelts." Nano Letters **3**(12): 1625-1631.

Kresse, G. and J. Furthmüller (1996). "Efficiency of *ab-initio* total energy calculations for metals and semiconductors using a plane-wave basis set." Computational Materials Science **6**: 15-50.

Kubo, R., M. Toda, et al. (1985). Statistical Physics II. Berlin, Springer.

Kulkarni, A. J., K. Sarasamak, et al. (2007a). "Characterization of novel pseudoelastic behavior of zinc oxide nanowires." Philosophical Magazine **87**(14-15): 2117-2134.

Kulkarni, A. J., K. Sarasamak, et al. (2007b). "Effect of load triaxiality on polymorphic transitions in zinc oxide." Mechanics Research Communications **in print**.

Kulkarni, A. J. and M. Zhou (2006a). "Size-dependent thermal conductivity of zinc oxide nanobelts." Applied Physics Letters **88**: 141921-1-3.

Kulkarni, A. J. and M. Zhou (2006b). "Size-effects-dominated thermal and mechanical responses of zinc oxide nanobelts." Acta Mechanica Sinica **22**: 217-224.

Kulkarni, A. J. and M. Zhou (2007). "Tunable thermal response of ZnO nanowires." Nanotechnology **18**: 435706-1-6.

Kulkarni, A. J., M. Zhou, et al. (2005). "Orientation and size dependence of the elastic properties of ZnO nanobelts." Nanotechnology **16**(12): 2749-2756.

Kulkarni, A. J., M. Zhou, et al. (2006). "Novel phase transformation in ZnO nanowires under tensile loading." Physical Review Letters **97**: 105502-1-4.

Landman, U., W. D. Luedtke, et al. (1996). "Reversible manipulations of room temperature mechanical and quantum transport properties in nanowire junctions." Physical Review Letters **77**(7): 1362.

Leeuwen, J. M. J. V., J. Groeneveld, et al. (1959). "New method for the calculation of the pair correlation function. I." Physica (Amsterdam) **25**: 792-808.

Li, D., Y. Wu, et al. (2003). "Thermal conductivity of individual silicon nanowires." Applied Physics Letters **86**(14): 2934-2936.

Liang, H., M. Upmanyu, et al. (2005a). "Size-dependent Elasticity of Nanowires: Nonlinear Effects." Physical Review B **71**: 241403(R).

Liang, W. and M. Zhou (2003). Size and strain rate effects in tensile deformation of Cu nanowires. Nanotechnology Conference and Trade Show, San Fransisco, CA, Computational Publications.

Liang, W. and M. Zhou (2005). "Pseudoelasticity of single crystalline Cu nanowires through reversible lattice reorientations." Journal of Engineering Materials and Technology **127**: 123-133.

Liang, W. and M. Zhou (2006). "Atomistic simulations reveal shape memory of fcc metal nanowires." Physical Review B (Condensed Matter) **73**: 115409-1-11.

Liang, W., M. Zhou, et al. (2005b). "Shape Memory Effect in Cu Nanowires." Nano Letters **5**(10): 2039-2043.

Limpijumnong, S. and S. Jungthawan (2004). "First-principles study of the wurtzite-to-rocksalt homogeneous transformation in ZnO: A case of a low-transformation barrier." Physical Review B **70**: 054104-1-4.

Limpijumnong, S. and W. R. L. Lambrecht (2001a). "Homogeneous strain deformation path for the wurtzite to rocksalt high-pressure transition in GaN." Physical Review Letters **86**(1): 91-94.

Limpijumnong, S. and W. R. L. Lambrecht (2001b). "Theoretical study of the relative stability of wurtzite and rocksalt phases in MgO and GaN." Physical Review B (Condensed Matter) **63**: 104103-1-11.

Liu, Y., K. Gall, et al. (2004). Thermomechanics of the shape memory effect in polymers, Boston, MA, United States, Materials Research Society, Warrendale, PA 15086, United States.

Lu, X., J. H. Chu, et al. (2003). "Modification of the lattice thermal conductivity in semiconductor rectangular nanowires." Journal of Applied Physics **93**(2): 1219-1229.

Lu, X., W. Z. Shen, et al. (2002). "Size effect on the thermal conductivity of nanowires." Journal of Applied Physics **91**(3): 1542-1552.

Lucas, M., W. Mai, et al. (2007a). "Aspect ratio dependence of the elastic properties of ZnO nanobelts." Nano Letters **7**(5): 1314-1317.

Lucas, M., W. J. Mai, et al. (2007b). "Size dependence of the mechanical properties of ZnO nanobelts." Philosophical Magazine **87**(14-15): 2135.

Luo, C.-Y., H. Marchand, et al. (1999). "Thermal conductivity of lateral epitaxial overgrown GaN films." Applied Physics Letters **75**(26).

Majumdar, A. (1993). "Microscal heat conduction in dielectric thin films." Journal of Heat Transfer **115**: 7-16.

Mao, S. X., M. Zhao, et al. (2003). "Nanoscale mechanical behavior of individual semiconducting nanobelts." Applied Physics Letters **83**(5): 993-995.

Mehrez, H., S. Ciraci, et al. (1997). "An atomistic study on the stretching of nanowires." Journal of Physics: Condensed matter **9**: 10843-10854.

Melchionna, S., G. Ciccotti, et al. (1993). "Hoover NPT dynamics for systems varying in shape and size." Molecular Physics **78**(3): 533-544.

Miller, R. E. and V. B. Shenoy (2000). "Size-dependent elastic properties of nanosized structural elements." Nanotechnology **11**(3): 139-147.

Mujica, A., A. Rubio, et al. (2003). "High-pressure phases of group-IV, III-V, and II-VI compounds." Reviews of Modern Physics **75**(3): 863.

Muller, C. and O. T. Bruhns (2006). "A thermodynamic finite-strain model for pseudoelastic shape memory alloys." International Journal of Plasticity **22**(9): 1658.

Muller, I. (1989). "On the size of the hysteresis in pseudoelasticity." Continuum Mechanics and Thermodynamics **1**(2): 125.

Muller, I. and H. Xu (1991). "On the pseudo-elastic hysteresis." Acta Metallurgica et Materialia **39**(3): 263.

Musolff, A. and H. Sahota (2004). "Phase transitions in the shape memory alloy CuAlNi." Continuum Mechanics and Thermodynamics **16**(6): 539.

Ni, H. and X. Li (2006). "Young's modulus of ZnO nanobelts measured using atomic force microscopy and nanoindentation techniques." Nanotechnology **17**(14): 3591.

Olson, G. B. and M. Cohen (1982). "Classical and nonclassical mechanisms of martensitic transformation." Proc. ICOMAT-82 Journal de Physique **43**: C4 75-88.

Opitz, J., P. Zahn, et al. (2002). "Ab initio calculated electronic structure of metallic nanowires and nanotubes." Physical Review B: Condensed Matter and Materials Physics **66**(24): 245417/1-9.

Otsuka, K. and C. M. Wayman (1998). Shape memory materials. New York, Cambridge University Press.

Ozgur, U., Y. I. Alivov, et al. (2005). "A comprehensive review of ZnO materials and devices." Journal of Applied Physics **98**: 041301.

Pan, Z. W., Z. R. Dai, et al. (2001). "Nanobelts of semiconducting oxides." Science **291**(9): 1947-1949.

Park, H. S., K. Gall, et al. (2005). "Shape Memory and Pseudoelasticity in Metal Nanowires." Physical Review Letters **95**: 255504-1-4.

Picu, R. C., T. Borca-Tasiuc, et al. (2003). "Strain and size effects on heat transport in nanostructures." Journal of Applied Physics **93**(6): 3535-3539.

Polvani, D. A., J. F. Meng, et al. (2001). "Large improvement in thermoelectric properties in pressure-tuned p-type Sb1.5Bi0.5Te3." Chemistry Of Materials **13**(6): 2068-2071.

Ramdane, A., B. Salce, et al. (1983). "Stress dependence of the thermal conductivity of Cr-doped GaAs." Physical Review B **27**(4): 2554.

Raniecki, B. and C. Lexcellent (1994). "R_L-models of pseudoelasticity and their specification for some shape memory solids." European Journal of Mechanics, A/Solids **13**(1): 21.

Raniecki, B. and C. Lexcellent (1998). "Thermodynamics of isotropic pseudoelasticity in shape memory alloys." European Journal of Mechanics, A/Solids **17**(2): 185.

Roufosse, M. and P. G. Klemens (1973). "Thermal conductivity of complex dielectric crystals." Physical Review B (Solid State) **7**(12): 5379.

Roufosse, M. C. and R. Jeanloz (1983). "Thermal conductivity of minerals at high pressure: the effect of phase transitions." Journal of Geophysical Research **88**(B9): 7399.

Sander, S. (2003). "Surface stress: implications and measurements." Current opinion in Solid State and Materials Science **7**: 51-57.

Schelling, P. K., S. R. Phillpot, et al. (2002). "Comparison of atomic-level simulation methods for computing thermal conductivity." Physical review B **65**: 144306-1 144306-12.

Serrano, J., A. H. Romero, et al. (2004). "Pressure dependence of the lattice dynamics of of ZnO: An *ab initio* approach." Physical Review B **69**: 094306-1-14.

Shi, L., Q. Hao, et al. (2004). "Thermal conductivities of individual tin dioxide nanobelts." Applied Physics Letters **84**(14): 2638-2640.

Shi, L., D. Li, et al. (2003). "Measuring thermal and thermoelectric properties of one-dimensional nanstructures using a microfabricated device." Journal of heat transfer **125**: 1-8.

Slack, G. A. and R. G. Ross (1985). "Thermal conductivity under pressure and through phase transitions in solid alkali halides. II. Theory." Journal of Physics C (Solid State Physics) **18**(20): 3957.

Smith, W. and T. R. Forester (1996). DL_POLY is a molecular simulation routine written by W. Smith and T. R. Forester, copyright of CCLRC for the Central Laboratory of Research Councils, Daresbury Laboratory at Daresbury, Nr. Warrington. Daresbury.

Song, J., X. Wang, et al. (2005). "Elastic property of vertically aligned nanowires." Nano Letters **5**(10): 1954.

Sood, K. C. and M. K. Roy (1992). "Phonon conductivity of doped germanium under uniaxial stress in the [110] direction." Physical Review B **46**(12): 7486.

Spearot, D., K. Jacob, et al. (2005). "Nucleation of dislocations from [001] bicrystal interfaces in aluminum." Acta Materialia **53**(13): 3579-3589.

Streitz, F. H., R. C. Cammarata, et al. (1994). "Surface-stress effects on elastic properties. I. Thin metal films." Physical Review B **49**(15): 10699-10706.

Sun, C. T. and H. Zhang (2003). "Size-dependent elastic moduli of platelike nanomaterials." Journal of Applied Physics **93**(2): 1212-1218.

Vanderbilt, D. (1990). "Soft self-consistent pseudopotentials in a generalized eigenvalue formalism." Physical Review B (Condensed Matter) **41**(11): 7892.

Volz, S. G. and G. Chen (1999a). "Lattice dynamics simulation of silicon thermal conductivity." Physica B **263-264**: 709-712.

Volz, S. G. and G. Chen (1999b). "Molecular dynamics simulation of thermal conductivity of silicon nanowires." Applied Physics Letters **75**(14): 2056-2058.

Walkauskas, S. G., D. A. Broido, et al. (1999). "Lattice thermal conductivity of wires." Journal of Applied Physics **85**(5): 2579-2582.

Wang, J., A. J. Kulkarni, et al. (2007). "Molecular dynamics and density functional studies of a body-centered-tetragonal polymorph of ZnO." Physical Review B (Condensed Matter and Materials Physics) **in print**.

Wang, Z. L. (2004a). "Functional Oxides Nanobelts – Materials, properties and potential applications in Nanosystems and Biotechnology." Annual Review of Physical Chemistry **55**: 159-196.

Wang, Z. L. (2004b). "Zinc oxide nanostructures: growth, properties and applications." Journal of Physics: Condensed matter **16**: R829-R858.

Wang, Z. L. (2005). "Self-assembled nanoarchitectures of polar nanobelts/nanowires." Journal of Materials Chemistry **15**: 1021-1024.

Wang, Z. L., X. Y. Kong, et al. (2004). "Semiconductiong and piezoelectric oxide nanostructures induced by polar surfaces." Advanced functional materials **14**(10): 943-956.

Wang, Z. L. and J. Song (2006). "Piezoelectric Nanogenerators Based on Zinc Oxide Nanowire Arrays." Science **312**: 242-246.

Wei, A., X. W. Sun, et al. (2006). "Growth mechanism of tubular ZnO formed in aqueous solution." Nanotechnology **17**(6): 1740.

Wentzcovitch, R. M., S. Fahy, et al. (1988). "*Ab initio* study of graphite --> diamond-like transitions in BN." Physical Review B (Condensed Matter) **38**(9): 6191-6195.

Wolf, M. W. and J. J. Martin (1973). "Low temperature thermal conductivity of zinc oxide." Physica Status Solidi **17**: 215-220.

Yakobson, B. I., C. J. Brabec, et al. (1996). "Nanomechanics of carbon tubes: instabilities beyond linear response." Physical Review Letters **76**(14): 2511.

Yiping, L., K. Gall, et al. (2006). "Thermomechanics of shape memory polymers: Uniaxial experiments and constitutive modeling." International Journal of Plasticity **22**(2): 279.

Zhang, P., Y. Huang, et al. (2002). "The elastic modulus of single-wall carbon nanotubes: a continuum analysis incorporating interatomic potentials." International Journal of Solids and Structures **39**(13-14): 3893-3906.

Zhao, M. H., Z. L. Wang, et al. (2004). "Piezoelectric characterization of individual zinc oxide nanobelts probed by piezoresponse force microscope." Nano Letters **4**(4): 587-590.

Zheng, J. C., H. Q. Wang, et al. (2002). "Structural and electronic properties of Al nanowires: an ab initio pseudopotential study." International Journal of Nanoscience **1**(2): 159-169.

Zhou, M. (2003). "A new look at the atomic level virial stress: on continuum-molecular system equivalence." Proceedings of the Royal Society of London **459**: 2347-2392.

Ziman, J. M. (1960). Electrons and phonons. London, Oxford University Press.

Zou, J. and A. Balandin (2001). "Phonon heat conduction in a semiconductor nanowire." Journal of Applied Physics **89**(5): 2932-2938.